Université de Valenciennes et du Hainaut-Cambrésis

Thèse de doctorat

Pour obtenir le grade de Docteur de l'Université de

VALENCIENNES ET DU HAINAUT-CAMBRESIS

et le cas échéant ETABLISSEMENT DE COTUTELLE

Discipline, spécialité selon la liste des spécialités pour lesquelles l'Ecole Doctorale est accréditée :

Mécanique - Energétique

Présenté et soutenu par Pin CHEN

Le 14/02/2018, à UVHC

Ecole doctorale :

Sciences Pour l'Ingénieur (SPI)

Equipe de recherche, Laboratoire :

Laboratoire d'Automatique, de Mécanique et d'Informatique Industrielles et Humaines (LAMIH UMR CNRS 8201)

Enhancement of Drops Evaporation Using Nanoparticles and Alcohols

Amélioration de l'évaporation des gouttes à l'aide de nanoparticules et d'alcools

JURY

Président du jury

- SARTRE Valérie, Maître de Conférences, INSA de Lyon.

Rapporteur

- BENNACER Rachid, Professeur, l'ENS Cachan.
- ABID Cherifa, Maître de Conférences-HDR, Polytech Marseilles.

Examinateurs

- SARTRE Valérie, Maître de Conférences, INSA de Lyon.
- CARLIER Julien, Maître de Conférences-HDR, UVHC.

Directeur de thèse

HARMAND Souad, Professeur, UVHC.

Co-directeur de thèse

BIGERELLE Maxence, Professeur, UVHC.

Abstract

In recent years, increasing requirement in high efficient heat dissipation for micro-electronics, spacecraft, nuclear reactors etc., encourage the development of next generation heat exchanger. Heat pipe is one of potential effective cooling equipments and most of mass and heat transfer take place at micro-region near triple phase (solid, liquid, vapor) contact line of working fluid, which is essential to thermal performance improvement of heat pipe. This study focuses on the evaporation process of sessile droplets of two novel working fluids (binary solution and nanofluid), which possess similar micro-region to that in heat pipe. Concentration gradient induced Marangoni flow and exceptional thermal conductivity are expected to significantly enhance evaporation rate of alcohol-water mixture and graphene nanofluid, respectively. A combination of acoustic and infrared techniques is developed to track alcohol concentration variation during evaporation of 1-butanol and ethanol aqueous droplets. According to observation of evaporation behavior at different substrate temperature, a series of empirical equations is suggested to predict evaporation rate of 1-butanol-water binary solution droplet considering thermal and solutal Marangoni effect. In addition, the effect of PEGylation, nanoparticle concentration and substrate temperature on drop evaporation of graphene nanofluid are investigated by microscopic, optical and infrared methods. Experimental results and thermodynamic analysis can contribute to the full understanding of involved mechanism concerning evaporation performance of graphene nanofluid.

Keywords: Drop evaporation, Binary solution, Nanofluid, Marangoni effect.

Résumé

Au cours des dernières années, les exigences croissantes en matière de dissipation thermique à haut rendement pour la microélectronique, les engins spatiaux, les réacteurs nucléaires, etc., encouragent le développement d'échangeurs de chaleur de nouvelle génération. Le caloduc est l'un des équipements de refroidissement efficaces et potentiels. La plupart du transfert de masse et de chaleur se fait au niveau de la micro-région près de la ligne triple de contact (solide, liquide, vapeur), qui est essentielle à l' amélioration de la performance thermique du caloduc. Cette étude se concentre sur le processus d'évaporation de gouttes sessiles de deux nouveaux fluides de travail (solution binaire et nanofluide), qui possèdent une micro-région similaire à celle du caloduc. Le flux de Marangoni induit par le gradient de concentration et la conductivité thermique exceptionnelle devraient améliorer significativement le débit evaporé du mélange alcool-eau et du nanofluide de graphène, respectivement. Une combinaison de techniques acoustiques et infrarouges est développée pour suivre la variation de la concentration d'alcool pendant l'évaporation des gouttes des mélanges 1-butanol-eau et éthanol-eau. Selon l'observation du comportement d'évaporation à différentes températures du substrat, une série d'équations empiriques est suggérée pour prédire le taux d'évaporation de la solution binaire de 1-butanol-eau en considérant l'effet Marangoni thermal et solutal. De plus, l'effet de la PEGylation, de la concentration des nanoparticules et de la température du substrat sur l'évaporation de gouttes de graphène nanofluide est étudié par des méthodes microscopiques, optiques et infrarouges. Les résultats expérimentaux et l'analyse thermodynamique peuvent contribuer à la compréhension complète du

mécanisme impliqué concernant les performances d'évaporation du nanofluide de graphène.

Mots clés: Evaporation des gouttes, Solution binaire, Nanofluide, Effet Marangoni.

Acknowledgements

I would like to express the deepest appreciation to all people who helped, encouraged and supported the accomplishment of my PhD dissertation.

First of all, a thank you to my supervisors Prof. Souad Harmand and Prof. Maxence Bigerelle, who gave me this opportunity and continuously offered insights and guidance throughout my PhD study. I would also like to express my gratitude to Prof. Rachid Bennacer and Dr. Cherifa Abid for spending valuable time to provide very helpful feedbacks and advices to improve my research. I would like to acknowledge the rest of my committee members Dr. Valérie Sartre, Dr. Julien Carlier for sharing their ideas and advising me throughout this process.

Besides, I would like to thank Dr. Malika Toubal, Prof. Bertrand Nongaillard, Mr. Jesse Schiffler, Mr. Safouene Ouenzerfi, Prof. Sabine Szunerits and Prof. Rabah Boukherroub for their valuable contributions. Also I would like to thank the support of current and previous LAMIH laboratory members, Celine Morin, Damien Meresse, Eric Delacourt, Fateh Mameri, Fethi Aloui, François Beaubert, Jean-Michel Dailliet, Marc Lippert, Maryam Parsa, Maxime Balligand, Raphaël Deltombe, Riadh Boubaker, Sabine Guilain-Houvenaghel and Sofia Korniliou.

Finally, special thanks go to my parents and my wife Lian Feng whose presence, help and encouragements were never missing. I am extremely grateful to them.

Table of Contents

Chapter 1 Introduction 1
1.1 Background 1
1.1.1 Heat transfer enhancement 1
1.1.2 Heat pipe 4
1.2 Research Objectives and Thesis Outline 8
Chapter 2 Literature Review 11
2.1 Binary Solutions 11
2.1.1 Marangoni effect 15
2.1.2 Self-rewetting fluids 18
2.2 Nanofluids 22
2.2.1 Preparation methods 23
2.2.2 Stability enhancement methods 24
2.2.3 Applications 26
2.3 Conclusions 26
Chapter 3 Alcohol Concentration Tracking of Binary Sessile Droplets during Evaporation 29
3.1 Abstract 29
3.2 Introduction 30
3.3 Experimental Setup 33
3.3.1 Optical and infrared measurements 33
3.3.2 Acoustic measurements 34
3.4 Experimental Results 38
3.4.1 Calibration of the acoustic measurement method 38

3.4.2 Evaporation of drops of pure liquids 40
3.4.3 Evaporation of drops of binary solutions 47
3.4.4 Comparison between acoustics and infrared observations 57
3.5 Conclusions 60
Chapter 4 Effect of Marangoni Flow on Evaporation Performance of Binary Sessile Droplets 63
4.1 Abstract 63
4.2 Introduction 64
4.3 Experimental Setup 69
4.4 Experimental Results and Discussion 70
4.5 Conclusions 90
Chapter 5 Effect of Multi Factors on Evaporation Performance of Graphene Nanofluid Droplets 93
5.1 Abstract 93
5.2 Introduction 94
5.3 Experiment Method 99
5.3.1 Synthesis of GO and rGO-PEG 99
5.3.2 Characterization results 100
5.3.3 Experimental setup 104
5.4 Results and Discussion 105
5.4.1 Experimental results at ambient conditions 105
5.4.2 Experimental results on heated substrates 113
5.5 Conclusions 130
Chapter 6 133
Conclusions and future work 133
Reference 137

Chapter 1 Introduction

1.1 Background

1.1.1 Heat transfer enhancement

Heat transfer is a basic physical process due to temperature difference between two objects or various parts of same object that thermal energy flows from high temperature place to low temperature place. As a fundamental discipline in thermal engineering with broad applications as heat exchanger, condenser, boiler and evaporator, heat transfer becomes an important subject that attracts researchers to hunt for the enhancement methods. In 1861, Joule [1] investigated the condensation of steam by using water and air as refrigerant and found that augmented steam velocity or spiral refrigerant flow will improve heat exchange performance, which is the first attempt to enhance heat transfer efficiency. Since that, numerous studies have been reported on heat transfer enhancement with increasing need in thermal engineering. The effective enhancement techniques are generally classified in two categories: passive and active methods. The difference is that the passive methods do not require extra power input while the active methods need external power supply. Bergles [2] identified several heat transfer enhancement methods whose efficiency strongly depends on the mode of heat transfer (single-phase, boiling, and condensation with natural or forced flow, respectively), the brief descriptions are following:

Passive methods

a. *Treated surfaces* with continuous or discontinuous fine-scale on surface finish or coating are applied principally in boiling and condensation. The roughness height of surface is inferior to that for single-phase heat transfer.
b. *Rough surfaces* with modified configurations varying from random sand-grain roughness to discrete protuberances are generally assigned to enhance heat transfer of single-phase flow. The aim of surface configuration is for turbulence promotion instead of heat transfer surface area extension.
c. *Extended surfaces* with increased effective heat transfer surface are customarily used for heat exchangers. The new development trend of extended surfaces is to combine surface area enlargement with improved heat transfer coefficient by modifying finned surfaces.
d. *Displaced enhancement devices* installed at interior surface of flow channel are employed for forced convection by indirect energy transport improvement at the heat exchange surface.
e. *Swirl-flow devices* including helical wire coils, twisted tapes, inlet vortex vanes, axial cores with screw-type windings, periodic spaced propellers etc., are engaged to induce swirl or secondary flows for single-phase or two-phase forced convection in channel.
f. *Coiled tubes* are employed in single-phase flow or most region of boiling, which induce secondary flows or Dean vortices to enhance heat transfer coefficient by coiled inner surface.

g. *Surface-tension devices* involve wicking or grooved surfaces, which drive the flow of liquid to boiling area and from condensing area by capillary force.
h. *Additives for liquid* include solid particles, gas bubbles and trace additives. The two former are used for single-phase flows while the latter for boiling systems.
i. *Additives for gas* include liquid droplets and solid particles, which are added in single-phase gas flows for forming dilute phase (gas-solid suspensions) or dense phase (fluidized beds).

Active methods

a. *Mechanical aids* include stirring, surface scraping, rotating surfaces and resonating pulse reactor, which agitate the fluid by mechanical means or by rotating the surface.
b. *Surface vibration* with either low or high frequency is primarily utilized to enhance the heat transfer efficiency of single-phase flows.
c. *Fluid vibration* as well as fluid pulsation, is the most practical vibration technique principally for heat transfer enhancement of single-phase fluids with vibration frequency ranging from 1 Hz to ultrasound.
d. *Electrostatic fields* (dc or ac sources) are used to create electric or magnetic fields, or combined field of both, which can intensify bulk fluid mixing and generate forced convection in dielectric fluids in order to improve heat transfer.
e. *Injection* is merely applied for single-phase flow by injecting gas, same or different liquid directly to the upstream of heat transfer section or to the convection flow through a porous heat transfer media.

f. *Suction* is used in nucleate or film boiling to remove vapor through a porous heated surface, or in single-phase flow to withdraw fluid through a porous heated surface.

g. *Jet impingement* is utilized in single or multiple mode (clusters or staged axially along the flow channel) to improve the heat transfer efficiency of single-phase flow or boiling by jetting heating or cooling fluid to the heat transfer surface at vertical or inclined angle.

The compound heat transfer enhancement method is that two or more of above mentioned methods are simultaneously applied to achieve a significantly improved heat transfer, which is higher than that obtained by only one enhancement method. The heat pipe is one of compound enhancement methods, which includes several passive methods (extended surfaces, surface tension devices, additives for liquid etc.).

1.1.2 Heat pipe

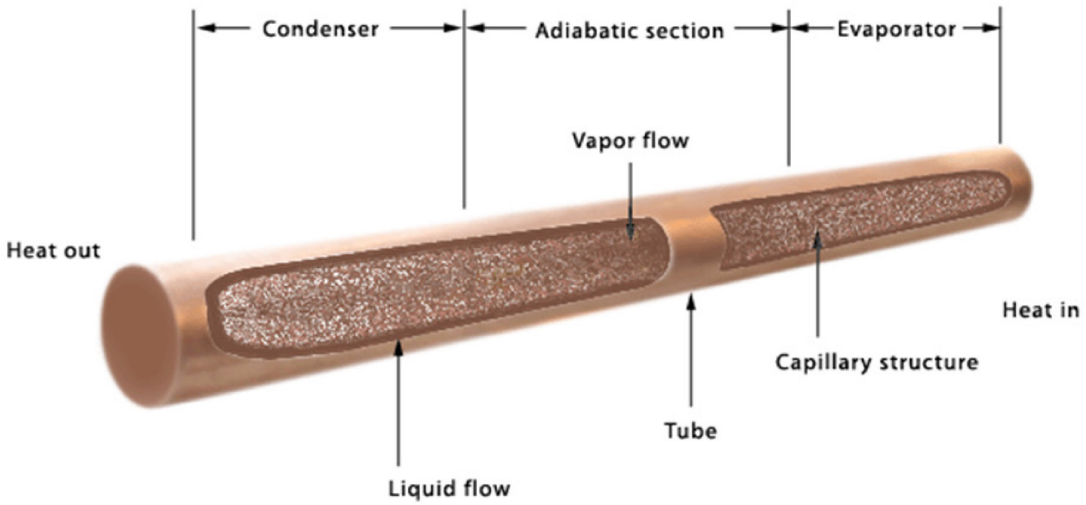

Figure 1.1 Schema of capillary-driven heat pipe. Image is from Ref. [3]

Heat pipe is a passive heat exchanger with advantages of significantly high heat transfer efficiency, flexible size, long service life, minimum maintenance and no require in external power. Fig. 1.1 represents the typical capillary-driven heat pipe with a cylindrical geometry. The heat pipe consists of a sealed pipe or tube which can be divided in three sections: evaporator section, adiabatic section and condenser section. The evaporator section is connected to the heat source while the condenser section is connected to the heat sink. The interior surface of heat pipe has wick structure. The working fluid absorbs the heat at evaporator section via thermal conduction and evaporates to become vapor phase. The generated vapor increases the vapor pressure at evaporator section which drives the vapor to arrive at condenser section through adiabatic section. The vapor concedes the latent heat of evaporation to the connected heat sink at condenser section and condenses to become liquid phase again. The wick structure drives the condensed working fluid back to the evaporator section by capillary force (thermosiphon uses gravitational force). The working fluid is in equilibrium state with its own vapor inside heat pipe and this circulation continues to conduct heat from evaporator section to condenser section until there is on sufficient vapor pressure difference or capillary force. The conventional working fluids applied in heat pipe are water, ammonia, methanol, acetone, heptane, sodium and so on. With a wide range of applications in electronic cooling, energy recovery, spacecraft thermal control, solar thermal etc., heat pipe becomes one of effective heat transfer devices.

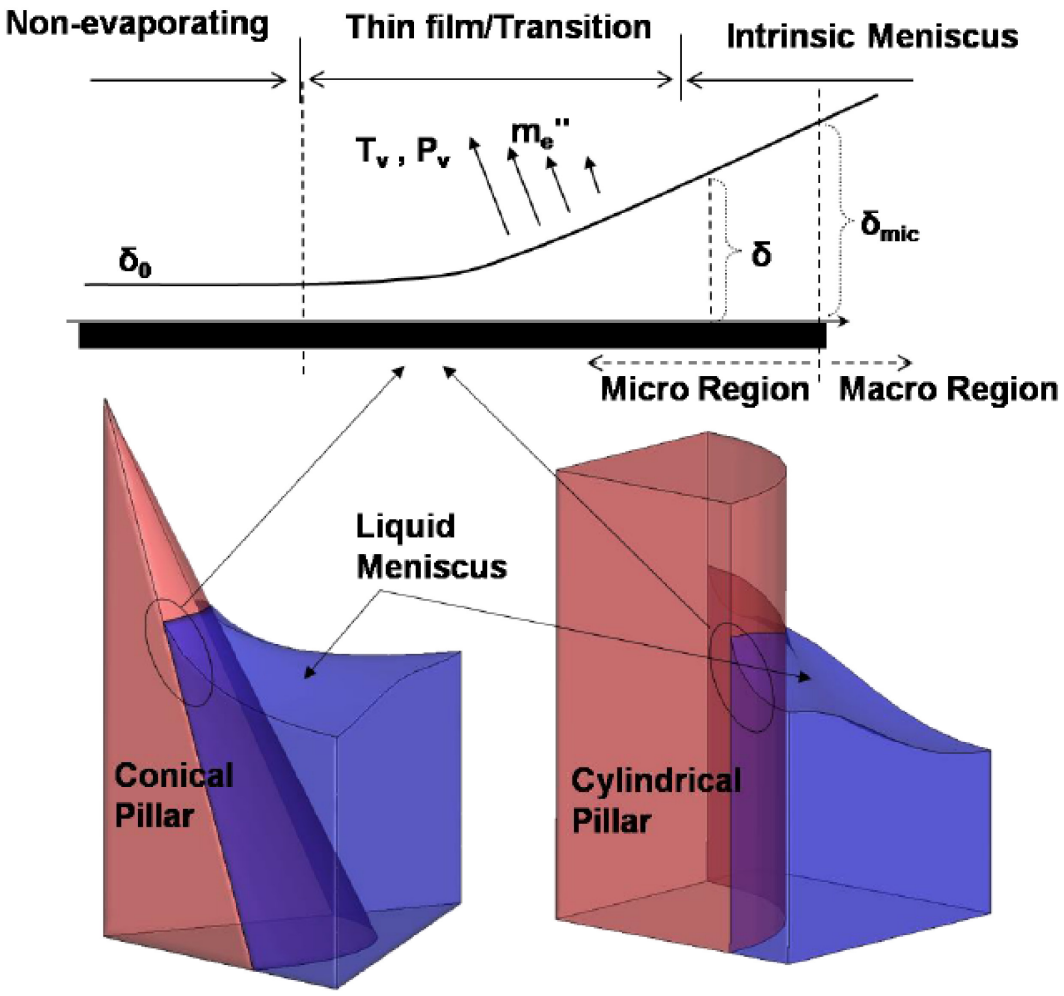

Figure 1.2 Schema of meniscus region near contact lines for thin liquid films. Image taken from Ref. [4].

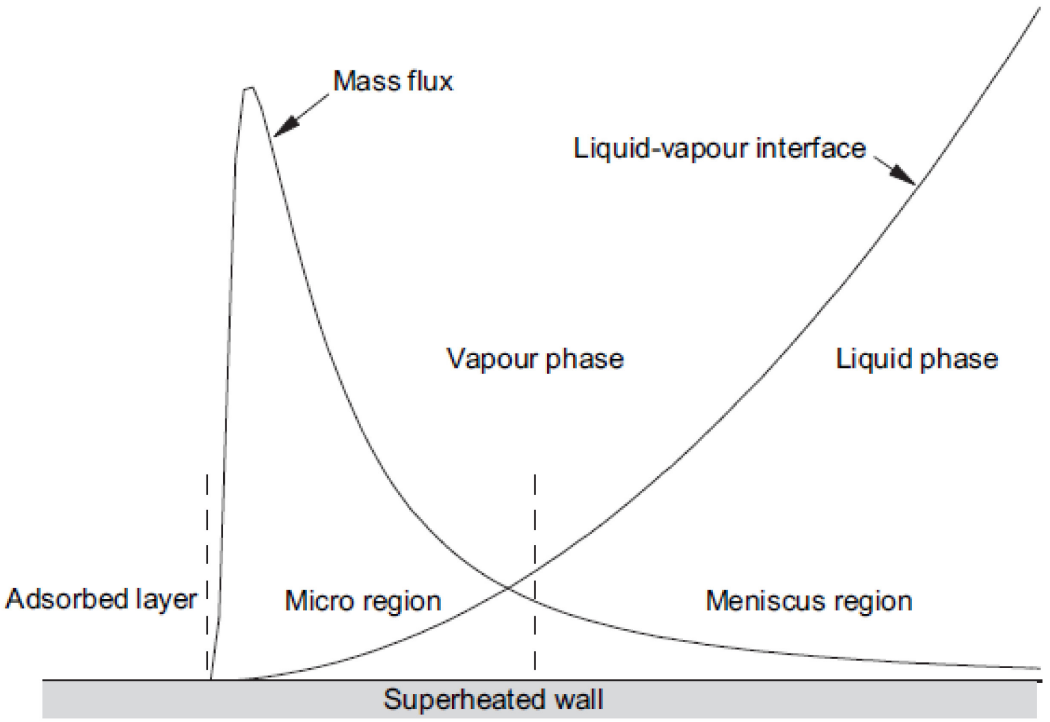

Figure 1.3 Distribution of evaporation flux along liquid meniscus. Image taken from Ref. [5].

When working fluid wets smooth or wicked surface of heat pipe, a region of the meniscus interface is created near the solid-liquid-vapor triple phase contact line (Fig. 1.2). The meniscus region is usually divided into three sub regions: non-evaporating region where working fluid is absorbed by surface without evaporation, transition region where disjoining liquid pressure takes place due to long-range molecular forces, and intrinsic meniscus region where capillary force is dominant. The enhancement of heat transfer efficiency for heat pipe is limited by the thermal resistance of evaporator section which is determined by the thermal conductivity of wick material and working fluid meniscus. For convectional application, the heat flux at evaporator section is governed by the thermal resistance of wick material. However for the application of very thin (< 200 μm) high

thermal conductivity wick structures (k > 100 W/mK), the thermal conductivity of working fluid meniscus which is primarily determined by thickness of thin film near contact line, plays a significant role in evaporation performance [4]. Many researchers report that most heat and mass transfer take place at the transition section of working fluid meniscus (Fig. 1.3) [5-8]. The study in nanoscale wick structure in order to increase the area of transition region or decrease the thickness of thin liquid film becomes more and more important in thermal performance improvement of heat pipe. Moreover, the capillary force of wick structure limit the sustainable working performance of heat pipe without the appearance of dry-out [9]. Therefore the optimization of wetting situation on wick structure is an important subject in heat transfer enhancement with increasing need in high efficiency heat exchangers.

1.2 Research Objectives and Thesis Outline

When a liquid droplet is deposited on a solid substrate, it has the same meniscus geometry near contact line as that on wick structure. Thus the study of evaporation performance and profile change in meniscus region of liquid droplet and the mechanism behind the phenomenon investigated will contribute to the optimization of wick structure as well as the heat transfer improvement of heat pipe. The main objective of this thesis is to determine the evaporation performance of droplets by using two novel solutions, binary solution and nanofluid. Binary solution can induce solutal Marangoni flow by surface tension gradient while nanofluid is supposed to possess exceptional thermal conductivity. Both will contribute to the enhancement of evaporation rate of droplets. A combination of optical, infrared and acoustic techniques is applied to investigate the

change in composition and profile of droplets and the temperature distribution on droplet surface, which can provide clues to full understanding of the complex evaporation behaviors and mechanisms near solid-liquid-vapor triple phase line. Another target of this thesis is focused on the effects of involved factors such as temperature, liquid composition and component concentration, on thermal performance of sessile droplets.

This dissertation consists of 6 chapters. The current chapter presents the fundamental theory on heat transfer enhancement and heat pipe as well as the research goal and the thesis structure. Chapter 2 summarizes the effort of the other researchers on thermal performance improvement by using binary solution and nanofluid. Chapter 3 introduces a novel combined method of optical, infrared and acoustic techniques for tracking the alcohol centration in a sessile droplet of binary solution during evaporation, which will be very helpful to illustrate the invisible component change within droplet. Chapter 4 presents the investigations on the evaporation behavior of 1-butanol-water binary droplets and the comparison of droplet evaporation rate between binary solution and pure water. A series of empirical equations for predicting the evaporation rates of pure water or 1-butanol-water binary droplets are provided. In Chapter 5, the effects of factors such as substrate temperature, PEG-functionalization, nanoparticle concentration, on evaporation performance of graphene nanofluid are investigated. The possible underlying mechanism is suggested to illustrate the evaporation rate difference between pure water and graphene nanofluid droplets. Chapter 6 concludes the accomplished experimental works and research discoveries, and proposes the perspectives in future work.

Chapter 2 Literature Review

2.1 Binary Solutions

The evaporation of a sessile droplet is a fundamental heat and mass transfer process in the nature. When a droplet is deposited on a solid surface, its profile is determined by the equilibrium of gas, liquid and solid phases (Fig. 2.1). In 1805, Young [10] described this equilibrium by the relationship between three interfacial tensions (solid/liquid, liquid/vapor and solid/vapor) in following equation:

$$\gamma_{SG} - \gamma_{SL} = \gamma_{LG} \cdot cos\theta_C \tag{1.1}$$

where γ_{SG}, γ_{SL}, γ_{LG} are surface tension of solid/vapor, solid/liquid, liquid/vapor interface respectively, θ_C is the contact angle which is the angle between liquid/solid interface and liquid/vapor interface of droplet. In addition, the contact line is the intersection of liquid phase, solid phase and vapor phase at the periphery of droplet wetted area. The wettability of solid substrate with liquid droplet depends on the physical properties of liquid and the surface characteristics of substrate, which can classify substrate in two types by the measurement of contact angle: hydrophobic when contact angle is above 90° and hydrophilic when contact angle falls in the range of 0° ~ 90°.

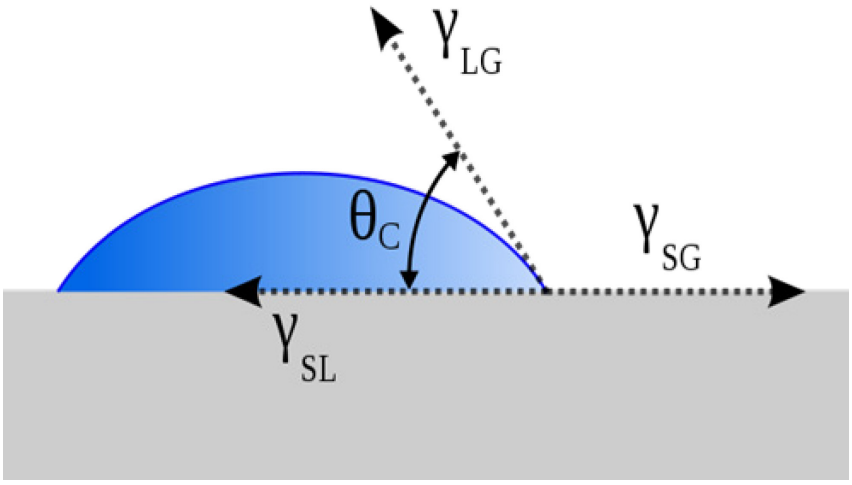

Figure 2.1 Contact angle of a liquid droplet wetted to a rigid solid surface. Image taken from Ref. [11].

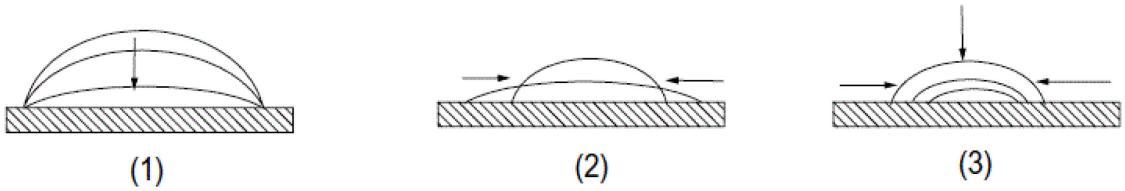

Figure 2.2 Different modes of droplet profile evolution: (1) constant contact line regime (2) mixed regime (3) constant contact angle regime. Image taken from Ref. [12].

In an atmosphere with unsaturated vapor pressure, the saturation variation between vicinity and infinity places continuously induce the evaporation of droplets deposited on solid substrate. The droplet profile varies during evaporation process due to the change in interactions of adhesive and cohesive forces. The droplet profile revolution can be identified in three different regimes (Fig. 2.2): (1) constant contact line regime (CCL), when the wetted area of droplet stays unchanged and the contact angle decreases gradually; (2) constant contact angle regime (CCA), when the contact angle remains

constant during the reduction of contact area; (3) mixed regime, when the profile evolution jump from CCL to CCA, vice versa or both contact angle and contact line decrease simultaneously. CCL regime is often observed in the evaporation of sessile droplet on hydrophilic substrate while the evaporation on hydrophobic substrate frequently behaves in CCA regime.

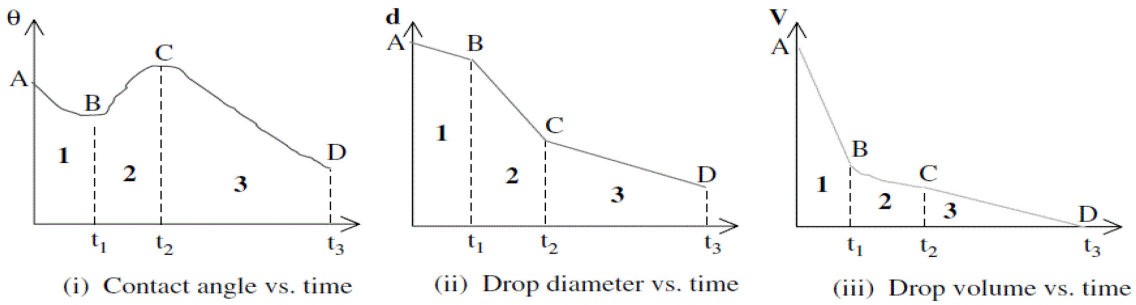

Figure 2.3 The evolution of parameters ((i) contact angle (ii) drop diameter (iii) drop volume) during evaporation of a water-ethanol mixture drop as a funciton of time. Image taken from Ref. [12].

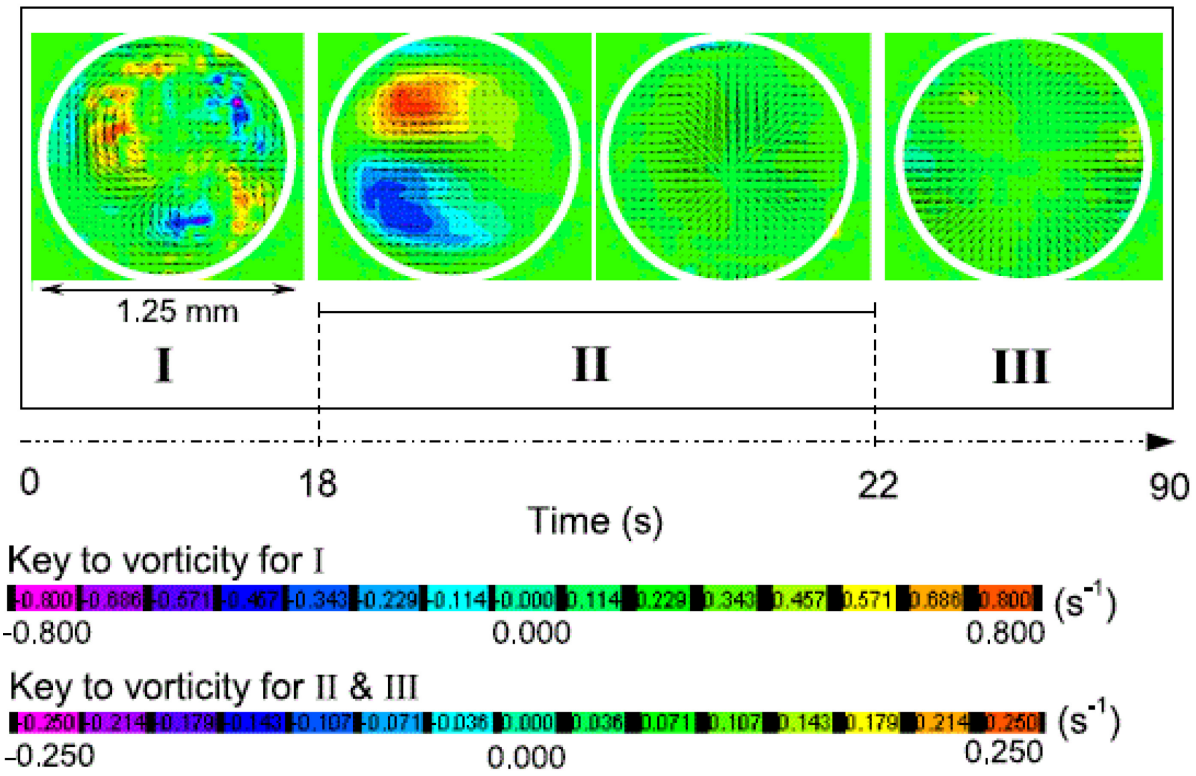

Figure 2.4 Velocity vectors and vorticity fields of three identified evaporation stages of water-ethanol mixture droplet presented by particle image velocimetry technique. Image taken from Ref. [13].

The evaporation of droplets of binary or multicomponent solution is a more complicated heat and mass transfer process. The more volatile liquid preferentially evaporates at the liquid/vapor interface, which is supplied by the diffusion of the same remained liquid from the bulk liquid of the droplet. The variation of composition in binary droplet leads to the change in physical and thermal properties such as surface tension, thermal conductivity, latent heat etc. Until the depletion of more volatile liquid, most of component remained in droplet is the less volatile one. After that, the evaporation behavior of droplet is similar to that for single component droplet. Sefiane et al. [12]

divided the evaporation process of water-ethanol mixture droplet in three different stages according to the dynamic evolution of contact angle, diameter and volume of droplet (Figure 2.3): First stage with similar evaporation behavior to that for pure volatile component droplet; Transition stage with increase of contact angle, decrease of contact diameter and a moderate evaporation rate; Last stage with similar evaporation behavior to that for less volatile component droplet. In the light of particle image velocimetry investigation by Christy et al. [13], the internal flow filed inside water-ethanol mixture droplet can be separated into three phases corresponding to evaporation behavior: Phase I with multiple vortices driven by concentration differences; Phase II with exponential decay of vortices with the migration of the remaining vortices toward the drop periphery; Phase III with evaporation driving outward flow to the contact line. Therefore a better understanding of heat and mass transfer mechanism behind mixture droplet evaporation, which is essential to many industrial processes such as circuit cooling, ink-jet printing, cloud formation, combustion etc., has attracted increasing interest in recent years. Two significant applicable effects produced by binary solutions are Marangoni effect and self-rewetting effect.

2.1.1 Marangoni effect

When concerning about the flows within a sessile single or multi component droplet on heated substrate, a surface tension difference driven effect plays an important role in evaporation kinetics. This effect is termed as Marangoni effect, named after Italian physicist Carlo Marangoni who firstly reported this surface phenomenon in 1855 [14].

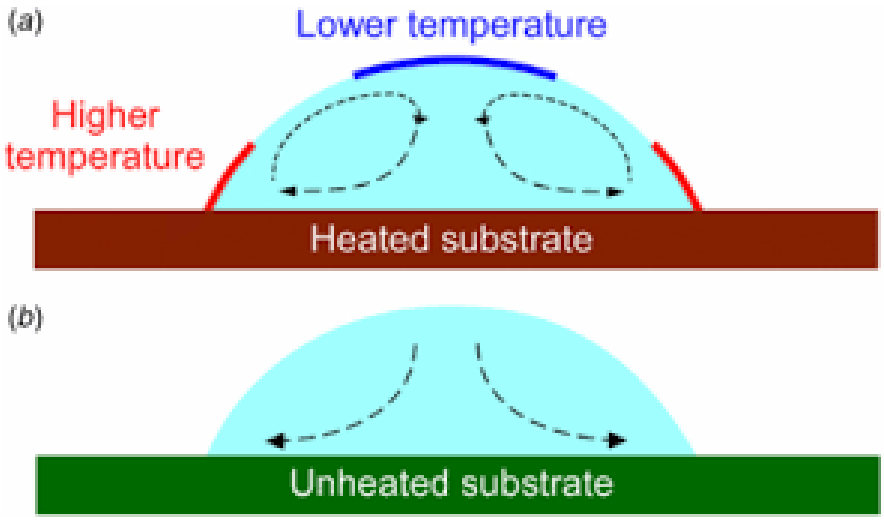

Figure 2.5 Flow structure within a single-component sessile droplet on (a) heated substrate and (b) unheated substrate. Image taken from Ref. [15].

Surface tension of common liquids has a monotonically decreasing relationship with increase of temperature. And all the liquids have an intrinsic tendency of moving from low surface tension place to high surface tension place. When a single-component droplet is deposited on an unheated substrate, as mentioned above, most of evaporation happens at vicinity of contact line. Due to continuity, a radially outward flow replenishes the part of liquid evaporated at meniscus region which is named the capillary flow (Fig. 2.5 (a)). If the substrate is heated, heat is conducted from solid/liquid interface to liquid/vapor interface. Owing to shorter heat transfer path, the temperature at vicinity of contact line is higher than that at the top of droplet. Increased temperature reduces surface tension of region near contact line and liquid is driven to the apex of droplet with higher surface tension along liquid/vapor interface (Fig. 2.5 (b)). The induced flow is called thermal Marangoni flow or thermocapillary flow. For the case of multi-component, the more volatile constituent preferably evaporates and most of mass transfer takes place at micro

region, which results in a sharp decreasing of concentration at vicinal region of contact line. As a consequence, a non-homogeneous distribution of component concentration as well as surface tension is created along the free surface of the droplet which generates the so-called solutal Marangoni flow.

Marangoni effect demonstrates potential application in DNA mapping, film coating and micro-electronic cooling according to plentiful researches on this topic. Hu and Larson [16] experimentally and theoretically investigated the effect of thermal Marangoni flow on "coffee ring" deposition of PMMA fluorescent particles by droplet drying and found that the formation of ring-like deposit necessitates not only constant contact line evaporation process but also suppressed thermal Marangoni flow. Majumder et al. [17] reported that the drying of water droplets containing nanoparticles at ethanol saturated atmosphere and ambient temperature will lead to homogenous nanoparticle deposition instead of "coffee ring" pattern. As a result of ethanol saturated pressure, water preferably evaporates and ethanol condenses from vapor phase at the vicinity region of contact line where surface tension is decreasing. The liquid flow from lower surface tension area (contact line) towards higher surface tension area (top), which is solutal Marangoni flow, recirculates nanoparticles taken by outward capillary flow near contact line and creates uniform nanoparticle deposit. In the study of Nikolov et al. [18], they suggested that the superspreading of aqueous trisiloxane ethoxylate surfactant solutions on hydrophobic surface is driven by solutal Marangoni flow and the spreading rate increases with larger surface tension gradient at free surface of liquid. The superspreaders can considerably improve the wetting problem on hydrophobic surface which is frequently encountered in numerous industrial processes. For heat transfer aspect, Savino

and Fico [19] analyzed the evaporation performance of pendant drops containing silicone oil and hydrocarbon by experimental and numerical methods, and the results revealed that the Marangoni flow induced by non-uniform evaporation can improve homogeneity of temperature distribution on drop surface as well as overall evaporation rate. Buffone and Sefiane [20] observed intense Marangoni convection inside the liquid meniscus formed in capillary tube. The evaporative cooling effect is considered as the driving mechanism of surface tension gradient induced convection which effectively enhances the heat and mass transfer from the pore.

2.1.2 Self-rewetting fluids

In 1973, Vochten and Petre [21] found that the dilute aqueous solutions with high-carbon alcohol show an abnormal increase of surface tension with the rise of temperature in a specific range of temperature, which is named as self-rewetting fluids. Ono et al. [22] employed maximum bubble pressure method to measure surface tension of high-carbon alcohol aqueous solutions (butanol and pentanol) and found that pure high-carbon alcohols show a monotonically decreasing relationship of surface tension with temperature while their aqueous solutions at different alcohol concentration display self-rewetting behavior with increasing surface tension in specific temperature range (Fig. 2.6). Therefore with temperature gradient falling in this specific range, the part of higher temperature possesses higher surface tension in self-rewetting fluid. Due to inherent motion from lower surface tension place to higher surface tension place, self-rewetting fluid will flow towards higher temperature area, which is driven by inverse Marangoni force. On basis of this assumption, Ouenzerfi and Harmand [23] conducted experiments by depositing 3 vol.% butanol aqueous mixture droplets on silicon or borosilicate glass

substrates where a linear temperature gradient is produced. Through optical and infrared cameras, they investigated a slight motion of droplet towards the warmer substrate area caused by inverse Marangoni effect (Fig. 2.7).

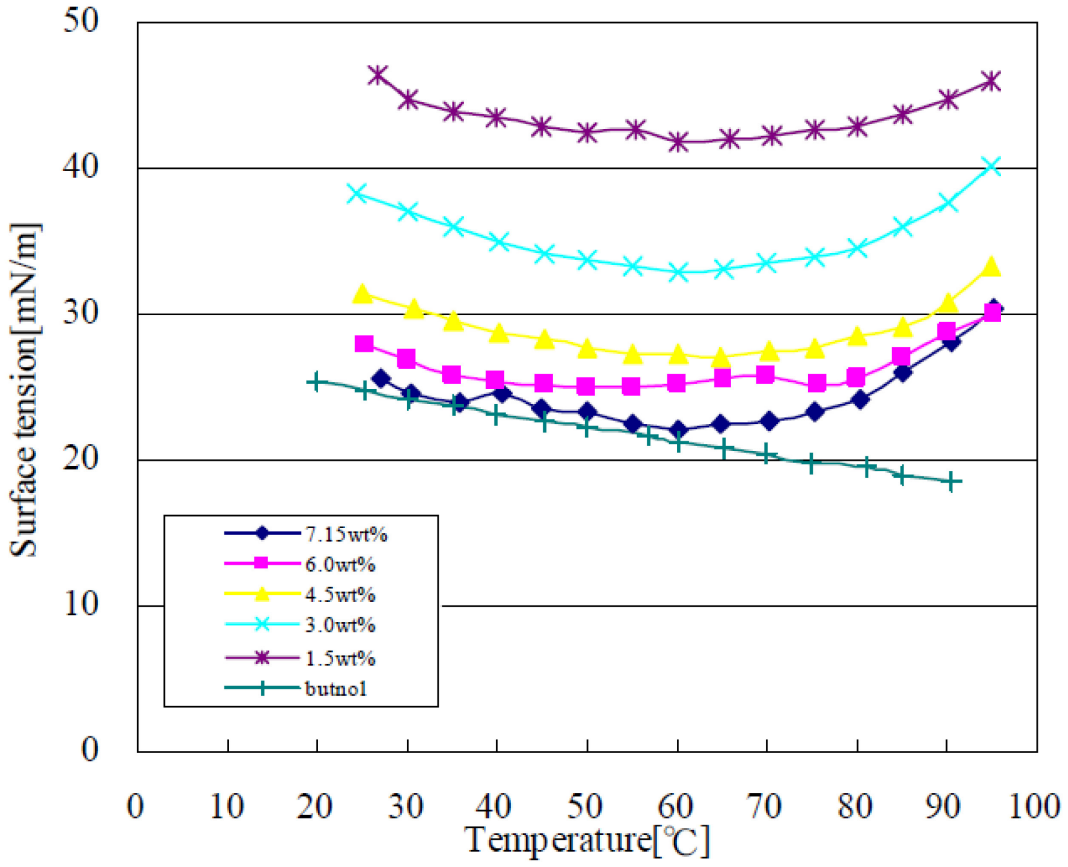

(a) Butanol

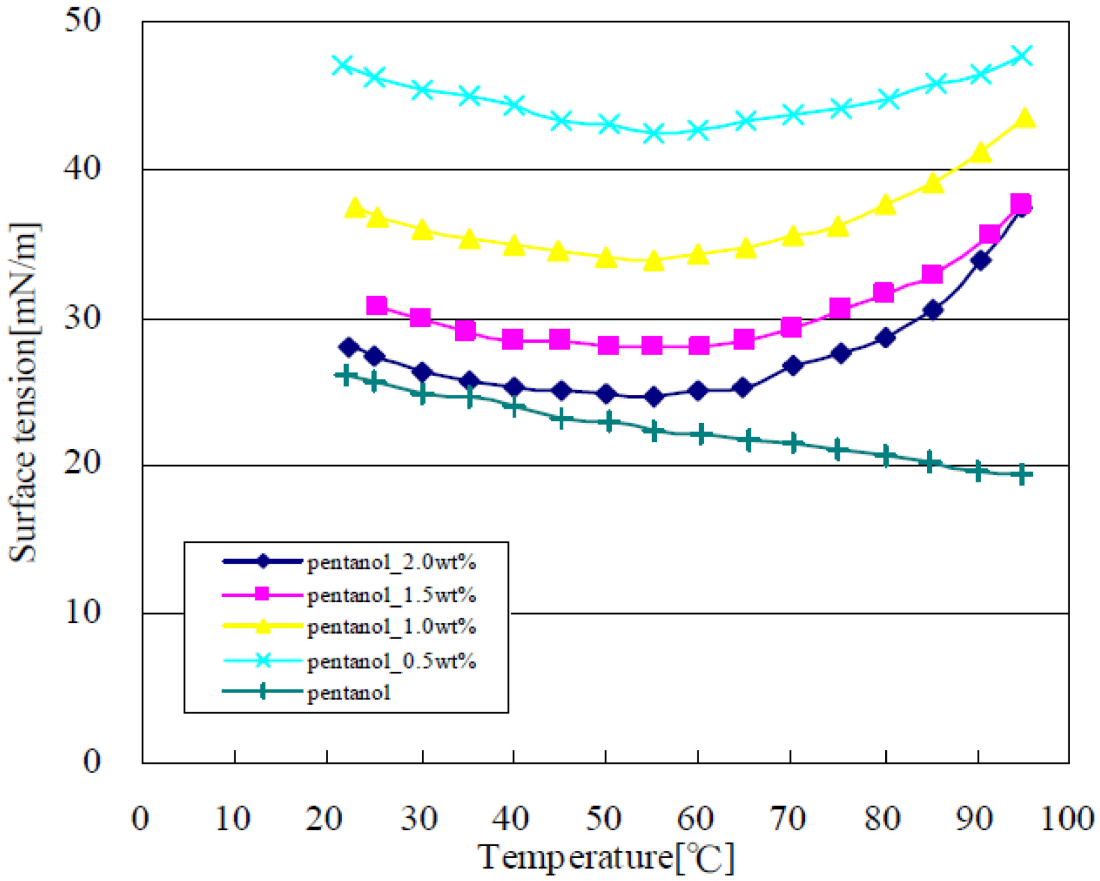

(b) Pentanol

Figure 2.6 Measurement results of surface tension for (a) butanol and butanol aqueous solutions, (b) pentanol and pentanol aqueous solutions by maximum bubble pressure method. Image taken from Ref. [22].

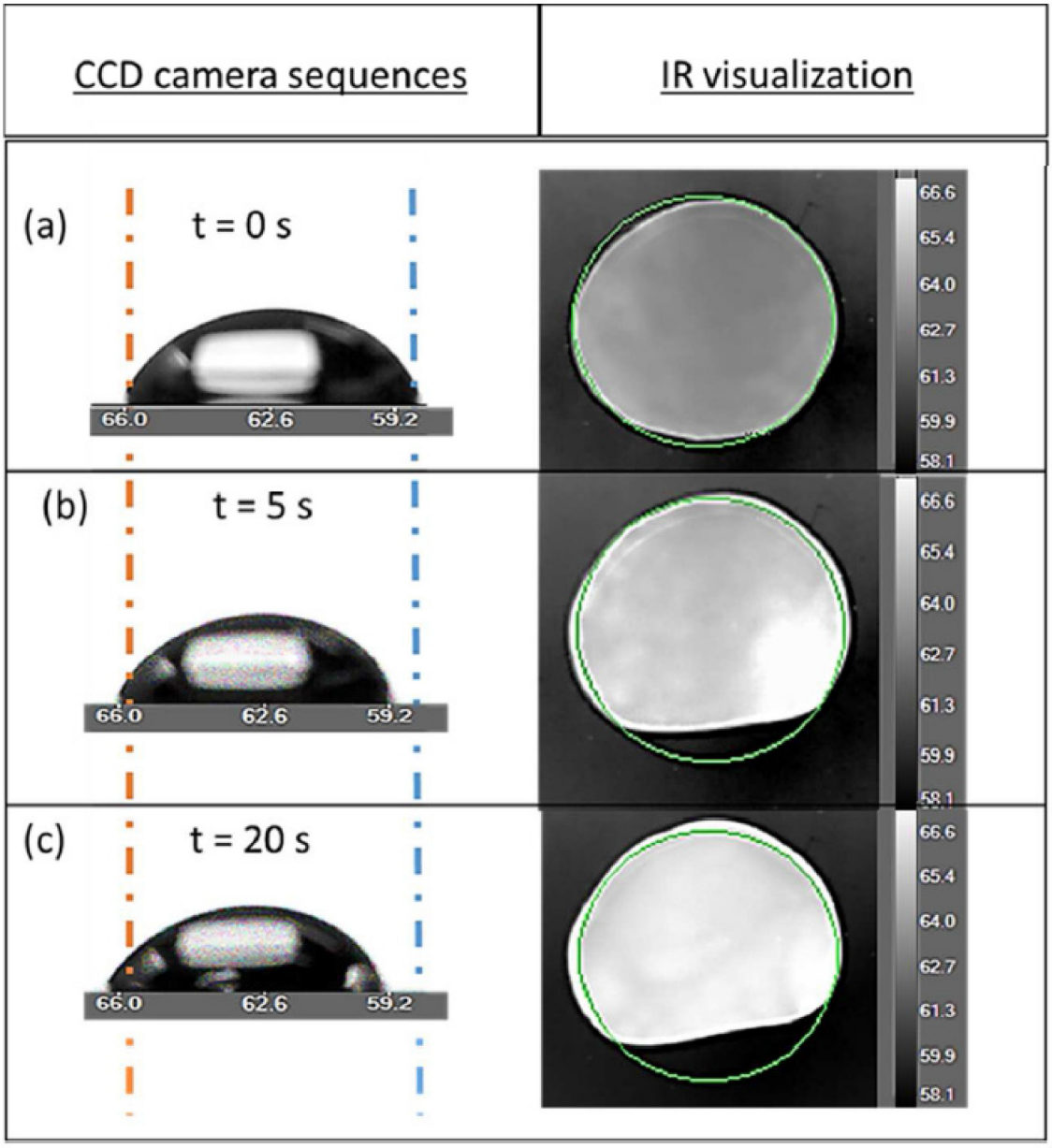

Figure 2.7 Snapshots from optical and infrared cameras of self-rewetting fluid droplets in specific temperature range at different instants. A temperature gradient is generated on substrate surface. Image taken from Ref. [23].

According to the abnormal behavior of self-wetting fluids, one important application of self-rewetting fluid is for the design of wickless heat pipe under microgravity condition. In space environment, the gravitational force is not strong enough to bring working fluid back to evaporation section and the wickless structure can contribute to lightweight design and simplified production of heat pipe. The optimized design of heat pipe is that the Marangoni flows driving the working fluid from condenser to evaporator are induced by both temperature and alcohol concentration gradients [24]. Even under terrestrial condition, Hu and al. [25] observed enhanced heat transfer and reduced capillary pressure gradient by applying self-rewetting fluid in micro oscillating heat pipes which is compared to that for the case of deionized water. The improved wetting situation at evaporation section and the effective recurrence with less capillary resistance make contributions to the ameliorated thermal performance of heat pipes. Savino et al. [26] conducted at terrestrial condition and at microgravity condition with wickless heat pipe containing self-rewetting fluid and pure water. Lower thermal resistance was observed during the performance of heat pipe filled with self-rewetting binary solution by comparing to that with pure water. Furthermore, the heat pipe filled with self-rewetting fluid have the similar heat transfer efficiency no matter under terrestrial or reduced gravity condition while the thermal performance of heat pipe filled with pure water is deteriorated in the parabolic flight.

2.2 Nanofluids

An innovative heat transfer medium with suspension of nanoscale particles is expected to possess extremely high thermal conductivity, which is termed as nanofluid by Choi et al.

[27]. Nanometer-sized particles of metal, metallic oxide, carbon nanostructure, whose inherent thermal conductivity is quite higher than that of common liquid, are employed in preparation of nanofluid in order to enhance thermal conductivity of convention heat transfer fluids such as water, engine oil and ethylene glycol. The advantages of nanofluid are highlighted in increased heat exchange area at solid/liquid interface, improved dispersion homogeneity and stability, reduced fill quantity, reduced probability of nanoparticle obstruction and controllable physical and thermal properties by changing nanoparticle loading [28]. With above mentioned benefits, nanofluid is considered as a potential high efficiency working fluid for the design of next generation heat exchanger.

2.2.1 Preparation methods

Preparation methods are crucial to the application of nanofluid, which will affect suspension stability, dispersion homogeneity, physical and thermal properties of nanoparticle suspension solution. In general, nanofluid preparation methods can be classified in single-step method and two-step method. The single-step method is based on Vacuum Evaporation onto a Running Oil Substrate (VEROS) method, which was originally developed by Yatsuya et al. [29] to produce metallic nanoparticles. The basic principle of VEROS method is that an electron beam vaporized pure metal under vacuum condition and then nanometer-sized metallic particles condense on a rotating substrate covered by radially outward moving oil. The nanoparticle suspension before drying is nanofluid. Henceforth VEROS method was modified by Wagener et al. [30] with employment of high pressure magnetron sputtering and improved by Eastman et al. [31] with direct condensation of metallic nanoparticles on a flowing ethylene glycol. Furthermore, the other single-step methods such as chemical reduction under microwave

irradiation [32] and vacuum submerged arc nanoparticle synthesis system (SANSS) [33] had been developed in recent decade. The advantages of sing-step method are minimal nanoparticle agglomerations and excellent stability, but only the liquids with low vapor pressure are appropriate for base fluid. The two-step method is more extensively applied in nanofluid preparation, which consists of nanoparticle synthesis and nanoparticle dispersion in base fluid. The industrialized nanopowder production simplifies the preparation process of nanofluid and makes large scale nanofluid synthesis become possible. Nanoparticles of pure metal [34-36], metal oxide [37-41] and carbon nanostructure [42-45] are successfully dispersed into base fluid with durable stability. Compared to single-step method, two-step method has a wider application range but the limit is the aggregation of nanoparticles due to high surface-activity. Thus the improvement of stability is an indispensable problem in two-step nanofluid preparation.

2.2.2 Stability enhancement methods

Some physical techniques are used in preparing stable nanofluid, such as ultrasonic vibration, magnetic force agitation, high-shear mixing, bead milling etc. Yu et al. [46] prepared ZnO ethylene-glycol-based nanofluid in ultrasonic bath and they observed a rapid decreasing of average nanoparticle size during first 3h of ultrasonification with the ending of approximate 210 nm. During preparation of ZnO nanofluid, Moosavi et al [47] used magnetic stirring to homogenize nanoparticle suspension which shows excellent stability for several months. Longo and Zilio [39] prepared TiO_2 and Al_2O_3 aqueous nanofluid by mechanical stirring and ultrasonification to improve the stability. The average size measurements of both nanofluids indicate that with the aid of

ultrasonification the nanofluid has a more homogeneous and stable dispersion than that with simple mechanical stirring.

The other technique concerns the surface properties of nanoparticle, which can be distinguished by surfactant addition and surface property modification. The surfactant used to improve particles separation and prevent clusters is also called dispersant which is composed of not only a hydrophilic polar head group but also a hydrophobic tail group. Surfactant can create a connection between nanoparticles and base fluid at solid/liquid interface. In the light of head portion, surfactants can be classified in four groups: nonionic without any charged head group, cationic with positive charged head group, anionic with negative charged head group, and amphoteric with zwitterionic head group. The surface property modification technique is to add hydrophilic groups on the surface of nanoparticle by chemical reaction. This functionalization method is frequently applied in the preparation of carbon nanotube solutions to improve suspension stability. In common use, the physical methods comes with the surface properties methods as a supplement. In the preparation of ZnO nanofluid, Moosavi et al [47] added ammonium citrate as dispersant before magnetic stirring and the collective effect leads to a stable state as long as several months. Bobbo et al. [48] tested several physical treatments and different dispersants in the preparation of single wall carbon nanohorns (SWCNH) and TiO_2 water-based nanofluids. Homogenization stands out from physical techniques while sodium dodecyl sulfate (SDS) and polyethylene glycol (PEG) are the most appropriate dispersants for nanofluids of SWCNH and TiO_2 respectively. Multi-wall carbon nanotubes (MWCNTs) were functionalized by Lamas et al. [49] with the treatment of nitric and sulfuric acid. And then treated MWCNTs were rinsed by deionized water and

dried in an oven. After 60 min physical treatment combined of magnetic stirrer and ultrasonic vibrator, MWCNTs nanofluid stays stable for more than 24 hours. However, both surfactant and functionalization can lead to an increase in thermal resistance between solid surface of nanoparticles and liquid phase, which is opposite to the aim of heat transfer enhancement. The equilibrium between stability and thermal conductivity becomes an interesting subject in the application of nanofluids.

2.2.3 Applications

Nanofluids prepared by different combinations of nanoparticles and base fluids exhibit various characteristics such as extraordinary thermal conductivity, intensive mass transfer, efficient heat absorption, excellent lubrication, magnetic property, antibacterial and drug-delivery activities, and tunable optical property, which bring about an wide-ranging application in energy storage [50-52], solar technology [53-56], bubble absorption [57-60], nanolubricants [61-64], magnetic sealing [65-67], biomedicine [68-73], and optical filters [74,75]. The most important application base on exceptional thermal conductivity is for improving heat transfer efficiency including micro-electronic cooling [76-78], fuel combustion [79-82], industrial boiling [83-85] and cooling [86,87], nuclear reactor cooling [88-90], and building heating system [91,92].

2.3 Conclusions

This chapter presents two novel and potential working fluid applied in heat transfer enhancement of heat pipe: binary solution and nanofluid. A review of experimental, theoretical and numerical studies in literature for thermal performance and involved

mechanism of binary solution as well as preparation methods and stability enhancement techniques of nanofluid is accessible in present chapter. Binary solution reveals more complex evaporation behavior than single-component liquid. Concentration gradient induced Marangoni flow increases mass and heat transfer within droplets of binary solution, which has been reported by numerous researchers. Furthermore the motion of self-rewetting fluid droplet towards warmer area has been observed. Both Marangoni effect and self-rewetting property can contribute to the development of wickless heat pipe under microgravity condition. In this thesis, Chapter 3 introduces a combination of infrared and acoustic technique to track alcohol variation during evaporation process of alcohol-water mixture droplet and Chapter 4 provides a series of empirical equations to predict evaporation rate of 1-butanol aqueous droplet including solutal and thermal Marangoni effect, both of which are devoted to the full understanding of mass and heat transfer mechanisms within binary solution droplets. For nanofluid, the biggest challenge is the balance between suspension stability and thermal conductivity. In this study, PEGylation is employed to functionalize graphene nanoparticle in order to obtain long-term stable nanofluid. An evaporation performance comparison between functionalized and non-functionalized graphene is effectuated and then the effects of nanoparticle concentration and substrate temperature are investigated. Experimental results and analysis are available in Chapter 5.

Chapter 3 Alcohol Concentration Tracking of Binary Sessile Droplets during Evaporation

This chapter is based on the published work in Langmuir in 2016 [93]. The author of this thesis contributed to the part of infrared method via designing and performing experiments, analyzing experimental results and writing the section of manuscript concerning visual investigation. Dr. M. Toubal, Dr. J. Carlier and Prof. B. Nongaillard took charge of acoustic method part including experiment design and execution, experimental results analysis and manuscript writing. Prof. S. Harmand and Prof. M. Bigerelle supported the author of this thesis for the writing of the manuscript and gave approval to the final version.

3.1 Abstract

Deposited on the hydrophobic silicon, the evaporation of droplets of three pure liquids (water, 1-butanol and ethanol) and four binary solutions (5 wt.% 1-butanol water-based solution and 5 wt.%, 25 wt.% and 50 wt.% ethanol water-based solutions) were investigated. A drop shape analyzer was used to measure the contact angle, diameter and volume of droplets. At the same time, an infrared camera was utilized for the infrared thermal mapping of droplet's surface. An acoustic high frequency echography technique was, for the first time, applied to track the alcohol concentration in a binary solution droplet. The evaporations of pure alcohol droplets were executed at different values of

the relative humidity, among which the behavior of pure ethanol evaporation was notably influenced by the ambient humidity as a result of high hygrometry. The evaporations of droplets of water and binary solutions were performed at a temperature of 22°C and a mean humidity of approximately 50%. The times when the alcohol exhausts in the droplets estimated by the acoustic method and the visual method were similar for water-1-butanol mixture; however, the time estimated by the acoustic method is longer compared to visual method for water-ethanol mixture due to the residual ethanol at the bottom of the droplet.

3.2 Introduction

In recent decades, many experimental [94-99] and theoretical studies [97,100-104] have investigated the process of evaporation of drops, which has a wide range of applications, e.g., ink-jet printing [105,106], DNA mapping [107,108], combustion engineering [109,110], and cooling system [111,112]. With optical and infrared techniques, the measurement of the parameters of a droplet (contact angle, base radius and height) can contribute to full understanding of the evaporation process. Moreover the dynamic evaporation of a binary mixture drop which can contain both of constant contact angle regime and constant contact radius regime is more complicated.

At ambient conditions, the evaporation process of the water-ethanol mixture drops was divided in three stages: the first stage conforms to the behavior of the pure volatile component evaporation; at the last stage, the drop evaporates in accordance with the less volatile component; and between the aforementioned stages, there is an intermediate (transitional) stage, where the contact angle clearly increases with nearly constant volume

[12]. Christy et al. [13] also showed that the evaporating of water-ethanol mixture sessile drop went through three distinct stages when they studied the interior flow in droplet with PIV technology: 1. chaotic regime, dominated by multiple vortices driven by concentration differences as a result of the preferential evaporation of ethanol; 2. transition regime, characterized by an exponential decay of vortices with the migration of the remaining vortices toward the drop periphery and a spike of the radial velocity along the drop base; 3. the third stage, characterized by the evaporation driving outward flow to the contact line, acting exactly the same as pure water drops. During the evaporation process of water-ethanol mixture, O'Hare and Spedding [113] found that the evaporation rate of water component maintained a nearly constant value, despite the continuous decrease of the actual ethanol concentration. Furthermore, Liu et al. [114] discovered that the evaporation behavior of water-ethanol mixture drop can be more complex: ethanol did not finish thoroughly at the end of transitional stage; rather, until the end of evaporation, a part of the residual ethanol still remained in the drop. The condensation of water vapor appeared as the mixture drop began to evaporate at high ratio of ethanol in the drop and high vapor pressure of water in the background gas.

Despite the numerous research studies performed on the evaporation of water-based binary alcohols solutions, there is still a lack of understanding of the evolution of alcohols concentration during evaporation. In this study, the dynamic evaporation of sessile drops of three pure liquids (water, 1-butanol and ethanol), as well as water-1-butanol and water-ethanol mixtures, was investigated using a complementary original dual-track approach combining optical and infrared techniques on one hand and acoustics on the other hand. While the optical and infrared techniques provide macroscopic

information of the phenomenon at the drop surface, the use of acoustics gives access to local interface exchange mechanisms at the bottom of the drop.

An acoustical method has been developed in our laboratory for characterizing solid/ liquid interfaces at micro/nanometers scales. First, the focus was on the wetting of droplets of various surface tensions on hydrophobized textured structures [115]. The surface tension threshold of the droplet was correlated to the observation of the transition from Cassie-Baxter to Wenzel state. Another targeted application was the determination of cleaning efficiency in the nanoelectronics fabrication process. Not only did the ultrasonic technique in the tracking of Cassie - Wenzel transition on microstructures during the evaporation process of a droplet on a microstructured surface [116,117] but also in nanostructures wetting characterization on periodic surfaces [118].

In the case of binary drop evaporation, the alcohol concentration tracking, which is the main interest of ultrasound techniques, is due to the high contrast of mechanical impedances between certain alcohols, such as 1-butanol and ethanol, trapped at the interfaces and liquids. Moreover, ultrasound techniques do not require any optical transparency. This sensitivity enables the monitoring of the evaporation kinetics of droplets of some water/alcohol mixtures at a plane of solid/liquid interface by the tracking of the concentration evolution at the interface between the droplet and the support. Depending on the binary alcohol concentration of the drop, the mechanical impedance of the liquid and the acoustic reflection coefficient will be modified. Due to a pre-established calibration curve of the reflection coefficient which depends on the alcohol concentration of droplet, it is possible to determine the concentration of alcohol on line at the interface by the acoustic reflection coefficient measurement.

3.3 Experimental Setup

Two separate devices are used, one for optical and infrared measurements, and the other for acoustic reflection coefficient measurement. In both cases, the droplets are left evaporating on the hydrophobized (100) silicon substrate treated with PFTS (PerFluorodecylTrichloroSilane). Measurements are made at a temperature of 22 °C and a mean humidity of approximately 50%. Moreover, the influence of humidity, namely 20%, 50% and 56%, on infrared and optical measurements is considered for the case of pure alcohol's evaporation.

3.3.1 Optical and infrared measurements

The substrates are placed in a vapor chamber (14 cm × 12.4 cm × 7.5 cm), in which the ambient temperature and the relative humidity can be controlled (Fig. 3.1 (a)). Air inside the chamber is at rest. The top of the vapor chamber has a sapphire window for the infrared camera and a hole for passing the syringe. The infrared camera (FLIR X6580SC, 640×512 pixels, 15µm detector pitch) is installed on top to be used for infrared thermal mapping and visualization of thermal instabilities on the surface of the droplets. The exploitation of dynamic infrared videos provides a good visualization of alcohol cells' motion on the droplet surface and consequently the alcohol life time during evaporation as water and alcohol have different emissivities. A Kruss® Drop Shape Analyzer is used to measure the contact angle, volume, diameter and height of sessile droplets during evaporation. A side view CCD camera (Allied Vision Technologies, 780×580 pixels) is used to record the evaporation process of the droplets for profile analysis.

3.3.2 Acoustic measurements

Measurements are made under controlled atmosphere thanks to an air-conditioning system. A prober system Cascade PM8 is used to control at the micro-scale the position of the S/G (Signal/Ground) probe on a piezoelectric transducer as small as 50 μm in diameter to achieve the electrical measurements (Fig. 3.1 (b)). The specificity of the probe is the possibility to achieve the electrical contact at the backside of the wafer on which the piezoelectric transducer was fabricated. These probes are connected to a Rhode & Schwarz ZVA8 Vector Network Analyzer. The droplet is deposited on the top side of substrate via a microfluidic device. A backside view camera is used to check the alignment of the probe and the transducer. The top view camera helps to check the correct position of the drop above the transducer surface, while the lateral view camera gives information of contact angle.

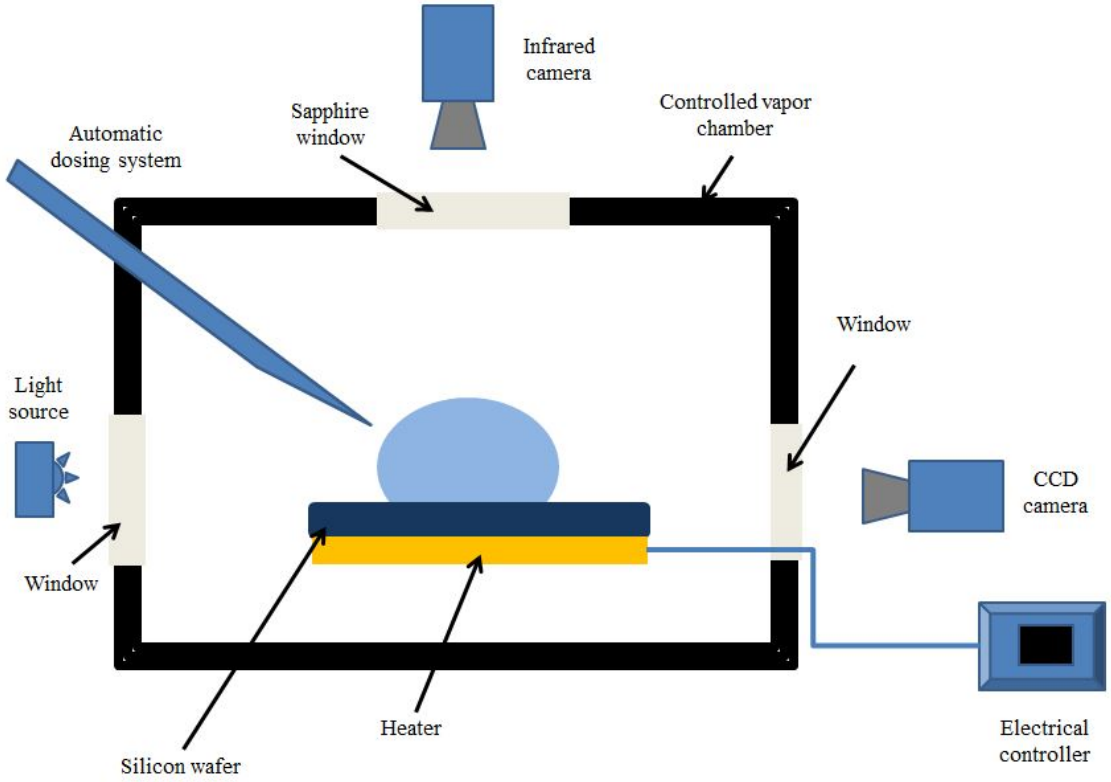
Infrared camera
Sapphire window
Controlled vapor chamber
Automatic dosing system
Window
Light source
CCD camera
Window
Heater
Silicon wafer
Electrical controller

(a)

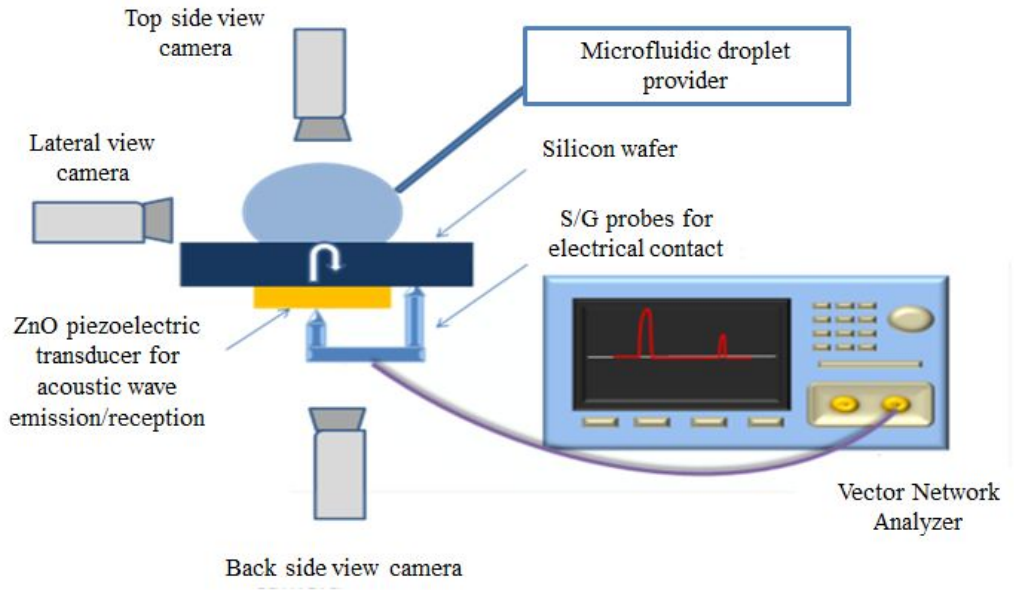

(b)

Figure 3.1 Schema of the experimental setup: (a) workbench of modified Kruss® Drop Shape Analyzer and infrared camera; (b) acoustic workbench.

The acoustic method is based on the high-frequency echography principle. A high frequency (1 GHz) longitudinal wave is generated by ZnO piezoelectric transducers fabricated on the backside of the (100) silicon substrate on which the solid/liquid interface is characterized. The diameter of the ZnO transducers is about 250 µm. The thickness of the silicon substrate is about 500µm. $S_{11}(f)$ scattering parameter (ratio of the complex amplitudes of the reflected and incident signals) is measured by using a Suss Microtech probe coupled with a Hewlett Packard 8753 Vector Network Analyzer. This parameter is the result of two separate, electric (S_{11}^{el}) and acoustic (S_{11}^{ac}) contributions.

$$S_{11}(f) = S_{11}^{el} + K\, S_{11}^{ac} \tag{3.1}$$

K includes electromechanical conversion effects at the interfaces.

S_{11}^{ac} parameter results from the superposition of the acoustic waves generated from all the reflected waves at the interface.

An inverse Fourier Transform applied on the $S_{11}(f)$ signal makes it possible to separate the acoustic contribution from the electric one. These two signal contributions are separated by a delay corresponding to the propagation in the substrate. The signal, in the time domain, windowed on the useful echo corresponding to the first reflected echo is then processed to determine the reflection coefficient.

From a theoretical point of view, a plane of the acoustic wave propagating at normal incidence at an interface separates two media of acoustic impedances Z_1 and Z_2; the absolute value of the reflection coefficient R in amplitude can be calculated using the following equation:

$$|R| = \frac{Z_2 - Z_1}{Z_1 + Z_2} \tag{3.2}$$

$Z = \rho c$, ρ is the density of the medium and c is the acoustic velocity of the wave propagating inside the medium. In our case, Z_1 is the acoustic impedance of the liquid, whereas Z_2 is that of the (100) silicon substrate. An online assessment of the evaporation kinetics of droplet is feasible due to the measurement of this reflection coefficient.

The width of the acoustical pulse is 5 ns. It corresponds to five times the period of the working frequency of 1GHz. Since the wavelength λ_l in water is about 1.5 μm, one can consider that the wave propagates over a distance of 5 times the wavelength λ_l in the

liquid, namely 7.5 μm. Beyond this thickness, the acoustic wave undergoes a strong attenuation. Since we process droplets of 1 μL, the corresponding diameter and height are about 1.5 mm each. The information gathered is then limited to a few micrometers inside the drop at the bottom.

3.4 Experimental Results

3.4.1 Calibration of the acoustic measurement method

For calibrating our acoustic device, water is used as a reference liquid. The acoustic reflection coefficient is calculated from the values of the density, and the acoustic velocity of both silicon and water found in the literature. Several precautions are taken to improve the accuracy of the measurements. Temporal drifts are minimized by the use of 2 identical transducers, one for reference to air, and the other for measurement at silicon/liquid interface. Reference to air is first measured on each case. The adjustment factor $|R|_c$ is equal to the ratio of the peak amplitudes *A22* and *A11*, which are the reflection coefficients measured with each probe on each transducer.

$$|\mathrm{R}|_{\mathrm{c}} = \left(\frac{\mathrm{A_{22}}}{\mathrm{A_{11}}}\right)_{\mathrm{air}} \tag{3.3}$$

The standardized reflection coefficient, R_{norm} at the solution (sol) / silicon interface is then deduced as:

$$|\mathrm{R}|_{\mathrm{norm}} = \frac{\left(\frac{\mathrm{A_{22}}}{\mathrm{A_{11}}}\right)_{\mathrm{sol}}}{\left(\frac{\mathrm{A_{22}}}{\mathrm{A_{11}}}\right)_{\mathrm{air}}} \tag{3.4}$$

A drop of water of approximately 1 μL is deposited on the surface of the planar (100)

silicon substrate. According to Eq. 3.2, the reflection coefficient at silicon/water interface is deduced to be 0.8595. Reliability can be assessed according to the stability and the accuracy of the measurement compared to the theoretical value; it was determined to be 0.02%.

The physical properties of the pure liquids and their studied mixtures as well as the (100) silicon substrate at a temperature of 22°C are reported on Tab. 3.1. ρ is the density, γ the surface tension, P_{sat} the saturation vapor pressure and c the acoustic velocity. The volatility is measured through the saturation vapor pressure P_{sat}. The higher the value of P_{sat}, the more volatile the liquid is. Note that P_{sat} is given for large volumes of liquid.

	ρ ($kg \cdot m^{-3}$)	γ ($mN \cdot m^{-1}$)	P_{sat} (kPa)	c ($m.s^{-1}$)
Water	998	72.80	2.65	1488.319[119]
(100) Silicon	2330			8433.8[120]
1-Butanol	809	24.67	0.80	
Water+5%1-Butanol	989	33.60	2.56	
Ethanol	789	22.31	5.80	
Water+5%ethanol	988	56.41	2.81	
Water+25%ethanol	946	36.09	3.44	
Water+50%ethanol	894	28.51	4.23	

Table 3.1 Physical properties of fluids and (100) silicon at 22 °C and 1 atm.

3.4.2 Evaporation of drops of pure liquids

The immediate attention was focused on pure liquids, namely pure butanol and pure ethanol. The relative humidity of 20% and 56% are the minimal and maximal value, respectively, that the vapor chamber can attain; moreover, 50% was chosen as a mean relative humidity. Acoustic measurements were made in a surrounding humidity of approximately 50%.

Pure butanol

(a) Optical and infrared investigation

For each liquid, we measured the contact angle, the diameter and the volume of droplets versus time and deduced $V^{2/3}$. All of experiments were repeated five times to guarantee a good repeatability. The plots of contact angle and $V^{2/3}$ versus time are presented in Fig. 3.2. The evaporation of pure 1-butanol drops can be divided in two stages: initially, the stage of constant contact radius where contact angle decreased slightly, followed by the stage of constant contact angle during most time of evaporation. The different values of the relative humidity used had no obvious effect on the evaporation of pure 1-butanol drops.

For a spherical cap drop, the evaporation rate [121] can be given by Eq. 3.5:

$$-\left(\frac{dV}{dt}\right) = \frac{4\pi D}{\rho_L}\left(\frac{3V}{\pi\beta}\right)^{1/3}(C_s - C_\infty)f(\theta) = KV^{1/3}f(\theta) \qquad (3.5)$$

where

$$K = \frac{4\pi^{2/3}3^{1/3}D(C_S - C_\infty)}{\rho_L \beta^{1/3}}$$

$$\beta = 2 - 3\cos\theta + \cos^3\theta$$

and V is the volume of the spherical cap drop, D is the diffusion coefficient of vapor in air, ρ_L is the liquid density of drop, C_s and C_∞ are the vapor concentrations close to the drop surface and far from drop respectively, θ is the contact angle, $f(\theta)$ is the function of contact angle of the spherical cap given by the model of Picknett and Bexon [100]:

$$f(\theta)_{Picknett\&Bexon} = \frac{1}{2}(\frac{C}{R_s}) \tag{3.6}$$

For $10^\circ \le \theta < 180^\circ$,

$$\frac{C}{R_s} = 0.00008957 + 0.6333\theta + 0.116\theta^2 - 0.08878\theta^3 + 0.01033\theta^4 \tag{3.7}$$

Assuming that the diffusion of vapor molecules in air is steady and the contact angle remains constant during evaporation, Eq. 5 can be integrated between initial volume V_0 ($t \to 0$) and V_t ($t \to t$):

$$V_t^{2/3} = V_0^{2/3} - \frac{2}{3}Kf(\theta)t \tag{3.8}$$

The plots of $V^{2/3}$ versus time, as shown in Fig. 3.2, are linear regardless of the conditions of relative humidity. In the case of 56% relative humidity, according to the slopes of ours plots, $Kf(\theta)$ varies in the 1.42×10^{-5} to 1.69×10^{-5} cm^2/s range. These values are

comparable to the theoretical ones calculated from Eq. 3.5 to 3.7, which fall in the 1.22 × 10^{-5} to 1.33 × 10^{-5}cm^2/s range.

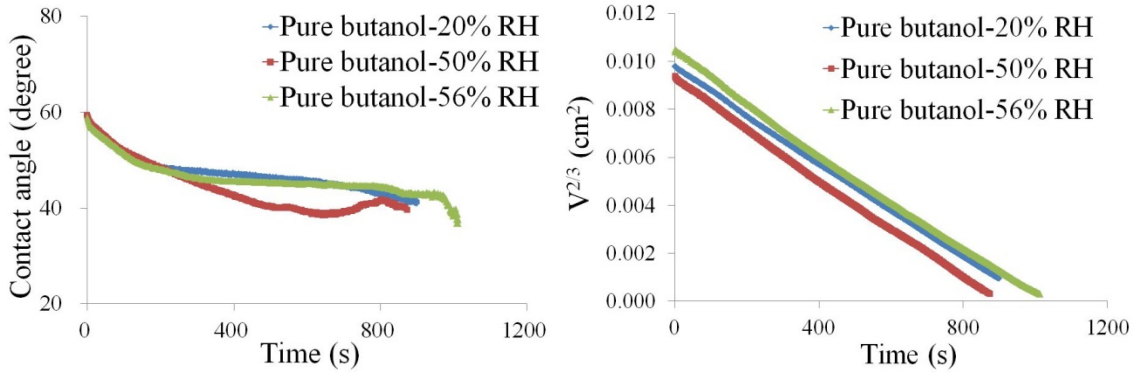

Figure 3.2 Evolutions of the contact angle and $V^{2/3}$ for pure 1-butanol droplets under different relative humidity conditions versus time.

Fig. 3.3 shows the evaporation process of the pure 1-butanol droplets at 56% relative humidity under the infrared camera (see supplementary material [122] for visualization). According to Stefan–Boltzmann law, the radiant exitance of a grey body *j* is determined:

$$j = \varepsilon\sigma T^4 \tag{3.9}$$

where σ is Stefan-Boltzmann constant, ε and T are emissivity and temperature of substance respectively. The scale in infrared thermal mapping represents the level of thermal radiation "*I*" received by infrared camera. The "*I*" level is proportional to the radiant "*j*". The Different colors correlate with different temperatures or different emissivities related to different substances. Water and alcohol in mixture droplet have the same temperature but the emissivity of water is higher than that of alcohol. Consequently there is a color contrast between water and alcohol that is visualized under infrared

camera. The normal temperature profile of a single substance droplet is that the coolest at the apex of droplet and the warmest at the contact line, then temperature varies from apex to contact line gradually. According to these infrared images in Fig. 3.3, the color consistency at the surface until the end of evaporation indicates that the temperature of droplet surface was almost homogeneous and there is no second liquid present in droplet. Moreover, the phenomenon was similar under different relative humidity conditions.

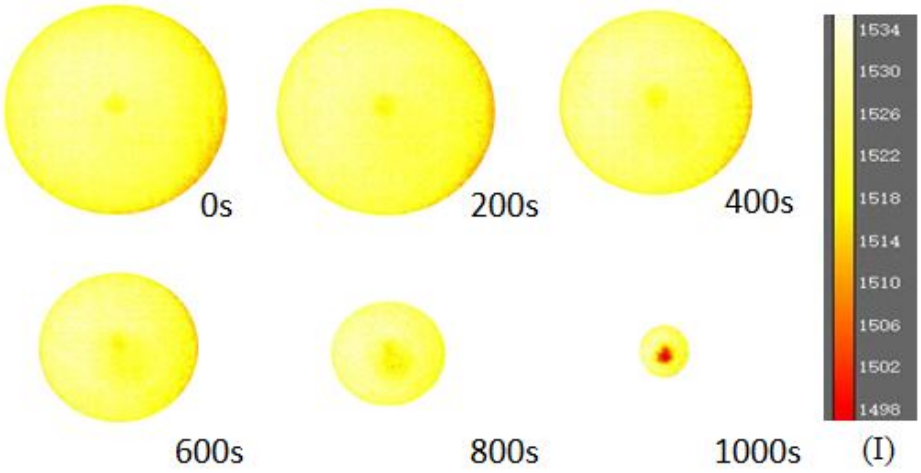

Figure 3.3. Snapshots from an infrared video of the evaporation process of a pure 1-butanol droplet at 56% relative humidity (See also the supplementary videos on line at Ref. [122]).

(b) Acoustic investigation

The reflection coefficient of pure 1-butanol drop remained constant during the evaporation process. This acoustic measurement supports the observation by optical and infrared techniques showing no influence of ambient humidity during the evaporation. These results confirm the investigation of Seaver et al. [123], who showed the very low hygroscopic power of a drop of 1-butanol during evaporation.

Pure ethanol

(a) Optical and infrared investigation

Fig. 3.4 represents the evolutions of contact angle and $V^{2/3}$ of pure ethanol droplets versus time. For these three relative humidity situations, the evaporation of pure ethanol droplet went through constant contact radius regime and then constant contact angle regime at the beginning, which is similar with the evaporation of pure butanol droplet. For the case of 20% RH, the contact angle increased slightly and then decreased until the end of evaporation after first two stages. However, for the cases of higher relative humidity, the contact angle rose rapidly to a maximal value. In particular, the case of 56% RH had a transition stage before the rapid rise where the contact angle and the diameter both decreased, and the maximal value (88°) was close to the contact angle of pure water droplet (107°). According to Young's Equation:

$$\cos\theta = \frac{\gamma_{SG}-\gamma_{SL}}{\gamma_{LG}} \tag{3.10}$$

where γ_{SG}, γ_{SL} and γ_{LG} are solid/vapor, solid/liquid and liquid/vapor interfacial tension respectively. Owing to the high hygroscopic nature of pure ethanol, water vapor condenses on the surface of pure ethanol droplet during evaporation. The liquid/vapor interfacial tension increases with the increase of water/ethanol ratio of droplet at contact line which leads to the raise of contact angle (Eq. 3.10). The condensation rate of water depends on the water vapor pressure of surrounding environment. Thus, the relative humidity can notably change the behavior of pure ethanol droplets' evaporation. The evaporation time of a drop at 56% RH was nearly triple as that of a drop at 20% RH

because the drop absorbed more water, which has a diffusion coefficient in the air much less than that of ethanol. In addition, the plot of $V^{2/3}$ can be obviously divided in two stages with different slope for higher relative humidity: initial steep stage when only ethanol evaporated, then gentle stage when contact angle reached the maximum, until the end and during which water mainly evaporated. We can conclude that pure ethanol droplet absorbs a non-negligible quantity of water during evaporation at 50% and 56% relative humidity, which has a significant effect on the evaporation of pure ethanol droplet.

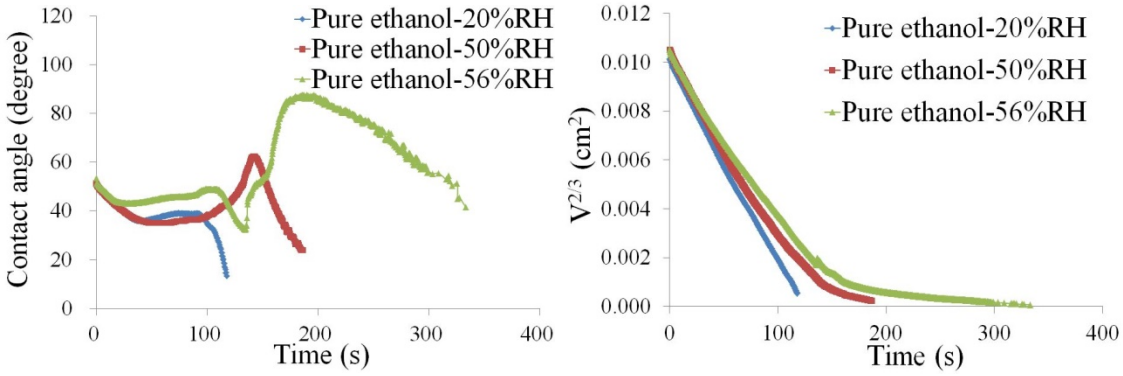

Figure 3.4 Evolutions of the contact angle and $V^{2/3}$ for pure ethanol droplets under different relative humidity conditions versus time.

Contrary to pure 1-butanol, the infrared thermal mapping using the infrared camera reveals heterogeneous zones during the evaporation process of a drop of pure ethanol. Fig. 3.5 (see also the movies on line at Ref. [122]) represents the infrared images of the case of 56% RH at different times. These snapshots show that some convection cells appeared from the beginning, demonstrating the presence of liquids of different density (ethanol and water). After 200 seconds, the drop became too small to allow for the distinction of convection cells; however, according to the analysis above mentioned, no

ethanol was present on the drop's surface, and no convection cells were found. By reducing the relative humidity to 50% and to 20%, the phenomena observed were similar and the only difference is that the convection cells were weakened and less visible. Thus, the environmental relative humidity can significantly affect the evaporation of pure ethanol droplet which absorbs water as soon as it is exposed in the air.

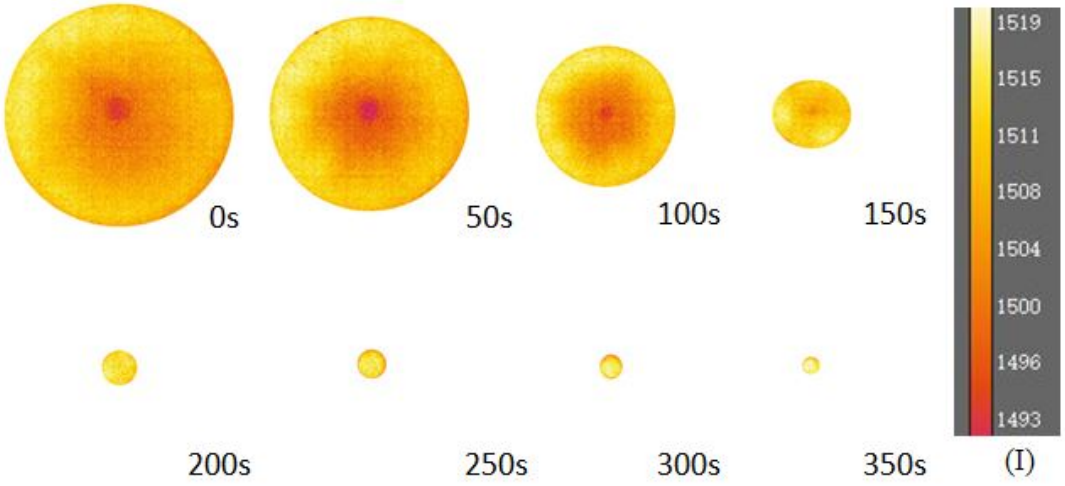

Figure 3.5 Snapshots from an infrared video of the evaporation process of a pure ethanol droplet at 56% relative humidity (See also the supplementary videos on line at Ref. [122]).

(b) Acoustic investigation

Regarding pure 1-butanol, we followed the evaporation kinetics of a drop of pure ethanol in the same conditions of temperature and humidity. One can see clearly that the ethanol drop undergoes a progressive water loading until no more alcohol remains at the bottom of the drop, when the reflection coefficient tends towards that of water and then maintains the value (Fig. 3.6). Notably, the high hygroscopic power of ethanol has been reported by

Liu et al., who demonstrated the influence of water condensation in the evaporation of water-ethanol mixtures drops [114].

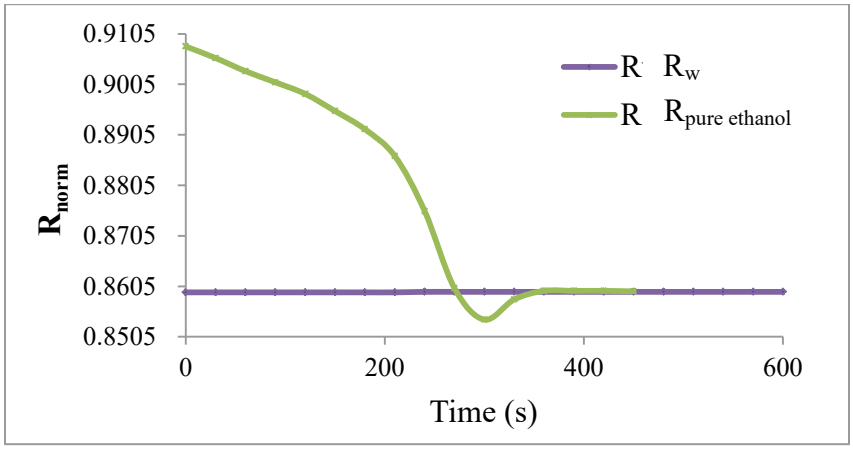

Figure 3.6 Kinetics of the acoustic reflection coefficient for a drop of pure ethanol

To the best of our knowledge, there is no reference in the literature regarding the evaporation of a sessile droplet of pure ethanol. The findings presented here constitute an original result, showing that the water vapor from the ambient humidity condenses onto the droplets of pure ethanol during evaporation, and then the solution becomes a mixture of water and ethanol.

3.4.3 Evaporation of drops of binary solutions

In the following experiments, the droplets of pure water and binary solutions were tested at a temperature of 22°C and a hygrometry of approximately 50% with the volume of 1 µL.

Water/butanol mixture

(a) Optical and infrared investigation

For the water-1-butanol mixture, the result was compared with those of pure water on the kinetics of contact angle and the plot of $V^{2/3}$. Fig. 3.7 represents the evolutions of contact angle and $V^{2/3}$ for droplets of pure water and 5% mass concentration water-1-butanol mixture. In spite of the slight decrease at the beginning, which is due to evaporation, the contact angle of pure water drop remained constant during most of the evaporation process and decreased abruptly at the end. Different from that of pure water, the contact angle of water-1-butanol mixture initially decreased and then increased until the maximal value before decreasing abruptly at the end of drop life. The plot of $V^{2/3}$ of water droplet is linear while that of water-1-butanol mixture has a slight deviation at the beginning due to the evaporation of 1-butanol.

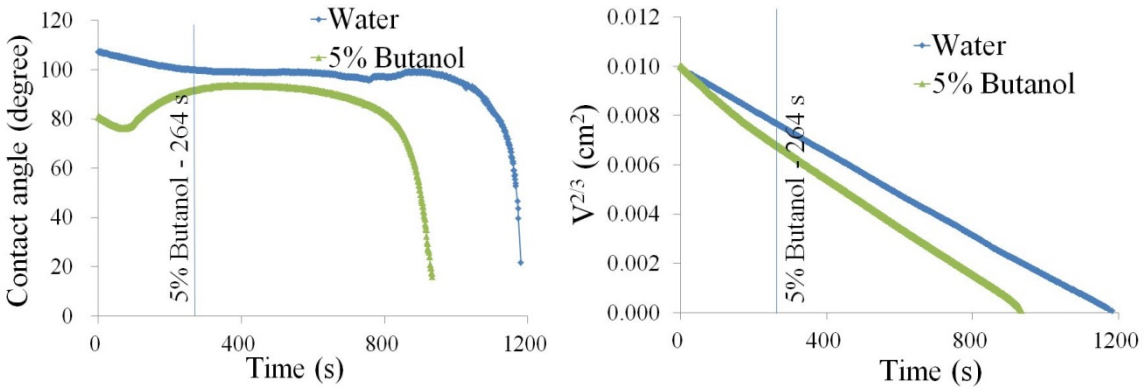

Figure 3.7 Evolutions of contact angle and $V^{2/3}$ for droplets of pure water and 5% mass concentrations water-1-butanol mixtures versus time.

Even though the diffusion coefficient of water vapor in air (0.282 cm^2/s) is much higher than that of 1-butanol vapor (0.08 cm^2/s), the ratio of evaporation rate is still lower than

the water/1-butanol component ratio. Therefore the concentration of 1-butanol near the air/liquid interface decreased which created a concentration gradient between surface and bulk. For replenishing the part evaporated on the surface, the 1-butanol inside the drop flowed outward to generate the convection cells. Fig. 3.8 shows the evaporation process of the water-1-butanol mixture droplets with 5% butanol mass concentration under the infrared camera (see also the movies on line at Ref. [122]). At the beginning, the motion of convection cells is fierce and random without any thermal pattern. Since the drop evaporated at ambient temperature, there is no large temperature gradient in the droplet. Therefore, the color difference of convection cells is due to emissivity difference, which indicates different substances, instead of temperature difference. As evaporation progressed, convection cells became smaller and slowed down towards the contact line until disappeared. With these infrared videos, we can visually identify the time when the thermal instabilities disappeared and the color distribution on droplet surface became stable as the moment when the 1-butanol in the droplet exhausted. The duration of 1-butanol is marked on Fig. 3.7, where the 1-butanol disappeared at 264 seconds. The finish point determined by infrared video is also the moment when contact angle reached maximal value close to that of water and the constant contact angle stage began.

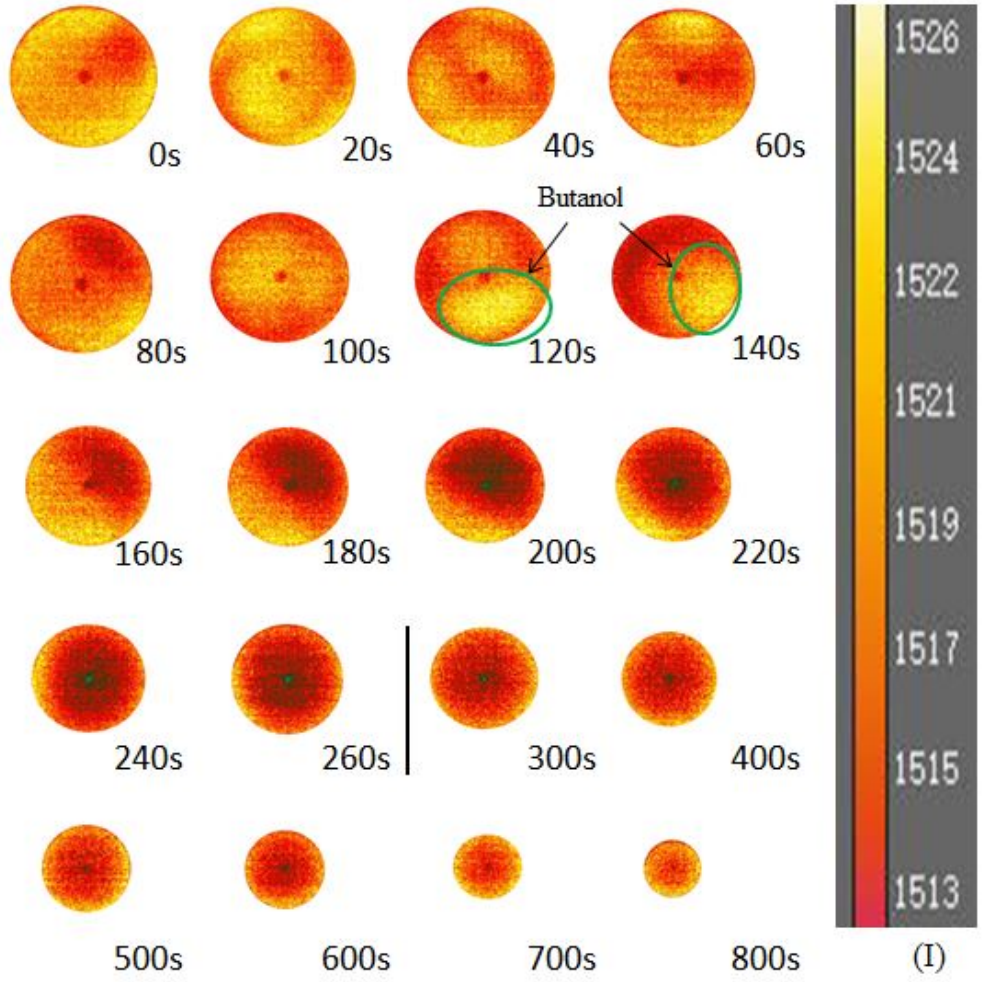

Figure 3.8 Snapshots from an infrared video of the evaporation process of a water-1-butanol mixture droplet containing 5 wt.% 1-butanol at ambient temperature (See also the supplementary videos on line at Ref. [122]).

(b) Acoustic investigation

From the acoustic reflection coefficient measured during the evaporation of a 5% mass concentration water-1-butanol mixture drop, one can follow the concentration decrease of 1-butanol inside the drop at the liquid/substrate interface. Beforehand, the calibration curve giving the acoustic reflection coefficient as a function of mass concentration is

established.

Because the limit of solubility of 1-butanol is reached for a mass concentration of approximately 7.3%, the upper limit is fixed here at C_m = 7%. Fig. 3.9 is the result of the average of a series of 3 measurements performed under the same conditions. The dispersion is in the range of 0.03%.

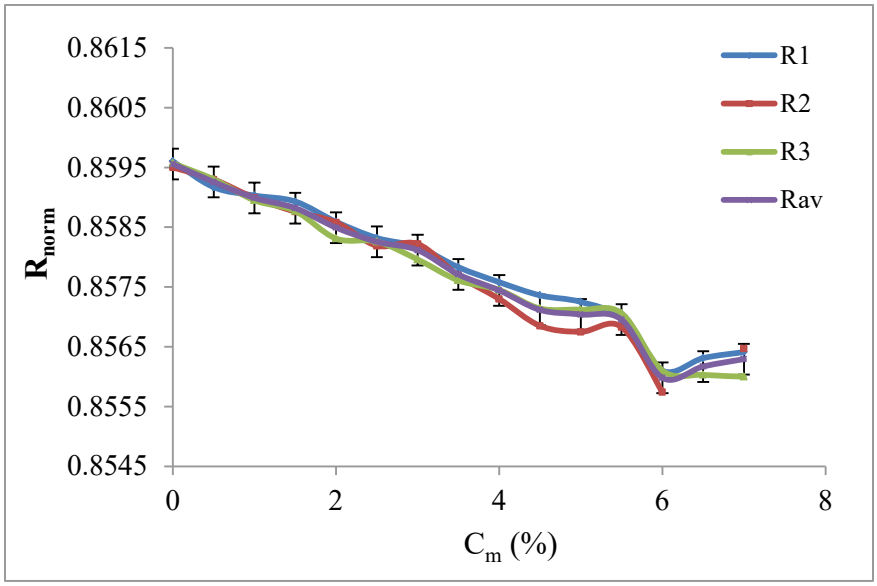

Figure 3.9 Calibration curve for 1-butanol at a temperature of 22°C and a hygrometry of 50%.

Starting with a mass concentration of 5%, the alcohol concentration at the bottom of the drop during evaporation is represented on Fig. 3.10. The curve is an average for a series of five measurements from which the necessary time $t_{C=0}$ for 1-butanol concentration to decrease to zero can be determined. This time is estimated to t_{C0} = 220 ± 15 s.

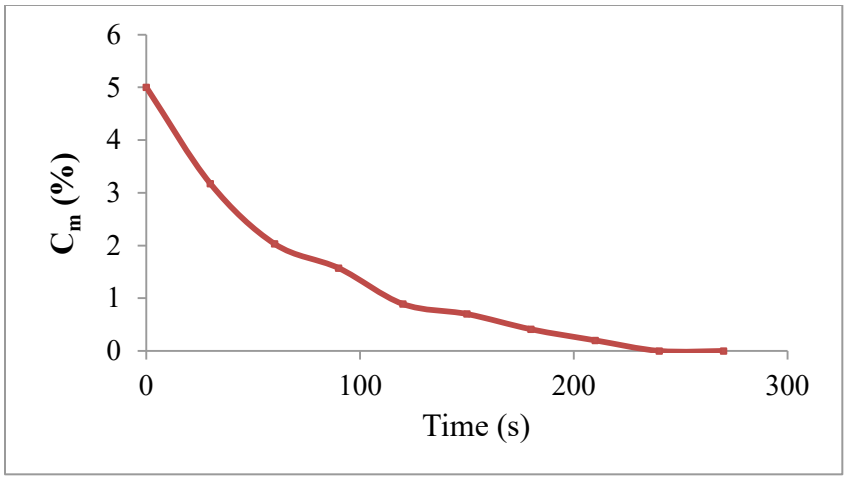

Figure 3.10 Mass concentration kinetics during evaporation of a droplet of 5 wt.% of 1-butanol deduced from the measurement of the acoustic reflection coefficient.

Evaporation of water-ethanol mixtures

(a) Optical and infrared investigation

Equally, Fig. 3.11 displays the evolutions of contact angle and $V^{2/3}$ for droplets of pure water, 5%, 25% and 50% ethanol mass concentrations of water-ethanol mixtures. Due to the tiny mass concentration of ethanol, the contact angle of a droplet containing 5 wt.% of ethanol developed versus time analogously as pure water. With the increase of mass concentration, the behaviors of the droplets with 25 wt.% and 50 wt.% of ethanol appears similar to that of water-1-butanol mixture, and the evolutions of contact angle can be divided in the same four stages: decline, increase, smooth and decrease at the end. According to the infrared videos on line [122] (Fig. 3.12 and Fig. 3.13), we can notice the appearance of the same thermal instabilities as the case of water-1-butanol mixture and also identified the time when convection cells disappeared while color distribution on droplet surface became stable on Fig. 3.11. On account of the very short duration of

convection cells, the infrared video for a droplet of 5 wt.% water-ethanol mixture is not shown here. The durations of ethanol are 5 seconds, 55 seconds and 100 seconds for 5 wt.%, 25 wt.% and 50 wt.% water-ethanol mixtures, respectively. Along with the contact angle evolutions, similar to the water-1-butanol mixtures, the finish points are situated at the maximal value of contact angle and the end of the increase stage for 25 wt.% and 50 wt.% concentrations. The droplets of water-ethanol mixture with high ethanol mass concentration behaved as those of water-1-butanol mixture, while with low ethanol mass concentration, the droplets' behaviors appeared similar to that of pure water. For the plot of $V^{2/3}$, 5 wt.% water-ethanol had the same linearity as pure water because of tiny ethanol concentration. For both 25% and 50% concentrations, the plot of $V^{2/3}$ has two different slopes: the first steep stage related to the quick evaporation of ethanol and the second more gentle stage. The steep stage extends with higher ethanol concentration. During the second stage, the plots of $V^{2/3}$ of all the water-ethanol mixtures have the similar regression coefficient and contact angles stay nearly constant in approximate value. According to Eq. 3.5 and 3.8, $\frac{2}{3}Kf(\theta)$ represents the regression coefficient of plot of $V^{2/3}$ and the same value indicates no change in density as well as component. Hence water mainly evaporates in the second stage.

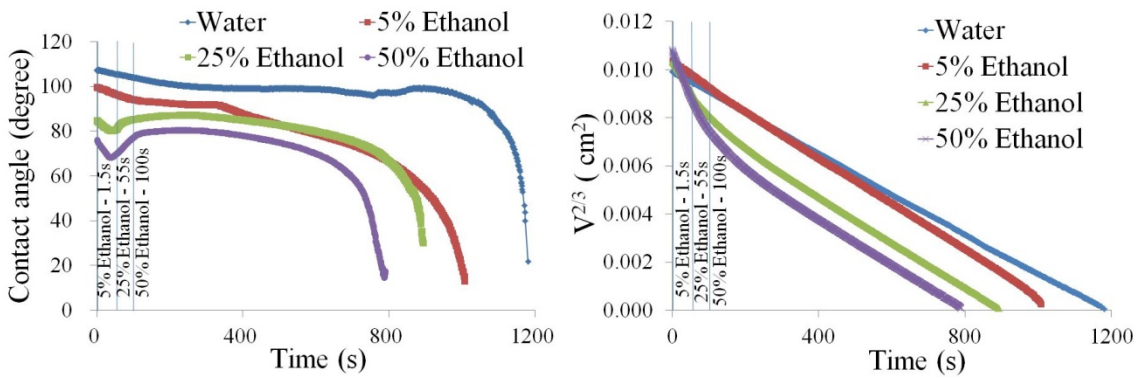

Figure 3.11 Evolution of contact angle and $V^{2/3}$ for droplets of pure water and droplets of 5%, 25% and 50% mass concentrations water-ethanol mixtures versus time.

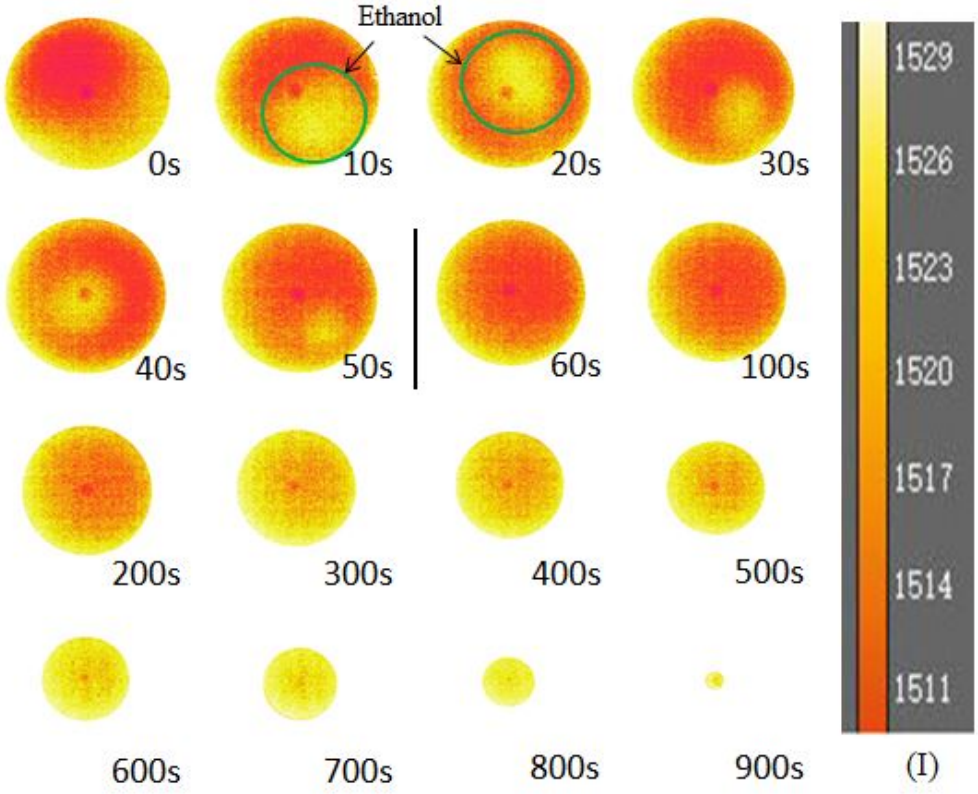

Figure 3.12 Snapshots from an infrared video of the evaporation process of a water-ethanol mixture droplet containing 25 wt.% ethanol at ambient temperature (See also the supplementary videos on line at Ref. [122]).

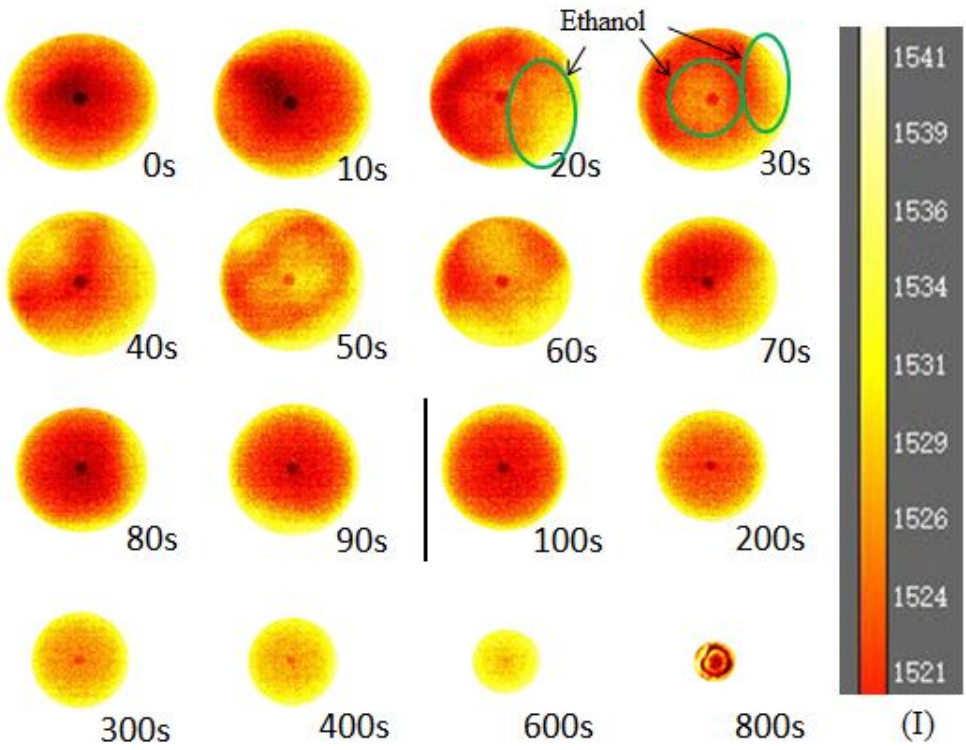

Figure 3.13 Snapshots from an infrared video of the evaporation process of a water-ethanol mixture droplet containing 50 wt.% ethanol at ambient temperature (See also the supplementary videos on line at Ref. [122]).

(b) Acoustic investigation

The ethanol concentration is monitored during the evaporation of a drop for each of the mass concentrations of ethanol of 5%, 25%, 50% and 100%. In the same manner as 1-butanol, the reflection coefficient is first measured during evaporation kinetics. From the calibration curve giving the reflection coefficient as a function of mass concentration of ethanol, shown in Fig. 3.14, the concentration evolution of alcohol is then transcribed as shown on Fig. 3.15. The results are the average of a series of three measurements.

Fig. 3.14 also reports the analytical evolution as a function of mass concentration of

ethanol obtained from Vatandas et al. [124]. There is a good agreement between the theoretical values and the measured ones within a confidence range of about 0.75%.

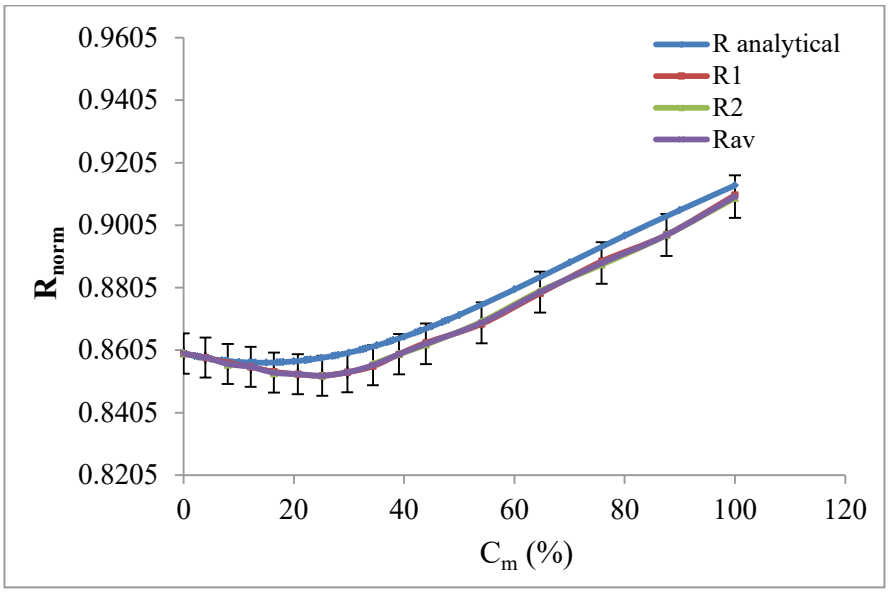

Figure 3.14 Calibration curve for ethanol at a temperature of 22°C and a hygrometry of 50%.

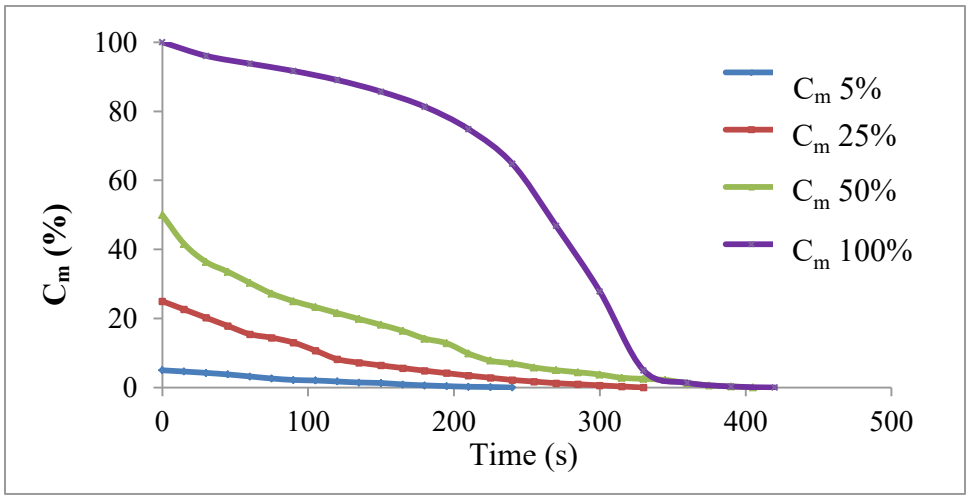

Figure 3.15 Mass concentration kinetics during evaporation of droplets of 5%, 25%, 50% and 100% of ethanol deduced from the measurement of the acoustic reflection coefficient at 22°C.

From Fig. 3.15, one can extract relevant parameters, such as the necessary time t_{C0} for the concentration to decrease to zero. The precision on t_{C0} is approximately 15 s. Tab. 3.2 summarizes the t_{C0} times for the different concentrations of ethanol and 1-butanol.

C_m (%)	t_{C0} (s) ethanol	t_{C0} 1-butanol
5	230 ± 15 s	220 ± 15 s
25	330 ± 15 s	
50	405 ± 15 s	
100	420 ± 15 s	

Table 3.2 t_{C0} for the different concentrations of ethanol and 1-butanol

3.4.4 Comparison between acoustics and infrared observations

Acoustics provides information on the manner by which alcohol is exhausted from the bottom of the drop, whereas infrared observation is related with the disappearance of alcohol from the surface of the drop. The necessary time for alcohol to exhaust from the bottom and from the surface of the drop is reported on Tab. 3.3.

	5 wt.% ethanol	25 wt.% ethanol	50 wt.% ethanol	5 wt.% 1-butanol
Visual method	1.5 s	55 s	100 s	264 s
Acoustic method	230 ± 15 s	330 ± 15 s	405 ± 15 s	220 ± 15 s

Table 3.3 Comparison between visual method and acoustic method

The times estimated by two methods are comparable in the case of the 1-butanol with a

mass concentration of 5%. However this is not the same consequence for any ethanol concentration. The possible explainable reason is the difference of volatility between ethanol and 1-butanol. At the beginning, the contact angle of water-ethanol mixture droplet decreased because of evaporation until the contact angle reached the receding angle of mixture solution. Then the contact line began to retract and the thermodynamic equilibrium of three interfaces was broken. Due to high volatility, ethanol evaporates faster than water which leads to the decrease of ethanol concentration on the air/liquid interface and the increase of surface tension of droplet from the beginning. Hence the contact angle increased since the disequilibrium of three interfaces. The ethanol concentration gradient was created between surface and interior of droplet which is the origin of convective flow. Therefore the ethanol evaporated on surface was replenished by convective flow, which generated the convection cells observed under infrared camera, and diffusion of ethanol molecules. When the total ethanol concentration became so weak as well as concentration gradient that the convective flow couldn't be engendered, the evaporation of ethanol on droplet's surface was controlled by its diffusion in droplet. It is because that the ethanol molecules need time to diffuse from the bottom to the surface of droplet and the diffusion coefficient of ethanol molecules in water (1.22×10^{-9} m^2/s) is much lower than in air (1.15×10^{-5} m^2/s). Thus, the ethanol/water ratio stayed in a very low value on the surface of droplet which couldn't be distinguished by infrared camera, and the contact angle stayed constant. The evaporation process is similar for the cases of 25 wt.% and 50 wt.% ethanol concentration, except for the case of 5 wt.% whose ethanol concentration on droplet surface is so tiny that it decreased quickly and the evaporation of ethanol was mostly controlled by diffusion in

droplet. However, during the evaporation controlled by diffusion in droplet, there was still a certain quantity of ethanol in droplet which could be detected by acoustic method. That's the reason for the large difference of exhaustion time of ethanol in droplet estimated between visual method and acoustic method. For the case of 5 wt.% water-1-butanol mixture, even the same concentration as 5 wt.% water-ethanol mixture, the droplet had the same evaporation process as that of 25 wt.% and 50 wt.% water-ethanol mixture. Owing to low evaporation rate of butanol, the decrease of 1-butanol/water ratio on droplet surface was much slower than that of water-ethanol mixture which can be demonstrated by the smooth increasing curvature of contact angle during the second stage. Thence, the concentration gradient remained much longer and the convective flows were generated continuously which was distinct under infrared camera. Even though the convective flows became weak, the supply of diffusion (0.93×10^{-9} m^2/s) in droplet maintained the 1-butanol/water ratio on surface at a certain value, which could be detected by infrared camera, due to low evaporation rate of 1-butanol. Consequently, the exhaustion times of 1-butanol in droplet estimated by both methods are close. Because the exhaustion of 1-butanol begins from the bottom of droplet on account of diffusion, the exhaustion time estimated by acoustic method is shorter than visual method. However, at the same concentration, the exhaustion times of alcohol estimated by acoustic method for water-ethanol and water-1-butanol mixture are very close which implies that the alcohol molecules diffusion is dominant during evaporation and with or without convection, there is no effect on the evaporation of alcohol in a mixture droplet.

3.5 Conclusions

For the first time, the acoustic method was applied for tracking the alcohol concentration in a bottom of a droplet of binary solution during evaporation. Using the pre-established acoustic reflection coefficient as a function of mass concentration, the alcohol concentration kinetics can be monitored versus time. From infrared images, the color distribution resulting from temperature and emissivity gradients is correlated to the existence of alcohol on the drop surface.

No ambient humidity influence is observed on the behavior of the contact angle and $V^{2/3}$ of a drop of pure 1-butanol during evaporation. In addition, the temperature at the surface remains constant and the acoustic reflection coefficient also remained constant during the process, i.e., no change of 1-butanol concentration occurred. These results confirm the very low hygroscopic power of a drop of 1-butanol during evaporation.

Due to the high hygroscopic nature of ethanol, the evaporation of a drop of pure ethanol is largely impacted by the relative humidity. Because of the absorption of water, the ethanol droplet became water-ethanol mixture and the convection cells appeared from the beginning. The kinetics of the acoustic reflection coefficient results in a decreasing trend of the ethanol concentration until reaching the acoustic reflection coefficient of water. These results showed that water vapor coming from ambient humidity condensed onto the droplets of pure ethanol during evaporation and the solution becomes a mixture of water and ethanol. As a consequence of high volatility, firstly the ethanol evaporated and exhausted, and then the absorbed water continued to evaporate through the end.

The exhaustion time of ethanol in drop estimated by acoustic method is always much

shorter than visual method at three different ethanol concentration. However, for the case of water-butanol mixture, both methods have the same result. This can be probably explained by the difference water/alcohol ration on drop surface due to different volatility between ethanol and butanol.

Chapter 4 Effect of Marangoni Flow on Evaporation Performance of Binary Sessile Droplets

This chapter is based on the published work in The Journal of Physical Chemistry B in 2017 [125]. The author of this thesis contributed to the designing and performing experiments, analyzing experimental results and writing manuscript. J. Schiffler co-designed this experiment and took in charge of experimental devices examination. S. Ouenzerfi measured the surface tension of 1-butanol-water binary solution with different alcohol concentration as a function of temperature. Prof. S. Harmand supported the author of this thesis for the writing of the manuscript and gave approval to the final version.

4.1 Abstract

The evaporation processes of pure water, pure 1-butanol, and 5% 1-butanol aqueous solution drops on heated hydrophobic substrates are investigated to determine the effect of temperature on the drop evaporation behavior. The evolution of the parameters (contact angle, diameter, and volume) during evaporation measured using a drop shape analyzer and the infrared thermal mapping of the drop surface recorded by an infrared camera were used in investigating the evaporation process. The pure 1-butanol drop does not show any thermal instability at different substrate temperatures, while the convection

cells created by the thermal Marangoni effect appear on the surface of the pure water drop from 50°C. Because 1-butanol and water have different surface tensions, the infrared video of the 5% 1-butanol aqueous solution drop shows that the convection cells are generated by the solutal Marangoni effect at any substrate temperature. Furthermore, when the substrate temperature exceeds 50°C, co-existence of the thermal and solutal Marangoni flows is observed. By analyzing the relation between the ratio of the evaporation rate of pure water and 1-butanol aqueous solution drops and the Marangoni number, a series of empirical equations for predicting the evaporation rates of pure water and 1-butanol aqueous solution drops at the initial time as well as the equations for the evaporation rate of 1-butanol aqueous solution drop before the depletion of alcohol are derived. The results of these equations correspond fairly well to the experimental data.

4.2 Introduction

As a natural phenomenon, drop evaporation has become an important topic in recent decades, attracting interest in many scientific applications such as coatings [126], ink printing [107,127], and cooling systems [113]. Numerous experimental [97,98,124, 128,129], analytical [98,104,105,130], and numerical [131-133] methods have been employed to investigate the evaporation process of sessile drops at ambient conditions, the behavior of which can be classified in three regimes: constant contact angle regime, constant contact radius regime, and a combination of both regimes.

Picknett and Bexon [101] studied an evaporating drop of methyl acetoacetate on a nearly flat surface covered by a layer of PTFE (polytetrafluoroethylene). The droplet evaporation was conducted at ambient temperature and its change of mass was recorded

by a microbalance. Based on Maxwell's analogy between diffusive flux and electrostatic potential, they obtained the evaporation rate equation for constant contact angle regime and constant contact radius regime. The comparison of droplet half-life by theoretical prediction with the experimental data showed a satisfactory agreement in both modes of evaporation at a particular range of contact angle, drop size, and vapor pressure. Rowan et al. [134] measured the change of contact angle and height of small water drops on poly-(methyl methacrylate) (PMMA) in constant contact radius regime. Based on a spherical cap geometry model, they derived a drop mass loss equation that included the liquid-vapor interface diffusion effect. The prediction result of their equation was validated by experimental data for a contact angle below 90°. Shanahan and Bourges-Monnier [135,136] conducted a series of experiments with sessile water and n-decane drops deposited on three different polymer substrates (polyethylene, epoxy resin, and Teflon) with and without saturated vapor pressure condition. The measurements of contact angle, contact diameter, and height of drops versus time revealed that the evaporation process could be divided in three or four distinct stages in open air, which depends on the roughness of the substrate. By analyzing the second stage, which is in constant contact radius regime, they proposed a model to evaluate the diffusion coefficient of liquid vapor into the air with the radial diffusion assumption. Hu and Larson [137] used experimental, analytical, and computational techniques to investigate the evaporation process of a sessile water drop in constant contact radius regime at ambient atmosphere. The quasi-steady water vapor concentration distribution and evaporation flux above the drop were calculated by a finite element method (FEM). Both experimental and computational results disclosed a time-independent constant

evaporation rate when the initial contact angle was less than 40°, despite an extraordinarily high evaporation flux at the periphery of the drop. An approximate model for evaporation rate at ambient condition was developed by comparing the FEM and analytical solution results, which agreed fairly well with the experimental data in the literature.

When the environmental condition is not ambient, the evaporation process of sessile drops will become more complicated with additional interfering factors such as temperature, humidity, vapor pressure, and convection in the drop or in the air. Girard et al. [138] used an infrared camera to investigate the water deposited on heated copper substrates at different temperatures and determined the contact line using the maximum value in the temperature profile. The infrared method result showed a satisfactory quantitative and qualitative agreement with the measurements using the optical technique. Furthermore, they used local energy conservation laws associated with the local measurements of the interface temperature to deduce the equation of local evaporative mass flux. The calculated evaporative flux was represented in a 3D plot with time. The mass flux increased as time proceeded and when approaching the contact line, the evaporation rate increased abruptly and tended to approach infinity. Their result was in agreement with the theories proposed for the evaporation of menisci; however, they did not present any experimental result on the evaporation rate. P.L. Kelly-Zion et al. [97] investigated the evaporation of droplets of four hydrocarbon components (3-methylpentane, hexane, cyclohexane, and heptane) with different base areas at atmospheric condition on aluminum and used an analytical balance to measure the reduction of the droplet mass. They first calculated the evaporation rate by Stefan's

equation, which is based on diffusion-controlled mode. They found that the diffusion-controlled mode underestimates the evaporation rate and even the measured rate is 475% greater than the value from the diffusion-controlled mode with a large drop radius. They developed an empirical model combined with convective transport, which is estimated by correlation with the Grashof number. This combined transport model agrees well with the measured evaporation rates and the error is less than 8%. Tuan A.H. Nguyen et al. [98] performed a theoretical analysis in order to determine the volume change of a sessile droplet due to natural evaporation and validate the volume change with the change in the transient contact angle and base radius as measured by tensiometry. In that study, they investigated two-stage evaporation: first at constant contact radius regime, then at constant contact angle regime. Based on Fick's second law, which describes the mass conservation for the vapor evaporation by diffusion, the Laplace partial differential equation of second order can be conveniently solved for the vapor concentration in the toroidal coordinate. By applying the separation-of-variables method and the Mehler–Fock integral transform, they obtained the solution for the vapor concentration around the droplet and then the net of the surface diffusive flux. Finally, they obtained the total evaporation rate by integrating the diffusive flux for the constant contact angle regime. They found that the total evaporation rate was a negative and monotonically decreasing function of the contact angle, only if the contact angle and wetted base radius were sufficiently small, and the residual droplet volume linearly decreased during the first stage. Carle et al. [99] investigated ethanol droplets that evaporated in air at a temperature of 25 °C on a cylindrical heated aluminum substrate. A heat flux meter was attached to the substrate in order to determine the evaporation rate. Two sets of experiments were

conducted with similar setups under terrestrial ($1g$) and reduced gravity (μg) conditions (performed with parabolic flights) to validate the effect of the buoyant natural convection transport on the vapor phase in the evaporation process. Under terrestrial gravity conditions, the diffusive model value was close to the experimental value, but as the substrate was heated, the diffusive model underpredicts the evaporation rate and the deviation increased with the substrate temperature. However, under reduced gravity conditions, the diffusion-controlled evaporation model correctly predicted the experimental data. They supposed that the natural convection in the vapor phase enhanced the evaporation rate and derived an expression for the evaporation rate that took into account the diffusive and naturally convective vapor transport. By applying this model, a satisfactory estimation of the experiments was obtained when the substrate was heated: the deviation was less than 7%. However, at ambient temperature, this model overestimated the evaporation rate by 20%.

The purpose of this study is to investigate the effect of the substrate temperature on the evaporation of pure solution and binary mixture drops and also to compare the evaporation behavior between these two types of drops. When a pure solution drop is deposited on a heated substrate, the temperature at the bottom of the drop is close to that of the substrate while the temperature at the top of the drop is similar to the ambient temperature. When the temperature difference as well as the surface tension difference between the top and the periphery of the drop becomes suitably large, the liquid will flow from the low surface tension place to the high surface tension place on the drop surface. This is called the thermal Marangoni flow. The surface tension difference can be also created by non-uniformity in composition and the generated flow in this case is termed as

the solutal Marangoni flow. The effect of surface tension gradient-driven flow is the Marangoni effect, named after the Italian physicist Carlo Marangoni, who found this phenomenon when studying the spreading of oil on water surface [14]. Therefore, another objective of this study is to determine the relation between the substrate temperature and the Marangoni effect as well as their influence on the evaporation rate.

4.3 Experimental Setup

The substrates are placed in a vapor chamber (14 cm × 12.4 cm × 7.5 cm), in which the ambient temperature and relative humidity can be controlled (Fig. 4.1) without air current. At the top of the vapor chamber, there are a sapphire window for the infrared camera and a hole for passing the syringe. The drops are deposited on the hydrophobic silicon substrate, below which a heater connected to an electrical controller is attached. The infrared camera (FLIR X6580SC, 640 × 512 pixels, 200Hz, 15 μm detector pitch) is installed on top for infrared thermal mapping and visualization of thermal instabilities on the surface of the droplets. The use of dynamic infrared videos provides a good visualization of the convection cell motion on the droplet surface and consequently the alcohol life time during evaporation, as water and alcohol have different emissivities. A side view CCD (charge-coupled device) camera (Allied Vision Technologies, 15 fps, 780 × 580 pixels) is used to record the evaporation process of the droplets for profile analysis by using a Kruss® drop shape analyzer (DSA) to measure the contact angle, volume, diameter, and height of the sessile droplets during evaporation.

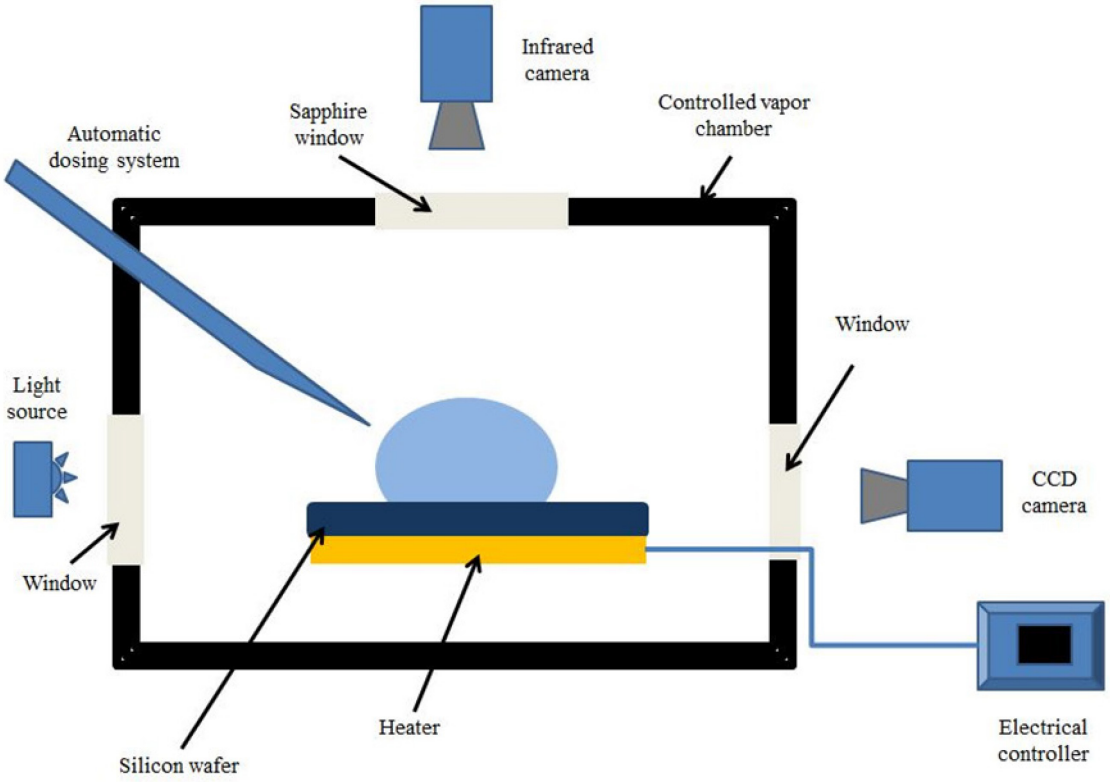

Figure 4.1 Schematic of the experimental setup of modified Kruss® drop shape analyzer and infrared camera.

4.4 Experimental Results and Discussion

In this study, the evaporation of three different drops, namely pure water, pure 1-butanol, and 5% 1-butanol aqueous solution on hydrophobic silicone substrates was investigated. The addition of 1-butanol is for verifying the enhancement of evaporation by the solutal Marangoni flow. Water is one of the common working fluids applied in heat pipes and 1-butanol aqueous solution is a novel one for wickless heat pipes. The experiments were conducted in six different substrate temperatures from T_s = 22 to 80°C to investigate the influence of temperature. In addition, the ambient temperature in the vapor chamber was

stabilized at T_a = 22 °C, and the relative humidity was maintained at 50% throughout the experiments.

Using the Kruss® DSA, the parameters of the drops (contact angle, diameter, and height) were measured as a function of time by analyzing the videos recorded by the side-view CCD camera. The measurement of contact angle is based on Young's Equation and the contact angle of the sessile drop is measured at the three-phase contact point between the drop contour (liquid/vapor interface) and the projection of the surface (solid/liquid interface). Based on these measurements, the volume of drop versus time was calculated by software in computer. The diameter of tested drop is always smaller than the capillary length (2.7 mm at standard temperature and pressure), so the profile of drop can be considered as a spherical cap. Fig. 4.2 shows the measurements of contact angle and diameter for water and 5% 1-butanol aqueous solution drops at six different substrate temperatures T_s.

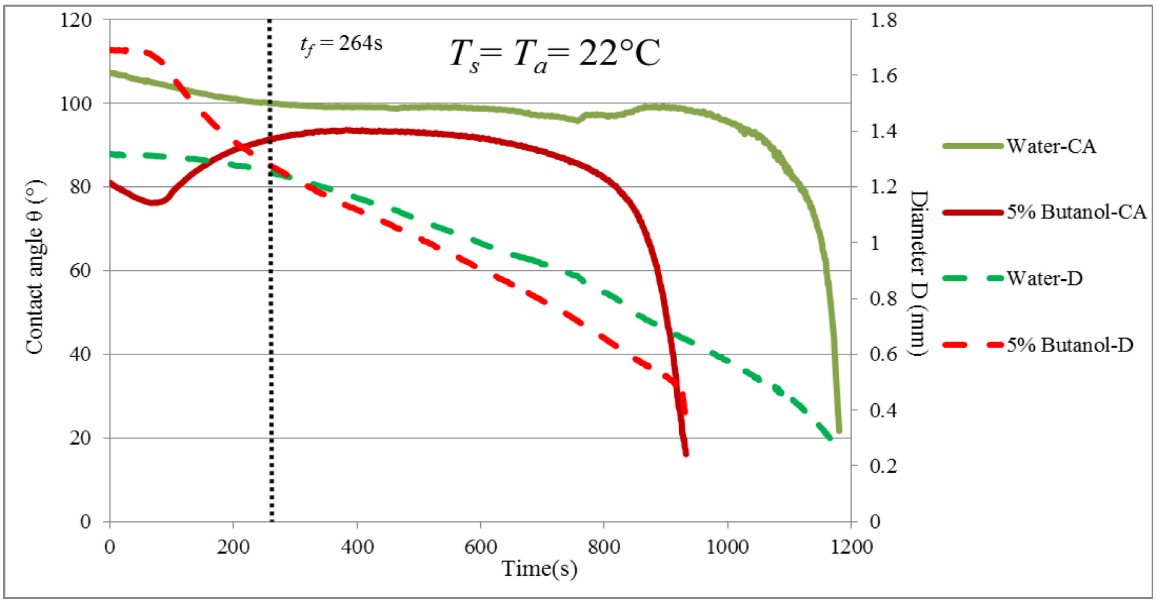

(a) T_s = 22°C

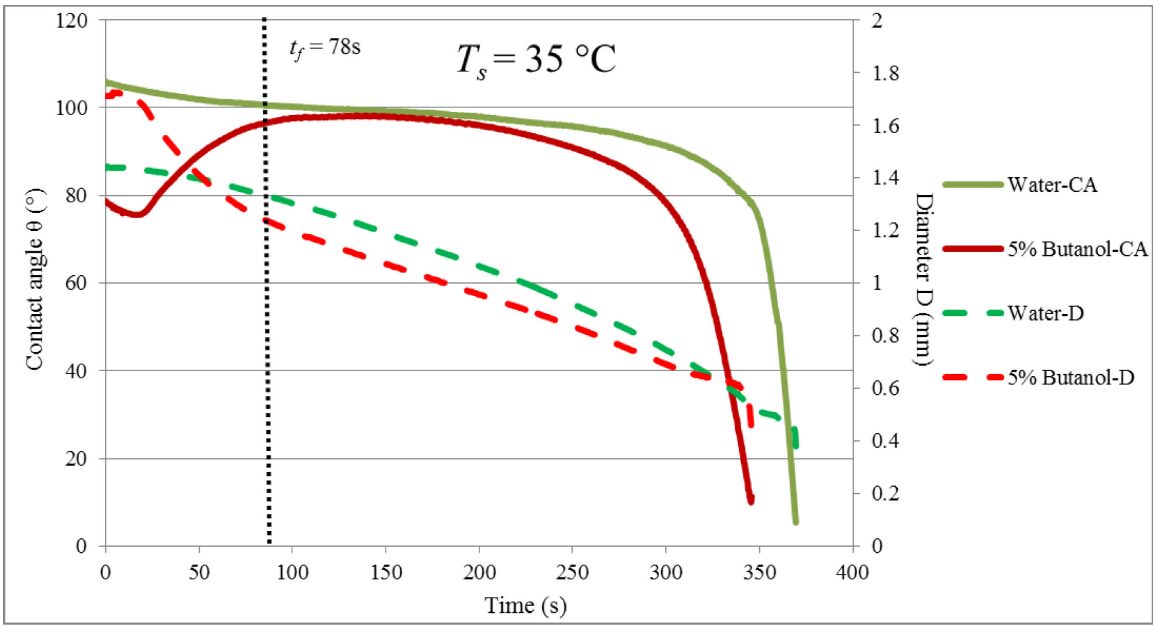

(b) T_s = 35°C

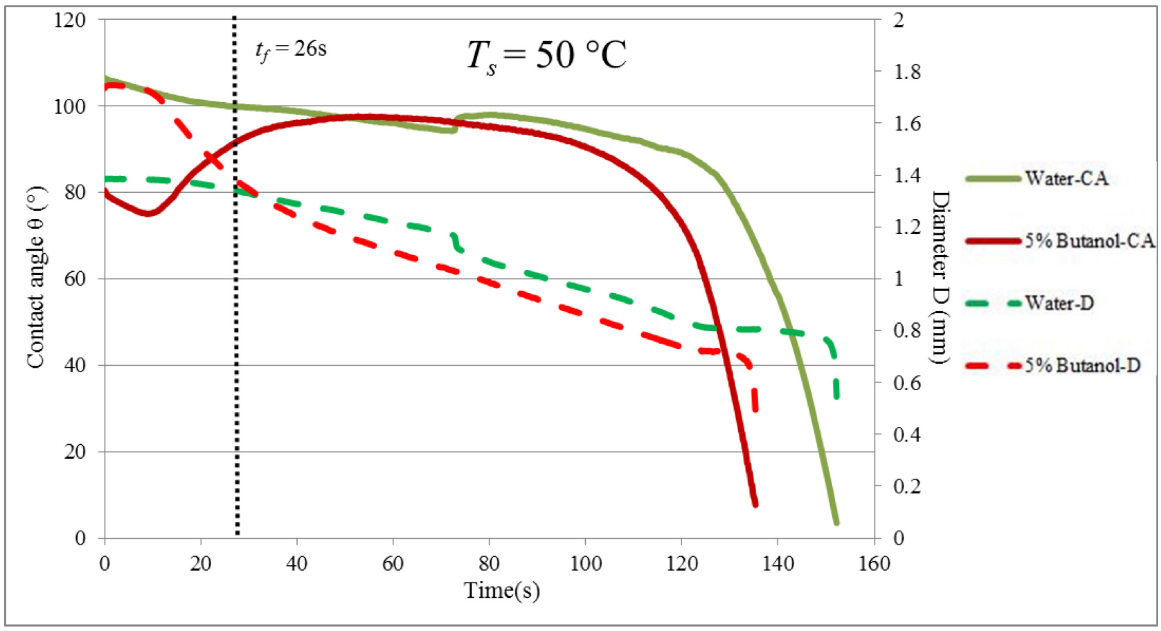

(c) T_s = 50°C

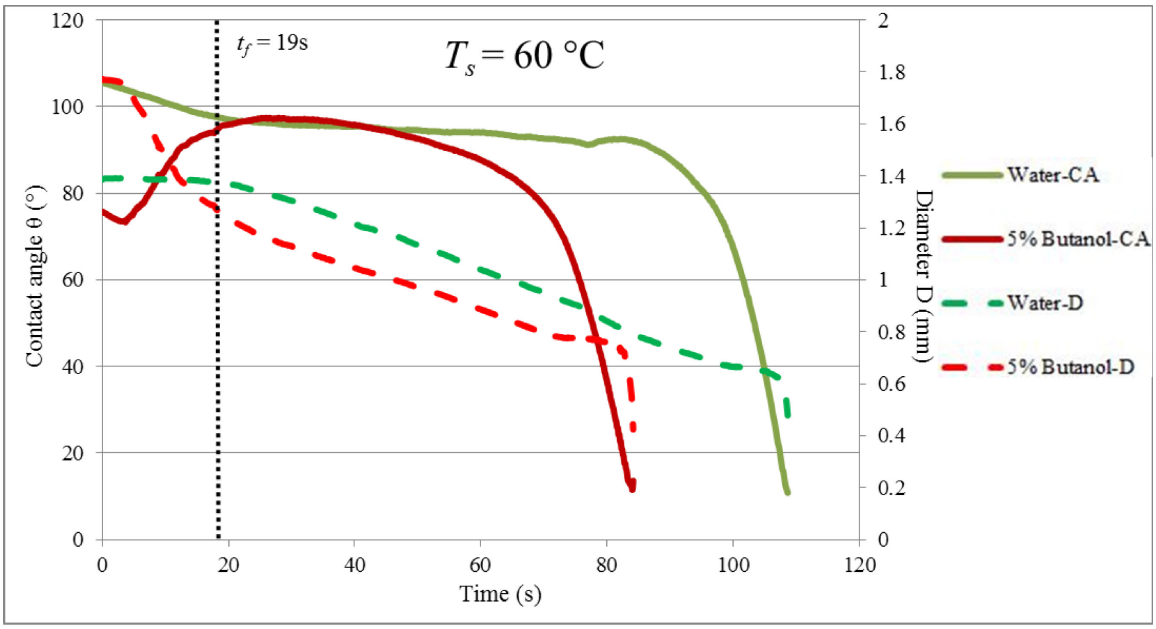

(d) T_s = 60°C

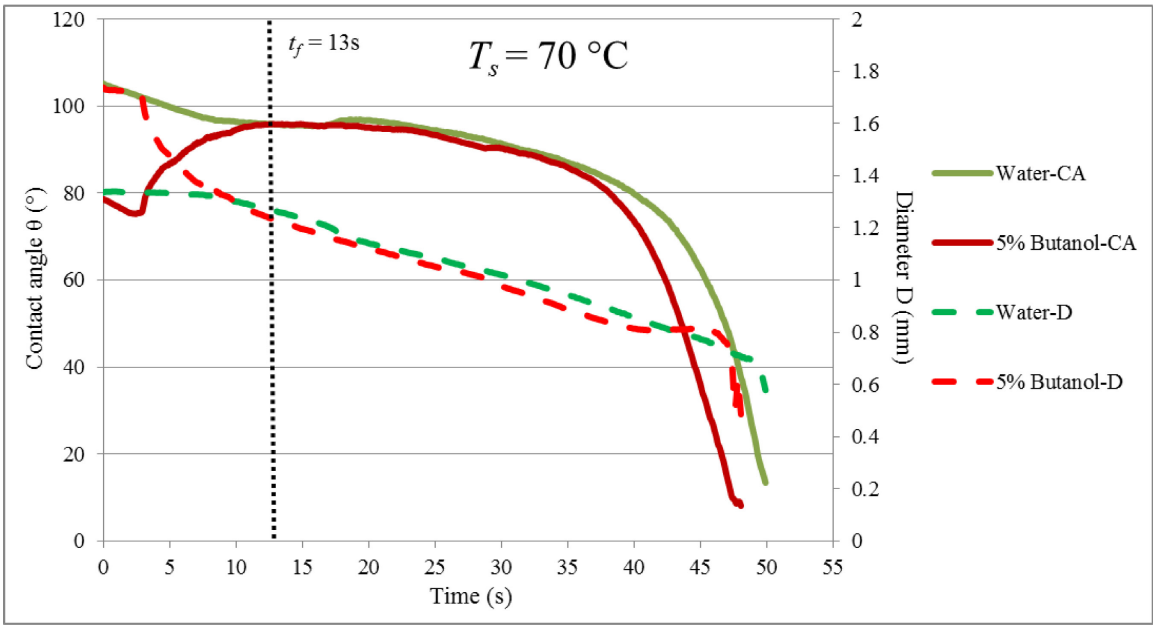

(e) T_s = 70°C

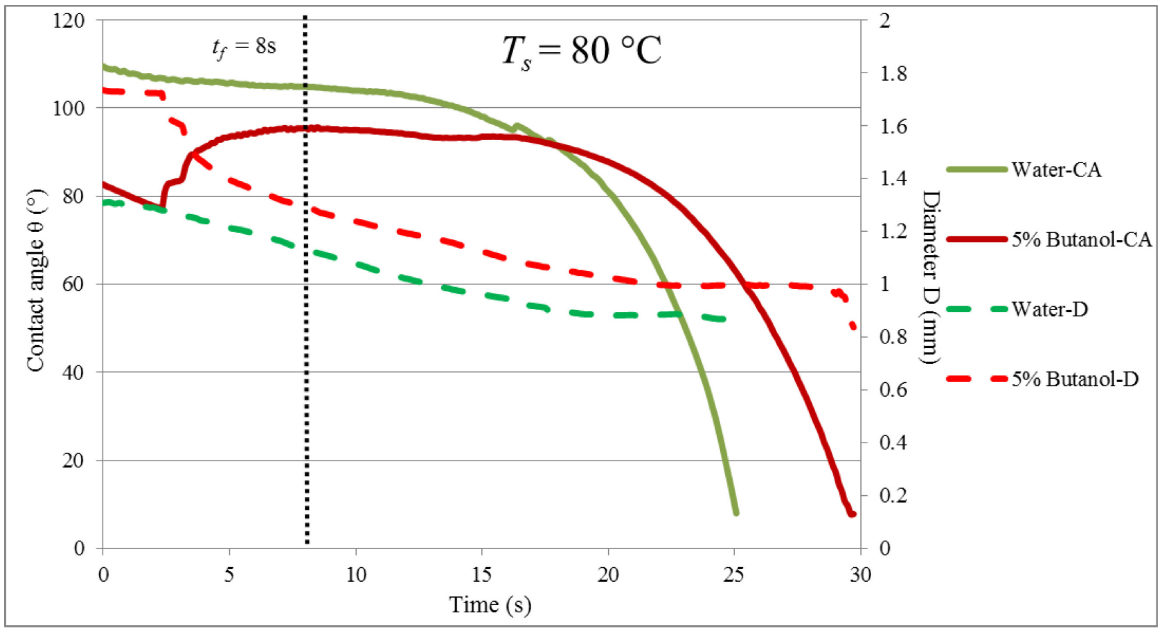

(f) T_s = 80°C

Figure 4.2 Evolution of contact angle and diameter for pure water and 5% 1-butanol aqueous solution drops versus time at substrate temperatures T_s = 22°C, 35°C, 50°C, 60°C, 70°C, and 80°C.

The substrate temperature has no obvious effect on the overall evolution of the contact angle and diameter versus time for both liquids. For the pure water drop, the contact angle stays almost constant or decreases at a slow rate during the most part of evaporation and diminishes sharply at the end. However, the drop of 1-butanol aqueous solution possesses a different behavior with respect to the contact angle and diameter in the course of evaporation. The evolution of contact angle can be divided into four stages. First, the contact angle decreases, and then increases until the maximum value, which is very close to that of the water drop. Afterward, the contact angle decreases slowly and diminishes abruptly at the end of evaporation, which is similar to that of pure water.

Owing to its lower density, 1-butanol tends to accumulate at the liquid/air interface after deposition of the drop. Thus, the diffusion of vicinal 1-butanol molecule to liquid/air interface leads to an increase in the ratio of 1-butanol/water, which is the reason why the contact angle decreases at the beginning of evaporation of the 1-butanol aqueous solution drop. Then, the evaporation rate of the liquid depends on the difference of its vapor concentration at the liquid/air interface and in ambient environment at infinite distance. However, in this experiment, the 1-butanol vapor concentration in the air is zero while the relative humidity of water vapor is 50%. That is why 1-butanol evaporates faster than water. Consequently, at the second stage, the ratio of 1-butanol/water at the liquid/air interface starts to decrease and the contact angle begins to increase accordingly. At the last two stages, the 1-butanol in the drop is almost depleted because of preferential evaporation and then the drops of both liquids have the same behavior in regard to the contact angle.

Regarding the temperature profile on the drop surface, the lowest temperature is found at the top and the highest temperature is situated at the contact line. The temperature difference between the top and the contact line is the source of the thermal Marangoni flow. In Fig. 4.3, no thermal instability can be detected during evaporation of the 1-butanol drops at different substrate temperatures. However, at higher substrate temperatures, a ring-like thermal pattern appears near the contact line and becomes more evident with the increase of substrate temperature. Fig. 4.4 shows the snapshots of infrared videos of water drop when they are deposited on the substrate. From the substrate temperature T_s = 50°C, the convection cells created by the thermal Marangoni flow are obvious under the infrared camera and become clearer and more intense with the

increase of substrate temperature. However, for the drop of 1-butanol aqueous solution, both thermal and solutal Marangoni effects work together. The former is caused by the temperature difference, while the latter is by the 1-butanol concentration difference. Based on the infrared videos (Fig. 4.5), the convection cells have two different patterns: first, the convection cells are irregular, chaotic, and cover the total surface of the drop; then, these small cells disappear gradually and two big ones appear which are similar to those observed for the water drop at higher substrate temperatures. At the end of evaporation, both convection cells disappear and the temperature is almost homogenous on the drop surface. By comparing the infrared images of the evaporation process between pure water (Fig. 4.6) and 1-butanol aqueous solution drops (Fig. 4.5) at the same conditions, the small random convection cells can be deduced to be generated by the solutal Marangoni effect, while the big stable ones are formed by the thermal Marangoni effect. The disappearance of the small convection cells means that there is no large alcohol concentration difference on the drop surface. Thus, the moment when the small convection cells disappear can be determined as the moment t_f when 1-butanol is nearly depleted in the drop, which is marked in Fig. 4.2. As shown in this figure, at t_f, the contact angle of 1-butanol aqueous solution drop is close to the maximum value, which signifies that the ratio of 1-butanol/water at the liquid/air interface is very low and can be assumed as zero. This confirms the determination of t_f. Furthermore, the accuracy of t_f determination by visual observation was already confirmed in our former research by the acoustic method [93].

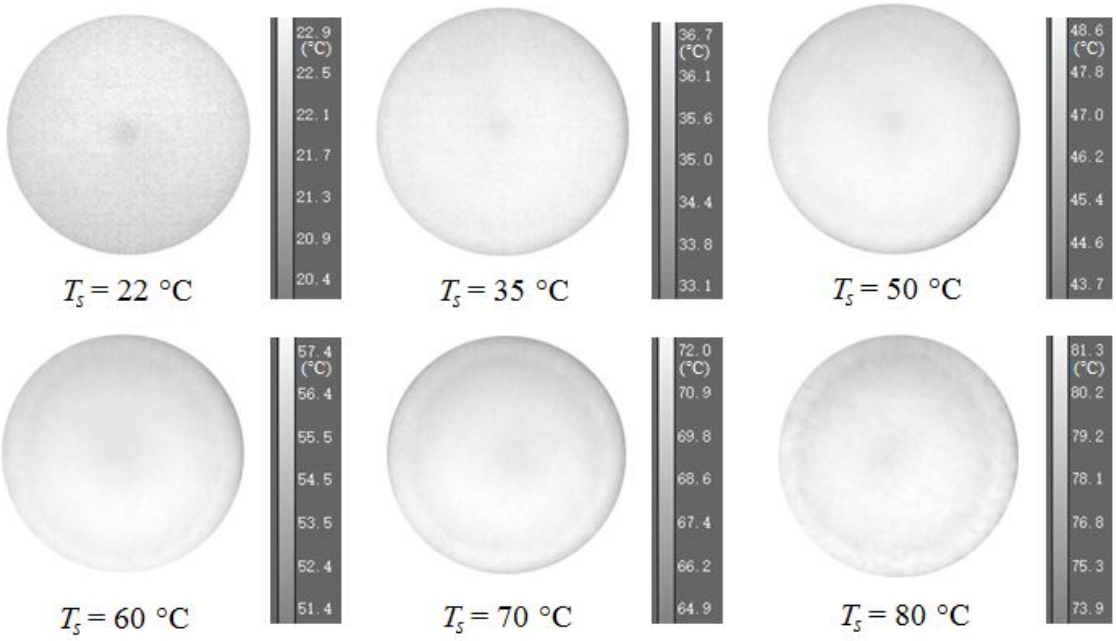

Figure 4.3 Snapshots from infrared videos of the evaporation process of 1-butanol drops at 50% relative humidity and different substrate temperatures T_s.

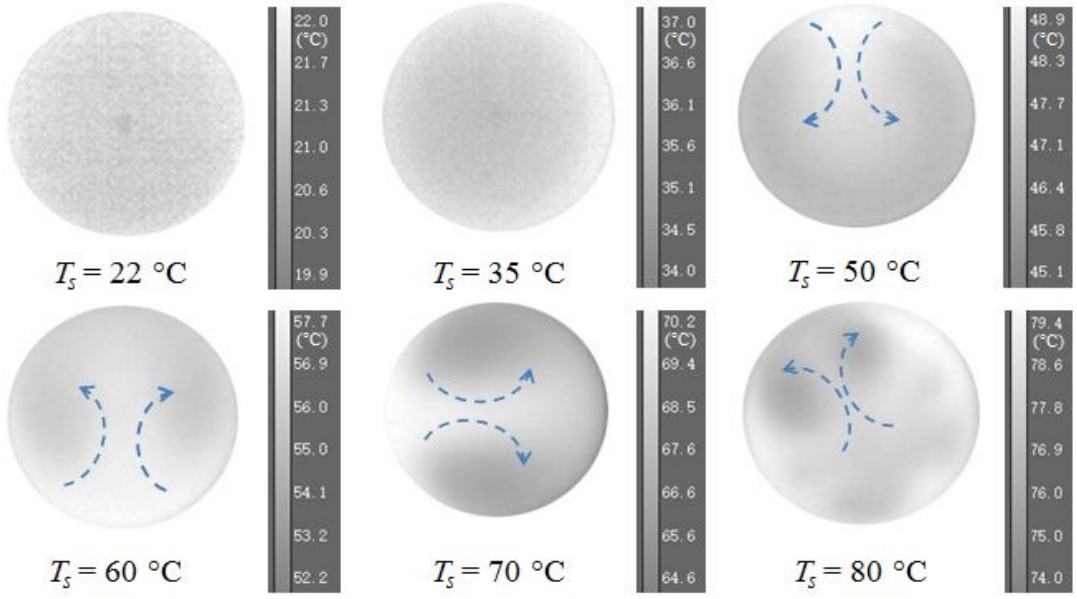

Figure 4.4 Snapshots from infrared videos of the evaporation process of water drops at 50% relative humidity and different substrate temperatures T_s.

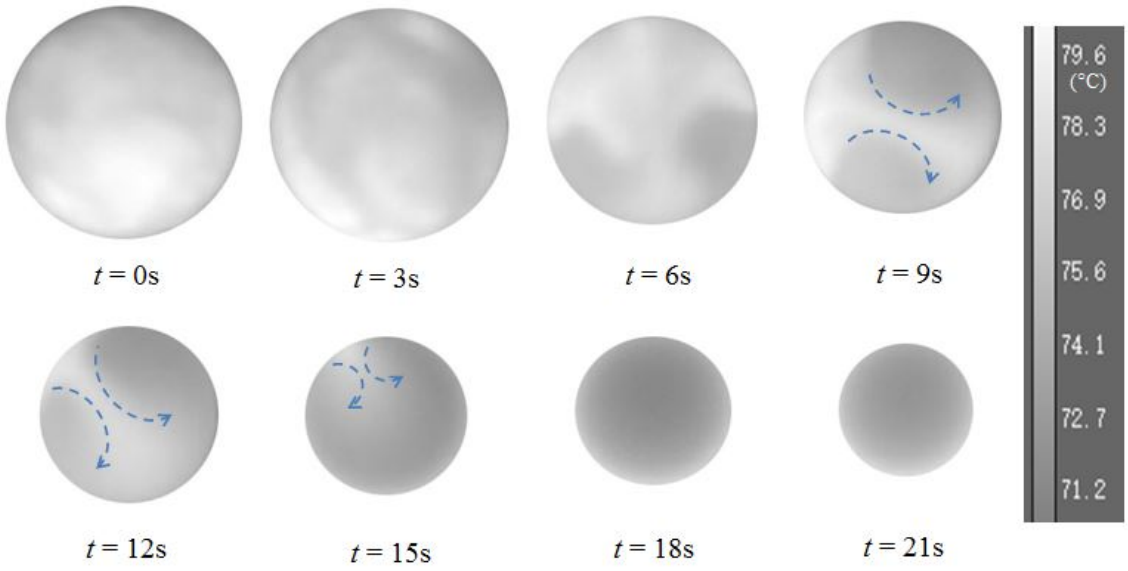

Figure 4.5 Snapshots of different moments from infrared videos of the evaporation process of 5% 1-butanol aqueous solution drop at 50% relative humidity and T_s = 80°C substrate temperature.

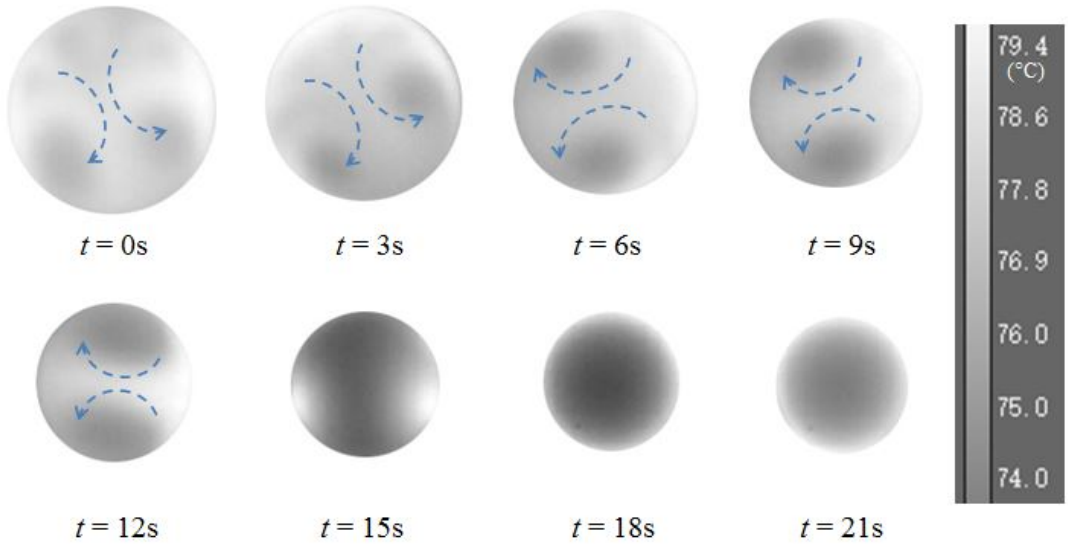

Figure 4.6 Snapshots of different moments from infrared videos of the evaporation process of a water drop at 50% relative humidity and T_s = 80°C substrate temperature.

According to the study conducted by Vochten and Petre [21], the 1-butanol aqueous solution is one type of self-rewetting fluid, which has a surface tension that decreases in a specific range of temperature. The surface tension of 1-butanol aqueous solution was measured at different temperatures by the pendant drop method with Kruss® DSA. Fig. 4.7(a) shows the relation between the temperature and surface tension σ or convection cells duration t_c of 5% 1-butanol aqueous solution drop, respectively. As a self-rewetting fluid, the mixture drop surface tension decreases from 20°C to 50°C approximately, where 50°C is the specific critical temperature for 5% 1-butanol aqueous solution. Beyond this value, the surface tension increases with an increase of temperature as a common liquid. The duration of convection cells declines with the increase of temperature because of the reduction of total evaporation time. Beyond the specific critical temperature, the decrease of convection cells duration becomes more moderate. Fig. 4.7(b) represents the relation between the ratio of 1-butanol duration on total evaporation time and temperature. The ratio has the minimal value at 50°C which coincides with the specific critical temperature of surface tension for 5% 1-butanol aqueous solution.

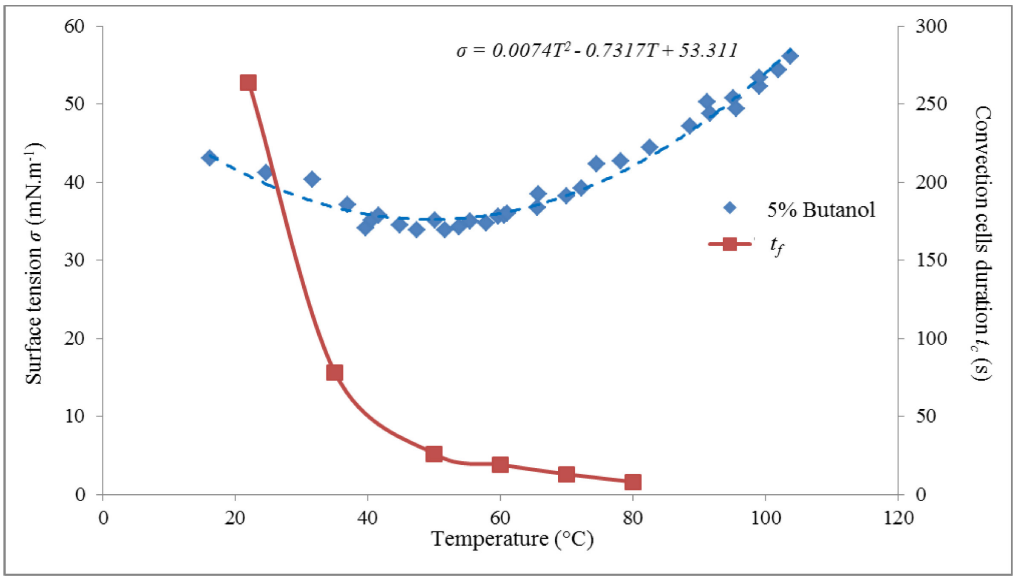

(a)

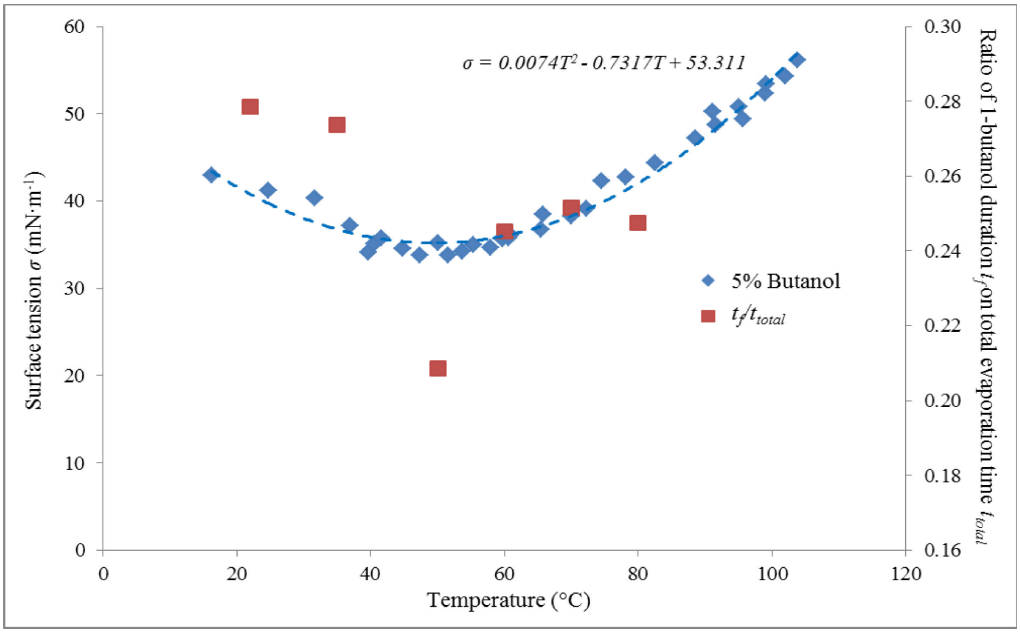

(b)

Figure 4.7 (a) Surface tension and convection cells duration of 5% 1-butanol aqueous solution drop as a function of temperature. (b) Surface tension and ratio of 1-butanol duration on total evaporation time versus temperature.

Hu and Larson derived an approximate equation for predicting the evaporation rate of water drop at ambient condition [137]:

$$\dot{V}(t) = -\frac{\pi R D_a}{\rho}(1-H)C_V(0.27\theta^2 + 1.30) \tag{4.1}$$

where R is the contact line radius, θ is the contact angle, D_a is the diffusion coefficient in air, H is the relative humidity, C_V is the saturated vapor concentration, and ρ is the density.

The result of applying Hu and Larson's equation to the ambient case is shown in Fig. 4.8. The prediction agrees very well with the experimental data of the water drop. In the same figure, the experimental data of 1-butanol aqueous solution drop is added for comparison and the alcohol exhaustion time t_f is marked. With the addition of 1-butanol, the solutal Marangoni flow created by the concentration difference clearly enhances the instantaneous evaporation rate of the drop at the beginning. At t_f, the evaporation rate of the mixture drop is similar to that of the water drop when 1-butanol is depleted. Because these experiments are conducted at the same conditions, the enhancement of the evaporation rate is clearly due to the solutal Marangoni effect. However, when applying Hu and Larson's equation to the cases when the substrate is heated, the equation always underpredicts the instantaneous evaporation rate compared with the experimental data. The convection generated by the thermal Marangoni effect, which will enhance the evaporation, is supposed to be the main reason.

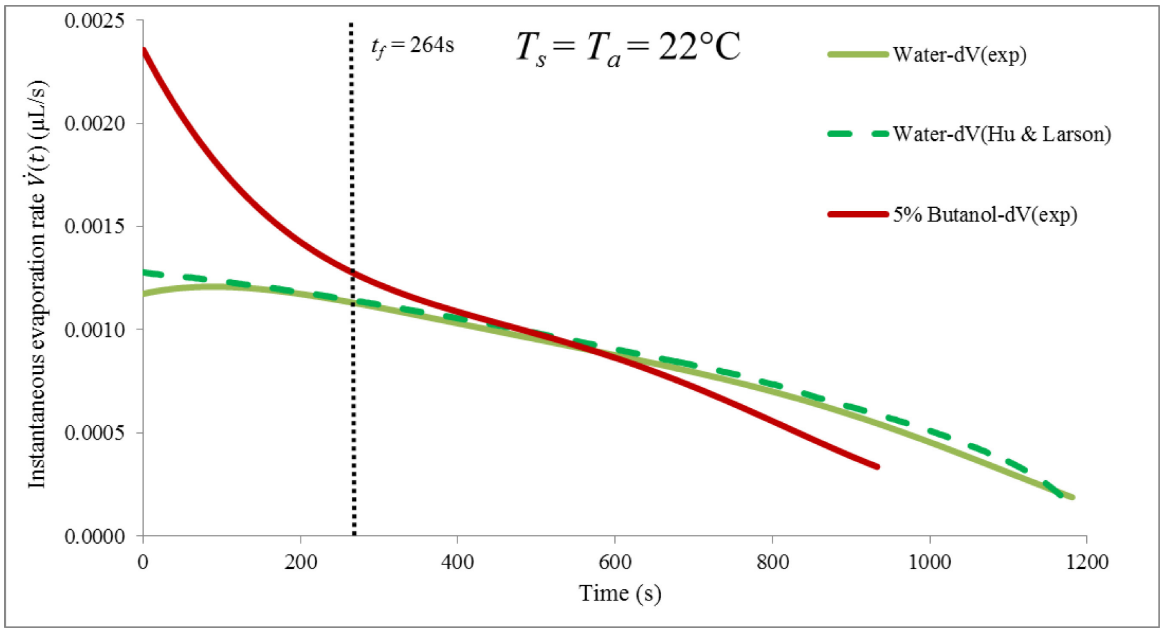

Figure 4.8 Instantaneous evaporation rate $\dot{V}(t)$ of water and 5% 1-butanol aqueous solution drops and prediction by Hu and Larson's equation versus time at T_a = 22°C and 50% relative humidity.

Based on the analysis mentioned previously, after the exhaustion time t_f, the 1-butanol is practically depleted in the mixture drop and a similar behavior as the water drop can be observed. Hence, the evaporation enhancement by addition of 1-butanol is only effective before t_f. Fig. 4.9 shows the comparison of the evaporation rate until exhaustion time between the water and 1-butanol aqueous solution drops. With the solutal Marangoni effect, the mixture drop possesses a higher evaporation rate than the water drop from ambient temperature and this enhancement increases with increasing substrate temperature. However, at T_s = 80°C, the gap becomes unexpectedly very slight and both drops have similar evaporation performance. The blue dashed line represents the prediction of evaporation rate by Hu and Larson's model. Except for the ambient case, the Hu and Larson's model always underpredicts the evaporation rate until t_f of the water

drop and this disparity increases with substrate temperature. To examine the influence of the initial concentration of 1-butanol on the evaporation dynamics, we compared the evaporation rate at the initial time between water and 1-butanol aqueous solution drops as shown in Fig. 4.10. The initial evaporation rate of both liquids shows an exponential growth with the increase of substrate temperature. With the solutal Marangoni effect, the mixture drop possesses much higher evaporation rate than the water drop at the initial moment when the 1-butanol concentration is maximum in mixture drop. Even at T_s = 80 °C, the mixture drop evaporates faster than the water drop at the beginning, though they have similar evaporation rate until t_f. The probable reason is that at the initial time, the 1-butanol concentration, which has a higher evaporation rate than water, is at the peak as well as the solutal Marangoni effect. And then the solutal Marangoni effect is reduced with the decrease of the 1-butanol concentration difference in the drop.

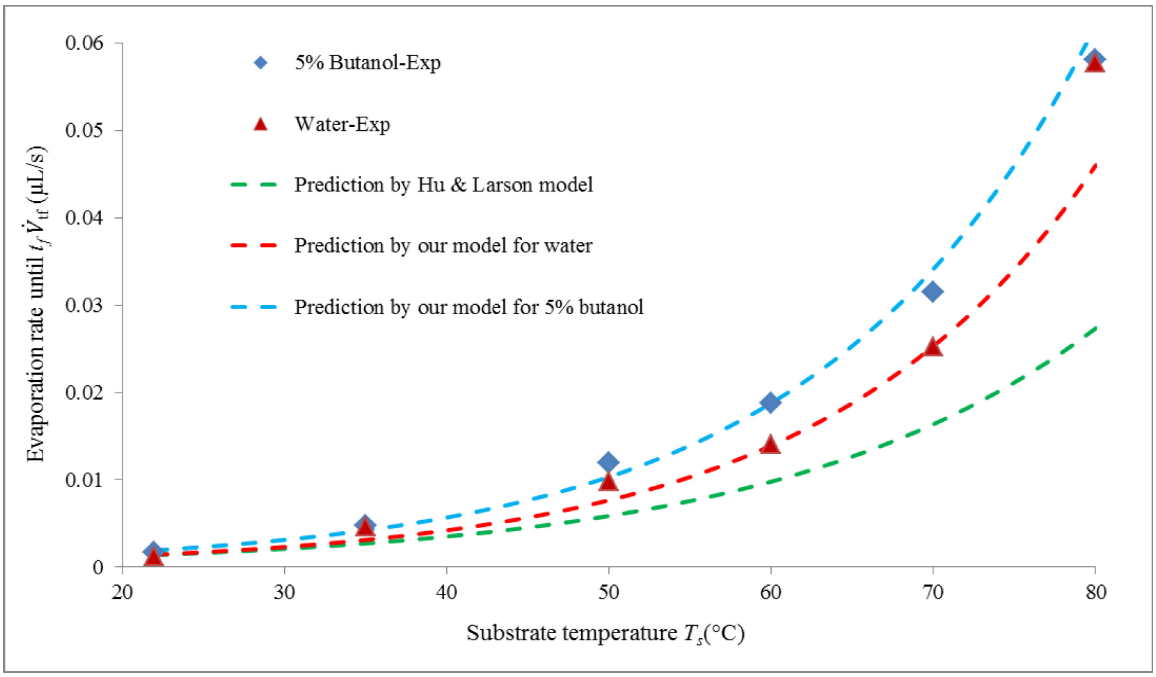

Figure 4.9 Evaporation rate until alcohol exhaustion time t_f of water and 5% 1-butanol aqueous solution drops and prediction by Hu and Larson's model and the model developed in this study as a function of substrate temperature T_s.

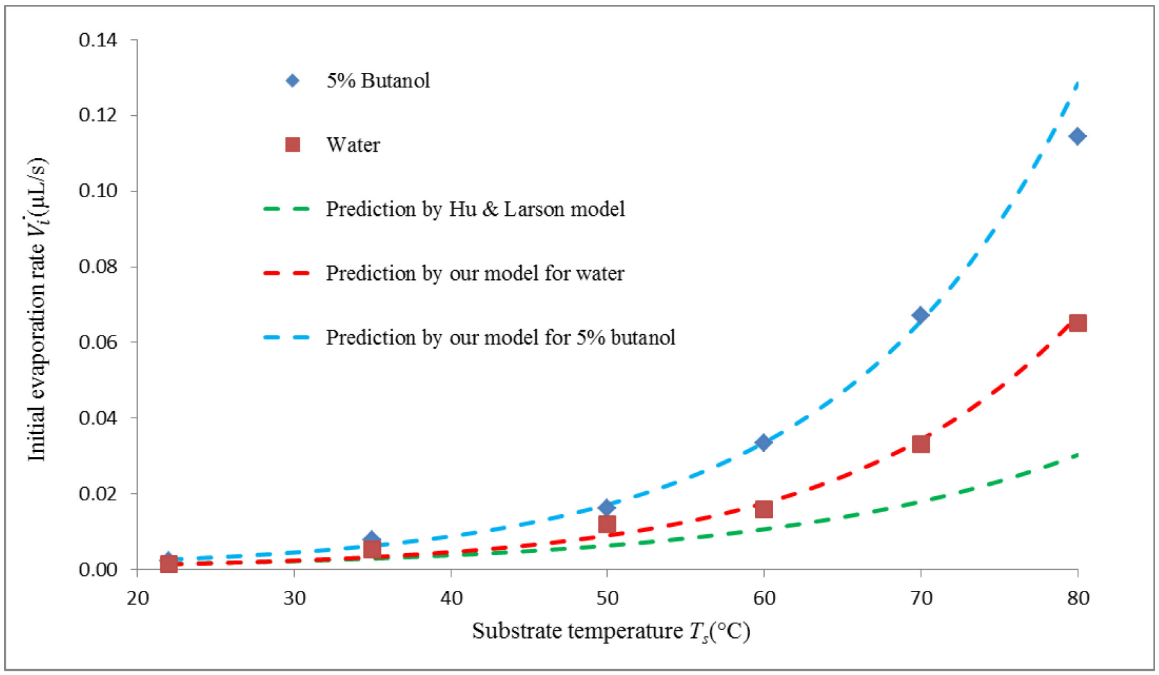

Figure 4.10 Initial evaporation rate of water and 5% 1-butanol aqueous solution drops and percentage of initial evaporation rate enhancement by addition of 1-butanol as a function of time.

The Marangoni effect is characterized by a dimensionless Marangoni number, which is the proportion of surface tension forces on viscous forces. The solutal and thermal Marangoni numbers can be described by the following equations:

Solutal Marangoni number Ma_S:

$$Ma_S = -\frac{\partial \gamma}{\partial C}\frac{L\Delta C}{\mu D_l} \tag{4.2}$$

Thermal Marangoni number Ma_T:

$$Ma_T = -\frac{\partial \gamma}{\partial T}\frac{L\Delta T}{\mu \alpha} \tag{4.3}$$

where γ is the liquid-vapor surface tension, ΔC is the alcohol concentration difference, ΔT is the temperature difference on the drop surface, L is the characteristic length (the drop radius R used in this experiment), μ is the dynamic viscosity, D_l is the alcohol diffusivity in water, and α is the thermal diffusion.

The calculation results of Marangoni number for the water, 1-butanol, and 5% 1-butanol aqueous solution drops as a function of substrate temperature are shown in Fig. 4.11. The thermal Marangoni number is calculated by using the temperature difference on the drop surface at the initial time using infrared measurements. For the calculation of the solutal Marangoni number, the maximum 1-butanol concentration difference is assumed to be 5%, the same as the 1-butanol concentration in the drop. For the 1-butanol aqueous solution drop, the solutal Marangoni number increases linearly with the substrate temperature. However, the thermal Marangoni number decreases first and then increases with the increase of substrate temperature. The minimal value of the thermal Marangoni number is situated at approximately 50°C, which is the specific critical temperature for the 5% 1-butanol aqueous solution. At 80°C, both solutal and thermal Marangoni numbers reach the maximum, which means that both concentration and temperature difference probably have a comparable effect on the Marangoni flow. In addition, the duration of the solutal Marangoni flow is shorter than thermal Marangoni flow which continues to be effective after the depletion of 1-butnaol. These can explain why the increase of evaporation rate by adding 1-butanol is not noticeable at 80°C. Below 80°C, the solutal Marangoni number of the 1-butanol aqueous solution drop is much higher than the thermal Marangoni number; therefore, without the solutal Marangoni effect, the water drop evaporates more slowly than the 1-butanol aqueous solution drop. However, at

80°C, the thermal Marangoni number of the water drop is also at peak. The effect of the concentration difference on the Marangoni flow is no longer significant as mentioned above and the water drop also has an intense convective flow owing to the thermal Marangoni effect. For the pure solution drops, namely water and 1-butanol, only the thermal Marangoni effect occurs. The thermal Marangoni number of the water drop increases with temperature. The value at the substrate temperature of 50°C (approximately 2000) is the critical thermal Marangoni number for the water drop, beyond which convection cells appear. As for the 1-butanol drop, the thermal Marangoni number is always lower than that of the water drop at same substrate temperature.

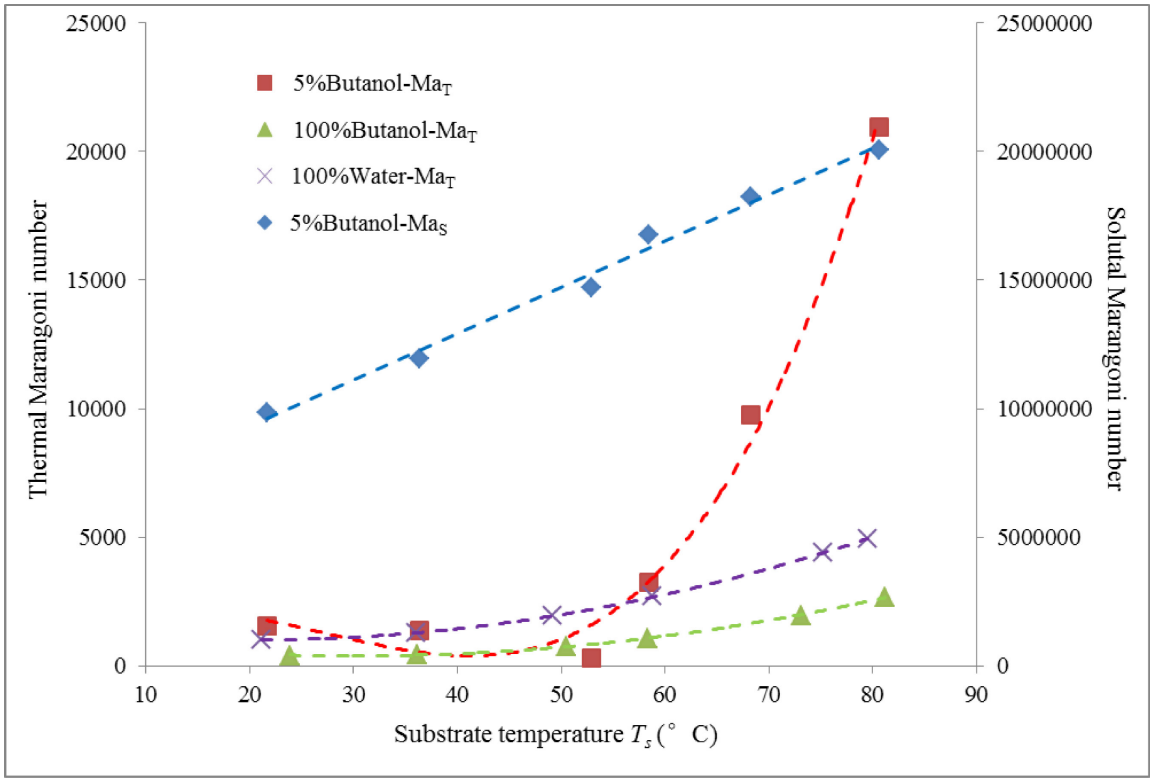

Figure 4.11 Marangoni number of water, 1-butanol, and 5% 1-butanol aqueous solution drops as a function of substrate temperature.

The formula of Hu and Larson can only be applied for the case of pure solutions at ambient temperature where the Marangoni flow is weak. With the increase of substrate temperature, the Marangoni flow is enhanced while the disparity between the measured evaporation rate of the water drop and the prediction value by Hu and Larson's formula increases. As a single-component solution, the Marangoni flow in the water drop is characterized by the thermal Marangoni number. By comparing the experimental data and predicted values, a linear relationship between the ratio of the experimental/predicted evaporation rate and thermal Marangoni number is found:

$$\frac{\dot{V}_{\exp}}{\dot{V}_{Hu\&Larson}} = 1.407\times10^{-4} Ma_T + 1 \tag{4.4}$$

Combining Eq. 4.1, 4.3, and 4.4, we obtain the equation of the evaporation rate when the substrate is heated:

$$\dot{V}_{Water-t_f} = -\underbrace{\frac{\pi R D_a (1-H) C_V}{\rho}(0.27\theta^2 + 1.30)}_{Hu\&Larson\ model\ at\ ambient}\underbrace{(-1.407\times10^{-4}\frac{\partial\gamma}{\partial T}\frac{L\Delta T}{\mu\alpha}+1)}_{Effect\ of\ temperature,\ our\ model} \tag{4.5}$$

The evaporation rate until t_f as predicted by Eq. 4.5 is plotted in Fig. 4.9 (shown as a dashed line). Except for the case at 80°C, the calculated result is very close to the experimental one. At the highest substrate temperature, the thermal patterns or the convection cells created by the thermal Marangoni flow in Fig. 4.4, where multiple cells appear, are extremely different from the cases at lower temperatures. Therefore, there exists another mechanism for heat transfer inside the water drop at 80°C.

The 1-butanol drop evaporates faster than water, but the concentration of 1-butanol in the mixture drop is only 5%; thus, the evaporation rate enhancement of 5% 1-butanol aqueous solution due to the higher evaporation rate of 1-butanol can be neglected. The main reason for the evaporation rate enhancement is the solutal Marangoni flow generated by the 1-butanol concentration difference. Comparing the evaporation rate until t_f of the 5% 1-butanol aqueous solution drop and the evaporation rate of the same duration calculated as a pure water drop by Eq. 4.5, the ratio has an approximate constant value of 1.349. Fig. 4.12 shows the surface tension measurement of different 1-butanol concentration drops at different temperatures. Obviously, the temperature has no effect on the value of $\partial\gamma/\partial C$, which is why the ratio of the experimental/predicted value is independent of temperature. Thus, an equation for the evaporation rate until t_f for 5% 1-butanol mixture drop can be simply obtained as

$$\dot{V}_{Mixture-t_f} = -\underbrace{1.349}_{\substack{Effect\ of\ \text{concentration},\\ our\ model}} \underbrace{\frac{\pi R D_a (1-H) C_V}{\rho}(0.27\theta^2+1.30)}_{Correlation\ of\ Hu\&Larson\ at\ ambient} \underbrace{(-1.407\times10^{-4}\frac{\partial\gamma}{\partial T}\frac{L\Delta T}{\mu\alpha}+1)}_{Effect\ of\ temperature,\ our\ model} \tag{4.6}$$

Following the same steps, the initial evaporation rate prediction equations for the water and 1-butanol aqueous solution drops are deduced as follows:

$$\dot{V}_{Water-t_i} = -\underbrace{\frac{\pi R D_a (1-H) C_V}{\rho}(0.27\theta^2+1.30)}_{Hu\&Larson\ model\ at\ ambient} \underbrace{(-3.196\times10^{-4}\frac{\partial\gamma}{\partial T}\frac{L\Delta T}{\mu\alpha}+0.688)}_{Effect\ of\ temperature,\ our\ model} \tag{4.7}$$

$$\dot{V}_{Mixture-t_i} = -\underbrace{1.913}_{\substack{Effect\ of\ concentration,\\ our\ model}} \underbrace{\frac{\pi R D_a (1-H) C_V}{\rho}(0.27\theta^2+1.30)}_{Correlation\ of\ Hu\&Larson\ at\ ambient} \underbrace{(-3.196\times10^{-4}\frac{\partial\gamma}{\partial T}\frac{L\Delta T}{\mu\alpha}+0.688)}_{Effect\ of\ temperature,\ our\ model} \tag{4.8}$$

The calculated results, which fairly agree with the experimental values, are plotted in Fig. 4.9 and 4.10.

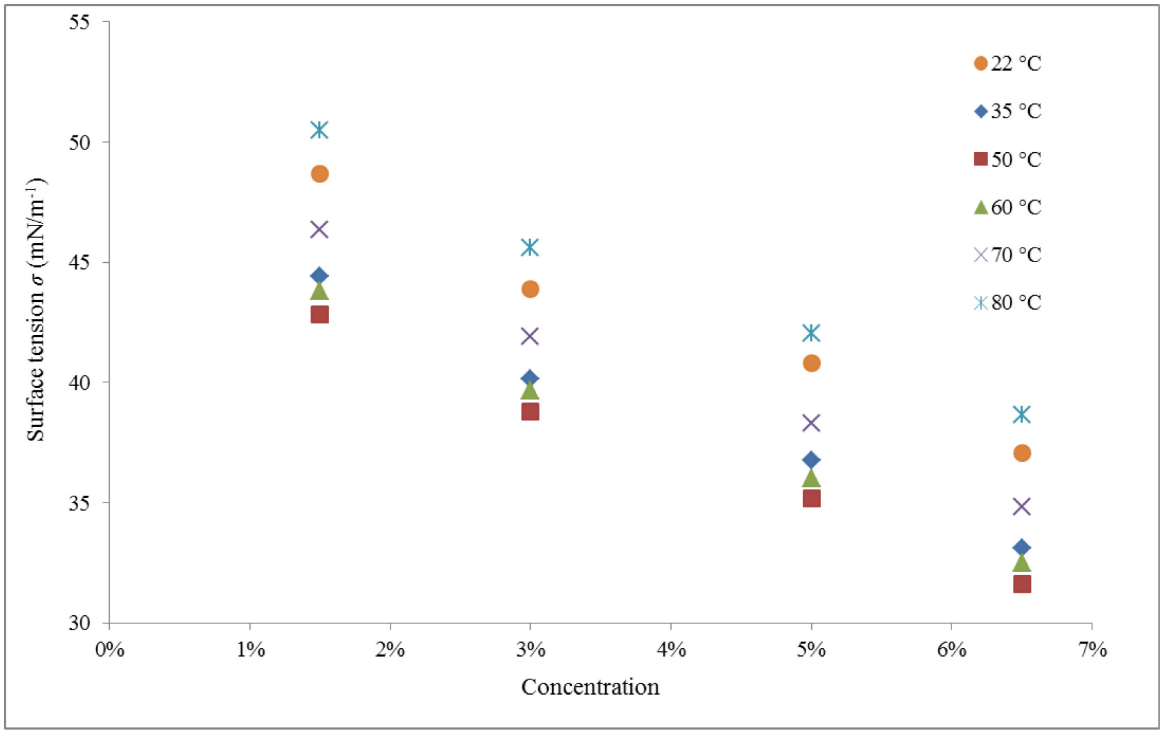

Figure 4.12 Surface tension of different 1-butanol concentration aqueous solution drops at different temperatures.

4.5 Conclusions

A visual method combining a CCD camera and an infrared camera is applied to investigate the dynamic evaporation process of three different solution drops (water, 1-butanol, and 5% 1-butanol aqueous solution) at different substrate temperatures. The behavior of the drops with respect to the contact angle and diameter shows no dependence on the substrate temperature. The 1-butanol drop evaporates faster than that of water. Therefore, for the mixture drop, the 1-butanol is depleted at the first stage of

evaporation and afterward, the water mainly evaporates. Under the infrared camera, the 1-butanol drop shows no thermal instability at different substrates. However, during the earlier periods of evaporation, the convection cells appear on the water drop surface from 50°C and the mixture drop possesses an intensive flow at any substrate temperature owing to the co-existence of the thermal and solutal Marangoni effects. At higher substrate temperatures, the irregular convection cells generated by the solutal Marangoni effect in the mixture drop disappear with the exhaustion of 1-butanol. Then, the regular thermal Marangoni flow continues to act on the drop evaporation. Owing to the addition of 1-butanol and the solutal Marangoni flow created by the alcohol concentration difference, the evaporation rate of the mixture drop is always much higher than the water drop before the depletion of 1-butanol. The model of Hu and Larson is employed to calculate the evaporation rate of the water drop, and the result agrees very well the experimental data at ambient conditions. However, without considering the Marangoni effect contribution, this model underpredicts the evaporation rate when the substrate is heated. The contribution of Marangoni effect is characterized by the Marangoni number; by analyzing the relationship between the experimental data and prediction as a function of the Marangoni number, an empirical equation is developed to calculate the evaporation rate of the water drop at different substrate temperatures. Because the concentration of 1-butanol in the mixture drop is small, the exceeded part of the evaporation rate can be neglected. Another empirical equation for estimating the mixture drop evaporation rate until t_f is obtained based on the preceding equation. With the same steps, the empirical equations for calculating the initial evaporation rate of the water and 1-butanol aqueous solution drop are derived. The results of these equations correspond fairly well to the

experimental data except for the evaporation rate of the water drop at 80°C, which requires further research.

Chapter 5 Effect of Multi Factors on Evaporation Performance of Graphene Nanofluid Droplets

This chapter is based on the manuscript submitted for publication in 2017. The author of this thesis contributed to the designing and performing experiments, analyzing experimental results and writing manuscript. Prof. S. Szunerits and Prof. R. Boukherroub synthesized graphene oxide (GO) and PEGylated reduced graphene oxide (rGO-PEG) nanofluids, and effectuated characterizations, analysis, and manuscript writing of UV/Vis spectrum, Raman spectroscopy, and X-ray photoelectron spectroscopy for GO and rGO-PEG nanofluids. Prof. S. Harmand supported the author of this thesis for the writing of the manuscript and gave approval to the final version.

5.1 Abstract

In this study, the evaporation behavior of graphene nanofluid droplets deposited on sapphire substrate was investigated in the temperature range from ambient to 106 °C. A side-view CCD camera was utilized to record the evaporation process for the droplet profile analysis and a top-view infrared camera was used to observe the temperature distribution on the air/liquid interface of the droplets. Graphene oxide (GO, 0.25 mg/ml), PEGylated reduced graphene oxide (rGO-PEG, 0.25 and 0.8 mg/ml) nanofluids, and water were tested at ambient conditions. The PEGylation was proved to improve the nanoparticles dispersion and the evaporation performance. Preparation without PEG-functionalization, or with an increased nanoparticle concentration, decreases the

evaporation rate due to the poor dispersion of graphene nanoparticles and large accumulation. On heated substrates, 0.25 mg/ml rGO-PEG nanofluid and water have similar behavior in the variation of droplet profile during evaporation, but the evaporation rate of water is dramatically higher than 0.25 mg/ml rGO-PEG nanofluid at high substrate temperature despite the exceptional thermal conductivity of graphene nanofluid. The convective flows induced by thermal Marangoni effect are responsible for the increased evaporation rate of water at high substrate temperature and the application of graphene nanofluid to enhance the heat transfer efficiency is more effective at low substrate temperature.

5.2 Introduction

The prediction of Moore [139] proves that for nearly every two years, the number of transistors contained in an integrated circuit will be double and the miniaturization of electrical elements results in an increased demand of high efficiency heat dissipation. Since the first time used by Choi et al. [27] as a term to refer to the fluids with suspended nanoparticles, nanofluid is considered as an excellent coolant with anomalous high thermal conductivity. Owing to intrinsic high thermal conductivity, pure metals, metal oxides and different nanostructures of carbon are dispersed as nanoparticles in conventional low efficiency heat transfer fluid, as water, ethylene glycol and engine oil etc., to improve thermal performance. Eastman et al. [140] reported an enhancement of 40% of the thermal conductivity of copper ethylene-glycol-based nanofluids with very low volume fraction of 0.3%. In the study of Hong and Yang [141], Fe nanoparticles were found to create a larger increase of thermal conductivity than Cu nanoparticles in

ethylene glycol, which indicated that the enhancement of thermal conductivity is independent of inherent thermal properties of nanoparticles. Patel et al. [142] prepared Ag and Au aqueous nanofluids with citrate stabilization and recorded 5-21% and 7-14% thermal conductivity enhancement for 0.026 vol.% Ag and 0.011 vol.% Au nanofluids, respectively at the same temperature range of 30-60°C. Wang et al. [143] dispersed Al_2O_3 and CuO nanoparticles in different base fluids (water, vacuum pump fluid, engine oil and ethylene glycol) and the experimental results revealed thermal conductivity improvement in base fluids which were higher than predictions from existing models. They proposed that microscopic motion, nanoscale structure, surface properties of nanoparticles should be taken into account for the effective thermal conductivity calculation of nanofluid. Murshed et al. [144] used two different shapes (rod-shape of Ø10nm×40nm and spherical shape of Ø15nm) TiO_2 nanoparticles to prepare aqueous nanofluids and they observed a thermal conductivity increase of approximately 33% for rod-shape and around 30% for spherical shape TiO_2 nanofluids, respectively with 5 vol.% nanoparticle concentration, which unveiled the effect of nanoparticle shape and size. Park and Kim [145] improved the stability of multi-walled carbon nanotubes dispersion by applying a chemical reformation process to adhere the hydroxyl radicals to the oxidized multi-walled carbon MWCNTs' surfaces. At 90°C, the thermal conductivity of MWCNTs nanofluid is 12.6% higher than that for base fluid. Phuoc et al. [146] measured the thermal conductivity and the viscosity of multi-walled carbon nanotubes (MWCNTs) nanofluids with chitosan and the experimental results disclosed a significant enhancement of thermal conductivity that is much higher than the predictions of Maxwell's theory. Tested with difference chitosan

concentration, they found that the thermal conductivity enhancement is independent of the base fluid viscosity, which is contrary to the micro convection theory.

Four possible mechanisms of heat flow in nanofluids are proposed by Keblinski et al. [147] to explain the anomalous enhancement in thermal conductivity: Brownian motion of the particles, molecular-level layering of the liquid at the liquid/particle interface, the nature of heat transport in the nanoparticles, and the effects of nanoparticle clustering. The other theories such as micro convection [148], nanoparticles interaction [149], thermo-phoretic motion [150] etc. are proposed as responsible for the significantly improved thermal conductivity of nanofluids. However, thermal conductivity is only one aspect of thermal characteristics and the practical application of nanofluid in heat transfer improvement is still controversial. Chen et al. [151] applied the pendant drop method to examine the effect of evaporation rate of different nanofluids (Laponite, Fe_2O_3 and Ag) and the experimental results revealed that the additive PVP can not only stabilize the nanofluid solution, but also significantly enhances the evaporation rate of Ag nanofluid by comparing to the base fluid. Yang et al. [152] reported the increase of heat transfer coefficient in laminar flow by application of graphite nanofluid and they supposed instinctive high thermal conductivity and interaction between nanoparticles to be possible reasons. Naphon et al. [153] applied deionized water, alcohol, and nanofluids (alcohol and titanium nanoparticles) as working fluid in heat pipe fabricated from straight copper tube and 10.60% higher thermal efficiency was gained with 0.10 vol.% nanoparticle loading compared to base fluid. You et al. [154] investigated the critical heat flux (CHF) in pool boiling with aqueous Al_2O_3 nanofluids whose concentration varies from 0 to 0.05 g/l. A dramatic enhancement of approximately 200% in CHF was observed with 0.005 g/l

Al_2O_3 nanoparticles. However, the boiling heat transfer coefficients of all nanoparticles loading were the same as pure water for which the authors cannot make any explanation. On the other hand, inconsistent results are reported. Putnam et al. [155] developed an optical beam deflection method to measure the thermal conductivity of nanofluids of C60-C70 fullerenes in toluene and alkanethiolate-functionalized Au in ethanol and toluene. They did not observe abnormal thermal conductivity improvement with low nanoparticle loading (maximum 0.6 vol.%) and the thermal conductivity of nanofluids investigated is independent of nanoparticle concentration. Moghiman and Aslani [156] designed an experimental system to measure the evaporation performance of different aqueous nanofluids (clay, TiO_2, ZrO_2, Fe_2O_3 and Ni/Fe) at different air velocities and compared the results with base fluid. They found that the evaporation performance of base fluid is ameliorated or degraded, depending on the type of nanoparticle and the nanoparticle concentration also has an important influence on the evaporation rate of base fluid. When Putra et al. [157] applied Al_2O_3 and CuO nanofluids in a horizontal cylinder with one end heated, they observed the deterioration of natural convection in the presence of both nanoparticles. Moreover, the deterioration was strengthened with the increase of nanoparticle concentration and the aspect ratio of container. Wen and Ding [158] applied aqueous TiO_2 nanofluid in a horizontal PTFE cylinder with bottom heated to compare the natural convection with pure water. The deterioration of heat transfer coefficient with the presence of nanoparticles was observed, which is intensified with the increase of nanoparticle concentration. The increased viscosity, the concentration gradient driven convection, the interparticle interaction and the deposition of nanoparticle aggregated on the heating surface were supposed to be the reasons of deterioration. Chopkar et al. [159]

investigated ZrO_2 nanofluid dispersed in deionized water to the pool boiling experiment. Surprisingly they found that the highest boiling heat transfer coefficient was obtained at the lowest nanoparticle concentration (0.005 vol.%) and with the increase of nanoparticles loading, the heat transfer was deteriorated even inferior to the application of pure water at the highest nanoparticle concentration (0.15 vol.%). In summary, the application of nanofluid for enhanced heat transfer performance needs more future researches.

Graphene is a single-atom-thick layer of carbon arranged in a 2D honeycomb lattice. Since its discovery by Novoselov et al. [160] in 2004, graphene has attracted numerous interests and one of its exceptional properties is the dramatically high thermal conductivity [161,162]. Thus, the graphene nanofluid is believed to be a good candidate for heat transfer enhancement. Graphene oxide (GO), synthesized via thermal exfoliation method and acid treatment, used as aqueous nanofluid exhibited an enhancement of 64% in thermal conductivity at 50 °C with only 0.056 vol.% GO concentration [163]. After that the same group investigated hydrogen exfoliated graphene (HEG) deionized (DI) water and ethylene glycol (EG) based nanofluids without surfactant [164]. The investigation of thermal performance in straight stainless steel tube showed that the addition of HEG induces considerable enhancement in thermal conductivity and heat transfer compared to the base fluid, which increases with temperature and volume fraction. Yu et al. [165] noticed a significant thermal conductivity enhancement (61.0% with 5.0 vol.% nanoparticles) of ethylene-glycol-based GO nanosheets nanofluid independently of the test temperature. Then they prepared GO nanosheets nanofluids with different base fluids (distilled water, propyl glycol and liquid paraffin) and found that the

addition of GO leads to a larger enhancement of thermal conductivity in base fluid, which possesses lower thermal conductivity [166]. Additionally, Kim and Bang [167] reported thermal resistance decrease and heat transfer coefficient enhancement at the evaporator section of heat pipe with application of GO/water nanofluid. Azizi et al. [168] reported an improvement in thermal performance and overall heat transfer coefficient in two-phase closed thermosiphon filled with graphene/water nanofluid.

In the present study, we examined the potential of PEG-functionalized reduced graphene oxide (rGO-PEG) nanofluid in heat transfer enhancement. rGO-PEG was synthesized in a two-step process from GO. The droplet evaporation performance of rGO-PEG nanofluid, basic phenomenon in heat transfer, is investigated and compared with normal graphene oxide (GO) nanofluid and base fluid (water). The effects of nanoparticle concentration and substrate temperature on evaporation rate are also assessed in this study.

5.3 Experiment Method

5.3.1 Synthesis of GO and rGO-PEG

All chemicals were of reagent grade or higher and were used as received unless otherwise specified. Graphite flakes, chloroacetic acid, sodium hydroxide, poly(ethyleneglycol) bis-(3-aminopropyl) (Mw=1.5 kDa), mercaptoethanol, *N*-(3-dimethylaminopropyl)-*N'*-ethylcarbodiimide (98%, EDC), acetonitrile, methanol and dichloromethane were purchased from Sigma and used as received. GO was prepared from native graphitic flakes according to the modified Hummer's method [169]. Carboxylated rGO (rGO–COOH) was synthesized from GO as described by Turcheniuk et al. [170]. In short,

sodium hydroxide (NaOH, 1.4 g) and chloroacetic acid (Cl–CH_2–COOH, 1 g) were added to 50 mL of an aqueous solution of GO (20 mg) and sonicated at 35 kHz for 2 h at 80°C to convert hydroxyl groups present on GO to COOH via conjugation with acetic acid moieties and partially reduce GO to rGO. The rGO–COOH solution was quenched with HCl (20%), washed (four times) with distilled water until neutral pH and purified by repeated cycles of centrifugation (4000 rpm, 20 min)/rinsing.

5.3.2 Characterization results

Absorption spectra were recorded using a Perkin Elmer Lambda UV/Vis 950 spectrophotometer in plastic cuvettes with an optical path of 10 mm. The wavelength range was 200–800 nm. Zeta-potential measurements were performed using a Zeta-sizer Nano-ZS (Malvern Instruments Inc. Worcestershire, UK). Samples were diluted to 25 μg/mL and measured in Milli-Q water at pH 7.0. Micro-Raman spectroscopy measurements were performed on a Horiba Jobin Yvon LabRam HR micro-Raman system combined with a 473-nm (1 mW) laser diode as excitation source. Visible light is focused by a 100× objective. The scattered light is collected by the same objective in backscattering configuration, dispersed by an 1800 mm focal length monochromator and detected by a CCD camera. X-ray photoelectron spectroscopy (XPS) measurements were performed using a PHl 5000 VersaProbe - Scanning ESCA Microprobe (ULVAC-PHI, Japan/USA) instrument at a base pressure below 5×10^{-9} mbar. Monochromatic AlKα radiation was used and the X-ray beam, focused to a diameter of 100 μm, was scanned on a 250×250 μm surface, at an operating power of 25 W (15 kV). Photoelectron survey spectra were acquired using a hemispherical analyzer at a pass energy of 117.4 eV with a 0.4 eV energy step. Core-level spectra were acquired at a pass energy of 23.5 eV with a

0.1 eV energy step. All spectra were acquired at 90° between X-ray source and analyzer with the use of low energy electrons and low energy argon ions for charge neutralization. After subtraction of the Shirley-type background, the core-level spectra were decomposed into their components with mixed Gaussian-Lorentzian (30:70) shape lines using the CasaXPS software. Quantification calculations were performed using sensitivity factors supplied by PHI. The sample was prepared by casting a concentrated aqueous solution of the material onto silicon substrate followed by drying at 100 °C for 1 h.

The GO investigated in this work was synthesized according to a modified Hummer's method, while the PEGylation of GO involved a two-step reaction. GO was first enriched with carboxylic acid groups through chemical reaction with chloroacetic acid under strong basic conditions (0.7 M) at 80°C. Under these experimental conditions, the epoxy and ester groups, on GO surface, were converted into hydroxyl groups, which were in turn transformed into carboxylic acid (-COOH) moieties via reaction with chloroacetic acid. At the same time GO was partially reduced to yield rGO-COOH. To improve the solubility and stability of the rGO-COOH nanosheets in aqueous media, PEGylation was performed with a polyethylene glycol diamine (PEG-NH_2; MW=1.5 kDa) via EDC activation reaction at 40°C through amide bond formation.

The UV/Vis spectrum (Fig. 5.1(a)) of GO shows a main absorption peak at around 229 nm due to π-π* transition from the C=C bonds, while rGO-PEG shows a higher absorption in the NIR and a red shift of the main absorption band to 269 nm. The result suggests that the GO nanosheets have been partially reduced to reduced graphene oxide

(rGO) and the electronic conjugation within the rGO nanosheets was partially restored. The zeta potential of GO in water was determined as -40±2 mV.

Raman spectroscopy was used in addition to investigate GO and rGO-PEG sheets. Fig. 5.1(b) shows the expected D (≈1350 cm^{-1}) and G (≈1580 cm^{-1}) bands for carbon based materials, which are assigned to the local defects/disorder and the sp^2 graphitized structure of GO. The ID/IG intensity ratio was determined to be 1.19 for GO and 0.72 for rGO-PEG; the smaller ID/IG peak intensity of rGO-PEG, corresponding to lower defect/disorders, is due to the improvement in the sp^2 graphitized rGO-PEG structure of the sheets during the reduction process. The 2D band at 2712 cm^{-1} is highly sensitive to stacking degree of the sheets. While a single-layer graphene sheet exhibits a 2D band at 2679 cm^{-1}, for multi-layered graphene sheets the 2D band appears as a broadened peak with 19 cm^{-1} shift into higher wavenumbers. In the case of GO the 2D band is positioned at 2714 cm^{-1}, while rGO-PEG shows a broad band centered at 2919 cm^{-1}, indicating that monolayer to bilayer structures are predominant in GO while rGO-PEG has a multilayered structure.

X-ray photoelectron spectroscopy (XPS) was in addition used to follow the chemical changes that occurred upon carboxylation and PEGylation of GO. Fig. 5.1(c) depicts the C_{1s} core level XPS spectra of GO and rGO-PEG. In the case of GO, the spectrum can be deconvoluted into three bands at 287.9 eV (C=O), 286.5 eV (C-O) and 284.5 eV (C-C) with a C/O ratio of 2.3.

To improve the solubility and stability of the GO, PEGylation was performed via EDC activation reaction at 40°C. Conjugation of PEG-NH_2 to rGO-COOH was confirmed by

the presence of 2.3 at.% of N_{1s} in the XPS spectrum (data not shown). The C_{1s} high resolution XPS spectrum of rGO-PEG is comparable to that of GO, with an increase of the band at C-C (285.1 eV) due to the integration of PE units.

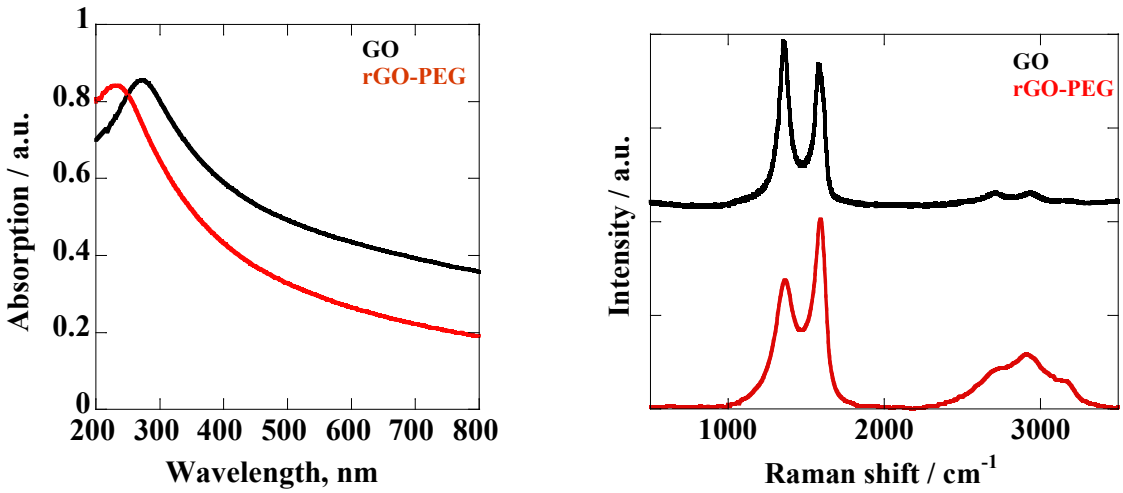

(a) (b)

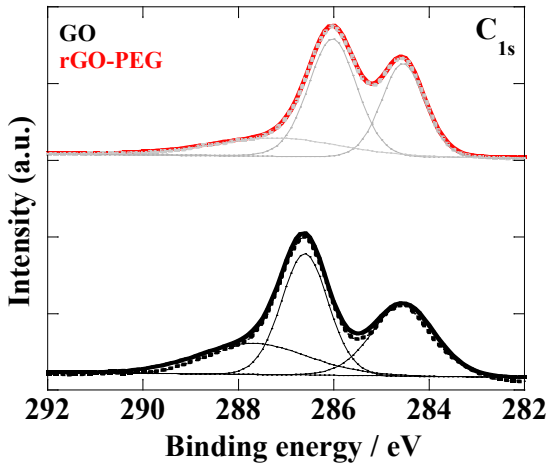

(c)

Figure 5.1 Characterization results of GO and rGO-PEG nanofluid: (a) UV-vis absorption spectra, (b) Raman spectra, and (c) C_{1s} high resolution XPS spectra.

5.3.3 Experimental setup

The optical and infrared techniques were applied to investigate the dynamic evaporation of droplets of graphene nanofluid and base fluid. The droplet is formed by an automatic dosing system, which can control the volume of droplet as well as dosing speed, and then is deposited on a sapphire substrate below which there is a black-painted heater connected to an electrical controller (see Fig. 5.2). The substrate and heater are positioned in a vapor chamber (14 cm × 12.4 cm × 7.5 cm) with controlled ambient temperature and relative humidity. A side-view CCD (charge-coupled device) camera (Allied Vision Technologies, 15 fps, 780×580 pixels) records the evaporation process and then the software Kruss® Drop Shape Analyzer (DSA) analyzes the profile of droplets by recorded videos and the evolutions of droplets' contact angle (incertitude ± 0.1°), volume and diameter are accessible. On the top of the vapor chamber, there are a sapphire window for the infrared camera and a hole for passing the syringe. The infrared camera (FLIR X6580SC, 640 × 512 pixels, 200Hz, 15 μm detector pitch) records the evaporation process at the top view and provides the dynamic temperature distribution (incertitude ± 1°C) on the surface of the droplets. The volume of droplets for all the liquids is controlled at 1 μL. The droplet evaporation was carried out at an ambient temperature of 22 °C and a relative humidity of 50 %. The substrate temperature was varied from ambient to 106 °C in order to investigate the influence of substrate temperature on the evaporation process.

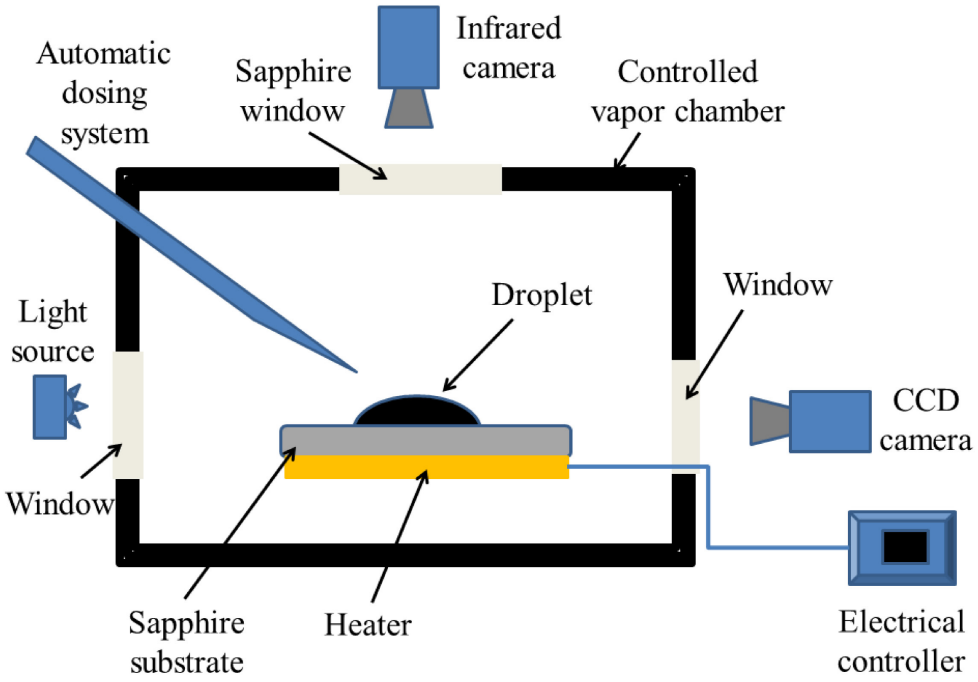

Figure 5.2 Schematic of the experimental setup of Kruss® drop shape analyzer and infrared camera.

5.4 Results and Discussion

5.4.1 Experimental results at ambient conditions

In this research on evaporation performance, graphene oxide (GO, 0.25 mg/ml), and rGO-PEG (0.25 and 0.8 mg/ml) nanofluids were tested on a hydrophilic sapphire substrate. A droplet of pure water was also tested for comparison. The PEGylation of rGO was applied to improve solubility and stability of the graphene nanofluid and thus prevent its sedimentation. Fig. 5.3 shows photographs of GO and rGO-PEG nanofluid samples, three months after preparation. The GO nanofluid (Fig. 5.3(a)) has apparent graphene nanoparticle sediment at the bottom of the bottle, while the rGO-PEG nanofluid

(Fig. 5.3(b)) still reveals a good dispersion of graphene nanoparticles without any apparent sedimentation. The study of Turcheniuk et al. [170] has also demonstrated that the rGO-PEG shows perfect solubility and stability in water and even after 6 months, no agglomeration can be observed. The PEG-functionalization is thus confirmed as a good strategy for stabilizing the nanofluid for a comparatively long period of time. The experiments were primarily performed under ambient environment conditions and Fig. 5.4 presents the droplet profile analysis results.

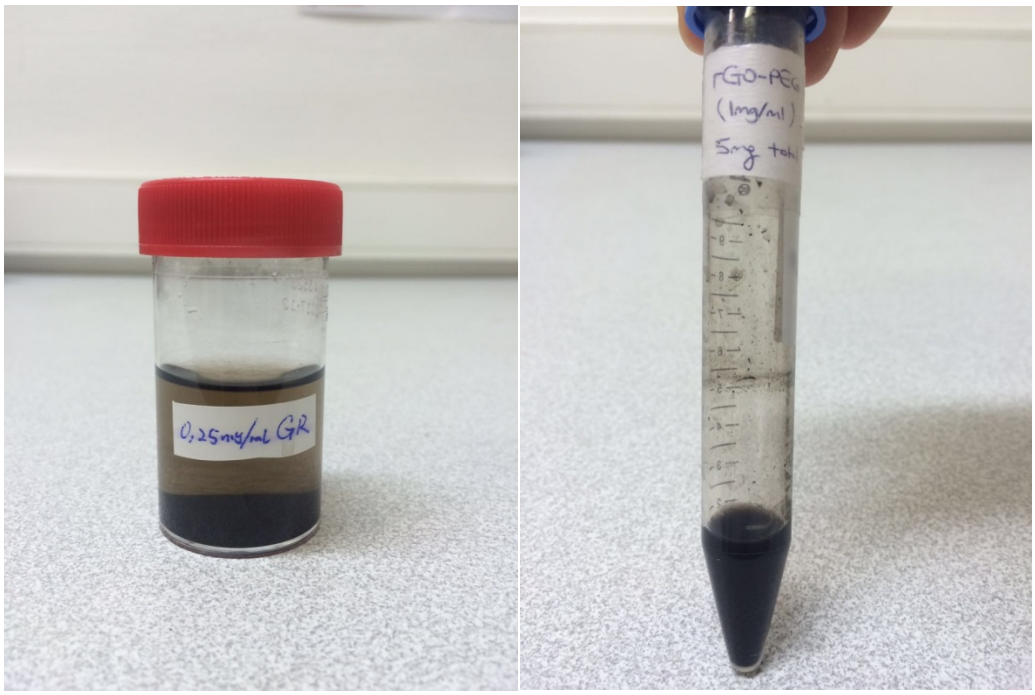

(a) (b)

Figure 5.3 Sedimentation of graphene nanofluids: (a) 0.25 mg/ml GO, and (b) 1 mg/ml rGO-PEG. Photographed three months after preparation.

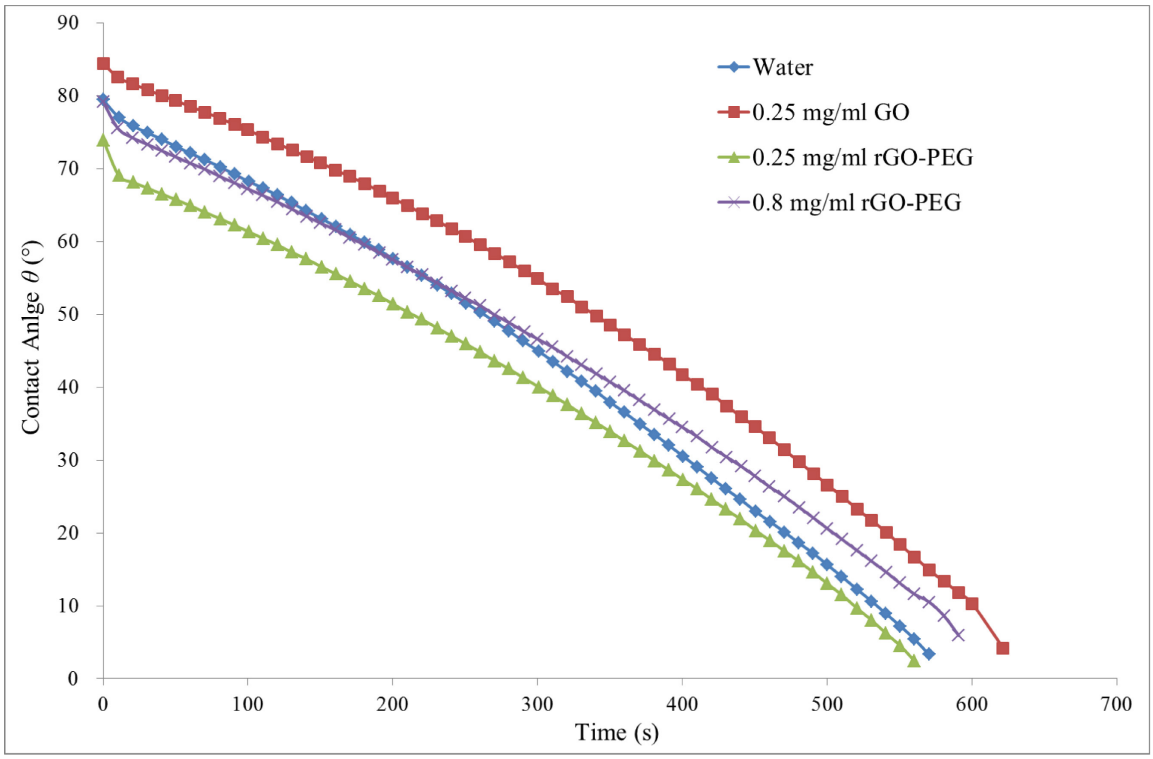

(a) Contact angle

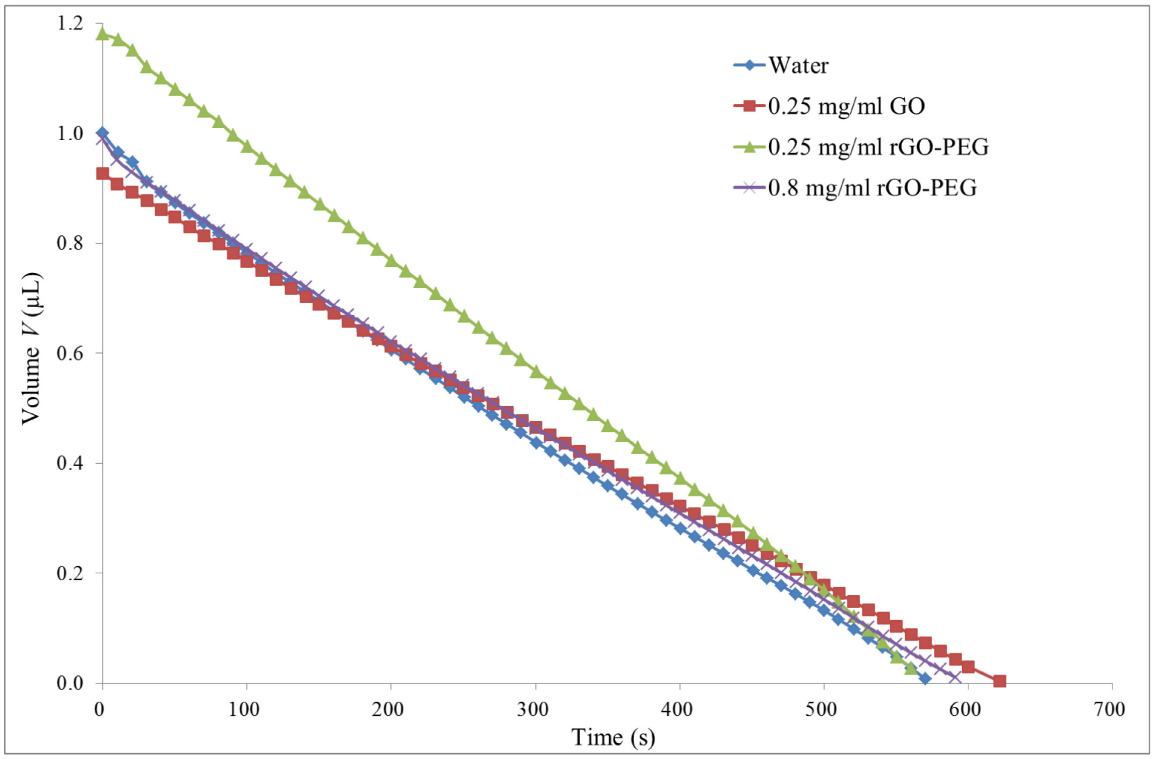

(b) Volume

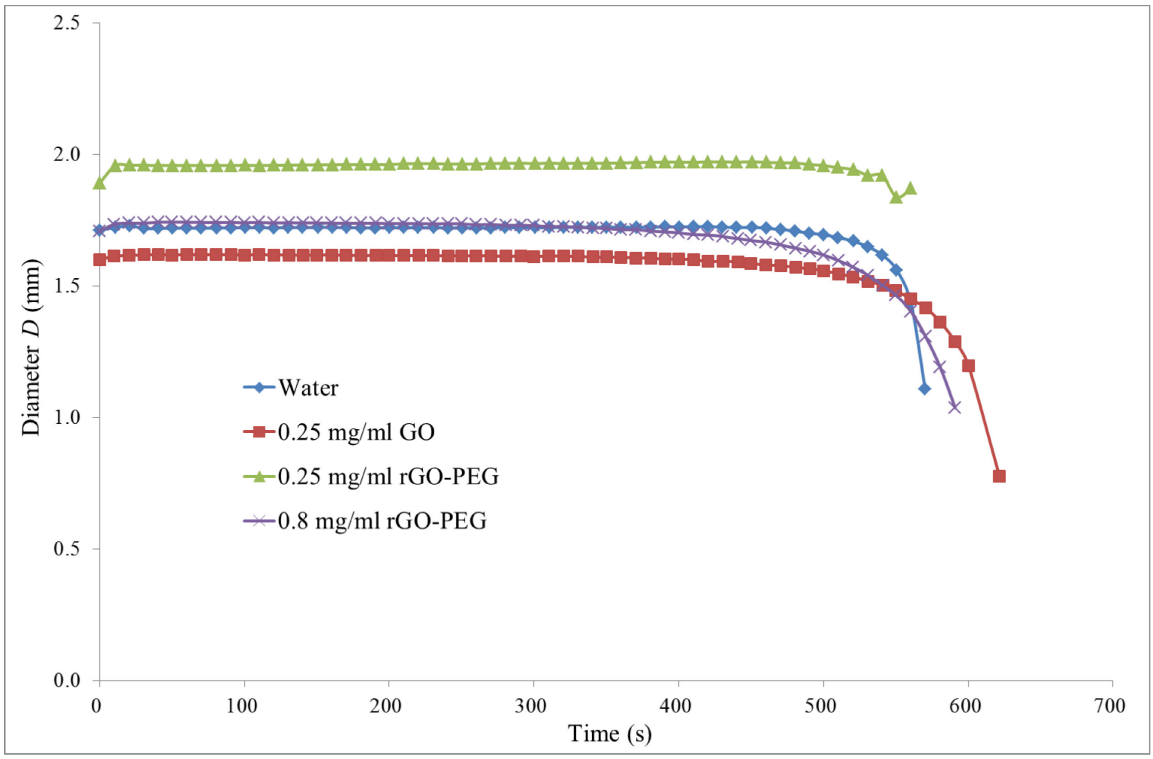

(c) Diameter

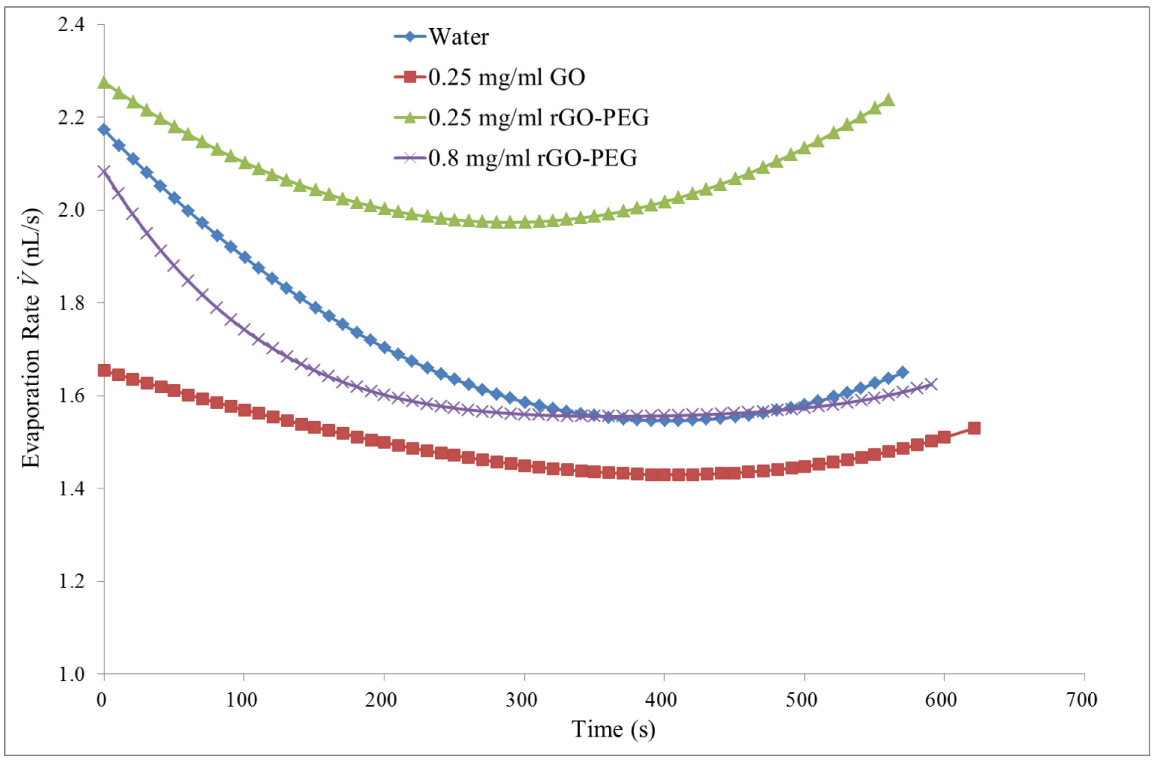

(d) Evaporation rate

Figure 5.4 Droplet behavior during evaporation: evolution of (a) contact angle, (b) volume, (c) diameter, and (d) evaporation rate. Samples used are pure water, GO nanofluid (0.25 mg/ml) and rGO-PEG nanofluid (0.25 and 0.8 mg/ml). All experiments were carried out at 22 °C ambient temperature and 50% relative humidity.

The droplets of all the graphene nanofluid samples have similar evaporation behavior as that of pure water, i.e., the typical constant contact line regime. The contact angle of each droplet decreases continuously during evaporation, while the diameter remains constant until it shrinks rapidly at the end. It seems that PEG-functionalization and the difference in rGO-PEG concentration have no influence on the evolution of the droplet profile, as seen by comparing the 0.25 mg/ml GO and rGO-PEG nanofluids results, and also from the 0.8 mg/ml rGO-PEG nanofluid results. The only significant difference is in the instantaneous evaporation rate. The droplets of 0.25 mg/ml rGO-PEG nanofluid have the highest evaporation rate, while the same concentration of GO nanofluid has the lowest. For the pure water and 0.8 mg/ml rGO-PEG nanofluid, the instantaneous evaporation rates are very close but the rate for pure water is somewhat higher. At ambient temperature, the dominant heat transfer inside the droplet is thermal conduction. With its extraordinarily high thermal conductivity, the rGO-PEG nanofluid is expected to evaporate much faster than water base-fluid alone; the result obtained for 0.25 mg/ml rGO-PEG nanofluid confirms this assumption. However, the 0.25 mg/ml GO, and the 0.8 mg/ml rGO-PEG, exhibit contradictory results. The former case can be explained by degraded thermal conduction, and hence reduced evaporation, resulting from poor dispersion of GO in water. For the latter case, with a higher concentration of rGO-PEG, it is suggested that agglomeration inside the droplet can easily take place, resulting in

reduced thermal conduction and evaporation. The ideal graphene nanofluid should have good stability with appropriate nanoparticle concentration.

Fig. 5.5 shows microscopic images of graphene nanoparticle deposition after evaporation. In this experiment, all droplets are in the constant contact line regime because of the hydrophilic substrate. Most of the evaporation takes place at the contact line, leading to outward capillary flow from the droplet center to the periphery. The outward flow transports the nanoparticles to the contact line where they deposit at the edge of the meniscus region. As evaporation progresses, more and more nanoparticles accumulate and the "coffee ring" left after evaporation is obvious in all the microscopic photographs. As seen in the image for 0.25 mg/ml GO nanofluid (Fig. 5.5(a)), the non-uniform dispersion of nanoparticles results in a heterogeneous deposition of GO inside the "coffee ring," with some locations free of nanoparticles. Nevertheless, large clusters of GO nanosheets are found. For the 0.25 mg/ml rGO-PEG nanofluid (Fig. 5.5(b)), a large fraction of the nanoparticles is accumulated at the contact line, and those remaining form a thin and homogeneous layer inside the "coffee ring" which indicates improved dispersion of PEGylated nanoparticles. For the sample with higher concentration (0.8 mg/ml) (Fig. 5.5(c)), trails indicating the degradation of nanoparticle dispersion are seen in the microscopic photograph. The "coffee ring" is wider and darker, indicating more nanoparticles are deposited there, and a second ring appears, much wider but less dark. Between the first and the second rings, bare nanoparticles are observed. Inside the second ring, the deposition of nanoparticles is no longer uniform and there are large nanoparticle clusters. These observations of nanoparticle deposition confirm the assumption about the nanoparticle dispersion status of the three nanofluid samples.

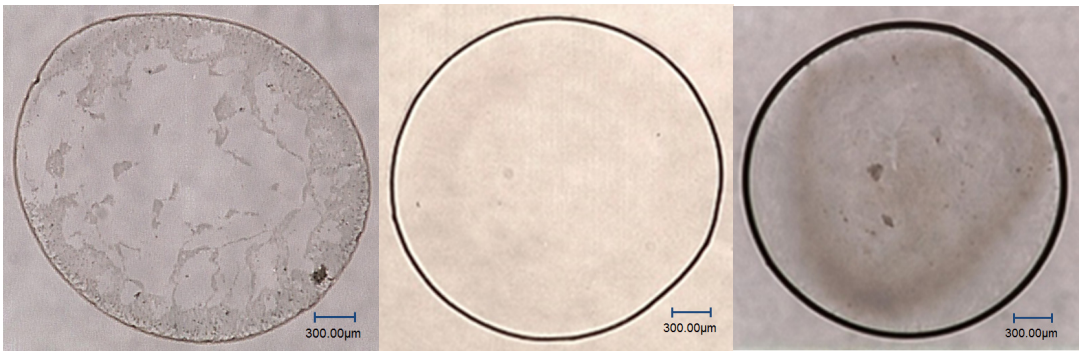

(a) 0.25 mg/ml GO (b) 0.25 mg/ml rGO-PEG (c) 0.8 mg/ml rGO-PEG

Figure 5.5 Microscopic photographs of nanoparticle deposition from graphene nanofluids: (a) 0.25 mg/ml GO, (b) 0.25 mg/ml rGO-PEG, and (c) 0.8 mg/ml rGO-PEG.

In order to understand the mechanism of nanoparticle deposition, the evaporation of graphene nanofluid droplets was investigated under a microscope. In Fig. 5.6, the contact line of a 0.8 mg/ml rGO-PEG nanofluid droplet is shown (22 °C environmental temperature, 50% relative humidity). As evaporation progresses, the nanoparticles separate into three layers: (1) sediment at the solid/liquid interface, (2) a stream towards the contact line by capillary flow, and (3) dispersion at the air/liquid interface. Some larger particles deposit at the bottom of the droplet in the first stage of sedimentation; they remain in their initial location throughout evaporation. The stream of graphene nanoparticles is transported by an outward capillary flow, and during the early stage of evaporation, the nanoparticles move slowly toward the droplet periphery with fluctuations, indicating Brownian motion. Because of the high contact angle, these nanoparticles can reach a location very close to the contact line and accumulate there, forming the first ring. At the same time, the remaining nanoparticles, which are out of the outward flow, disperse homogeneously at the air/liquid interface. As a result of

evaporation, the contact angle decreases slowly and the nanoparticle dispersion is also slowly driven to the summit of the droplet by the surface tension of water. As the evaporation progresses, the velocity of the outward nanoparticle stream increases and the nanoparticle dispersion at the air/liquid interface shrinks more rapidly. During the last stages of evaporation, the contact angle becomes so small that the nanoparticles in the stream do not approach the contact line and deposit at a distance away or join the dispersed nanoparticles at the air/liquid interface. The strong surface tension separates the nanoparticle dispersion from the accumulation at the contact line, creating a vacancy of nanoparticles in the gap; the concentration of dispersed nanoparticles at the air/liquid interface forms the second ring. In the case of the 0.25 mg/ml rGO-PEG nanofluid, the nanoparticle dispersion at air/liquid interface is thinner and a thin layer of nanoparticles remains inside the “coffee ring”; the region with a vacancy of nanoparticles is much narrower. In contrast, for the GO nanofluid, the poor dispersion of nanoparticles results in a heterogeneous deposition inside the “coffee ring”. The supposition about the heat transport mechanism inside the droplets is confirmed by analysis of the microscopic videos.

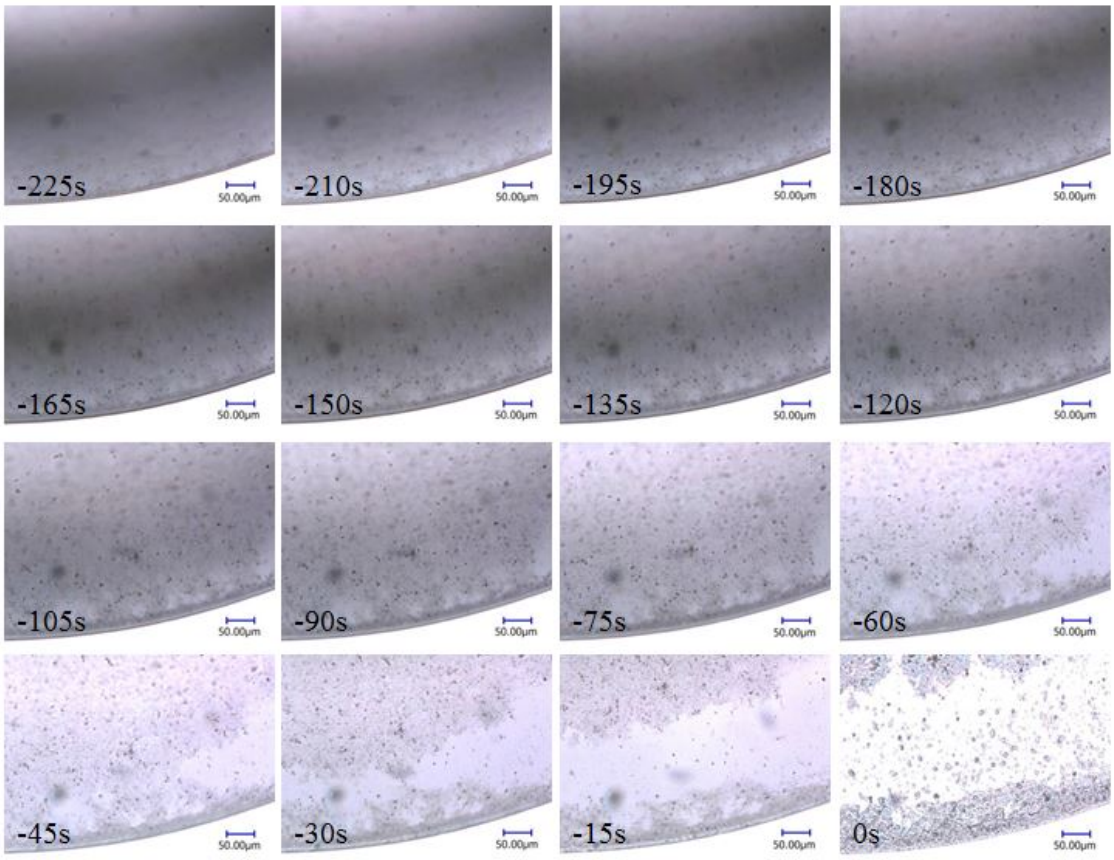

Figure 5.6 Evaporation along the contact line. Photographs from the microscopic video for a 0.8 mg/ml rGO-PEG nanofluid droplet. Taken at an ambient temperature of 22 °C and 50% relative humidity. Magnification is 1000×; the scale bar is 50 μm. The end of evaporation is denoted as 0 s; negative times indicate the period of evaporation.

5.4.2 Experimental results on heated substrates

In the previous part, the evaporation properties of different graphene nanofluids and water were studied under ambient conditions. The temperature has a central influence on the dynamic viscosity, the thermal conductivity, and the specific heat capacity of fluids so two graphene nanofluids (0.25 mg/ml GO and rGO-PEG) and water were tested on heated sapphire substrates to investigate the effect of substrate temperature (The ambient

temperature and relative humidity were 22 °C and 50%, respectively). From the previous results, it was found that an increase of rGO-PEG nanoparticle concentration had no influence on the enhancement of droplet evaporation rate; the 0.8 mg/ml rGO-PEG nanofluid is therefore not included in the heated substrate tests.

The sapphire substrates were heated at different temperatures (50, 66, 84, 106 °C) and the profile analysis shows no evident influence of substrate temperature on the evolution mode of the contact angle, volume, and diameter. However, the substrate temperature plays an important role in determining the time for complete evaporation of the droplets. The results of evaporation rate are displayed in Fig. 5.7; the inset is an enlarged view at lower temperatures. Each test was repeated 6 times to ensure the reproducibility of the experiments and the average values are presented in the figure. The evaporation rates of all liquids increase significantly with the rise of substrate temperature. As previously observed for ambient temperature, the evaporation rate for GO nanofluid is lower than that of the other two liquids (water, rGO-PEG nanofluid) at all substrate temperatures investigated. The probable reason is that instabilities in the GO nanofluid lead to agglomeration of nanoparticles, which reduces the heat transfer efficiency. Having large nanoparticle clusters and subsequently a low evaporation rate, the GO nanofluid is not a suitable material for evaporation performance improvement, and is not included in the following analysis.

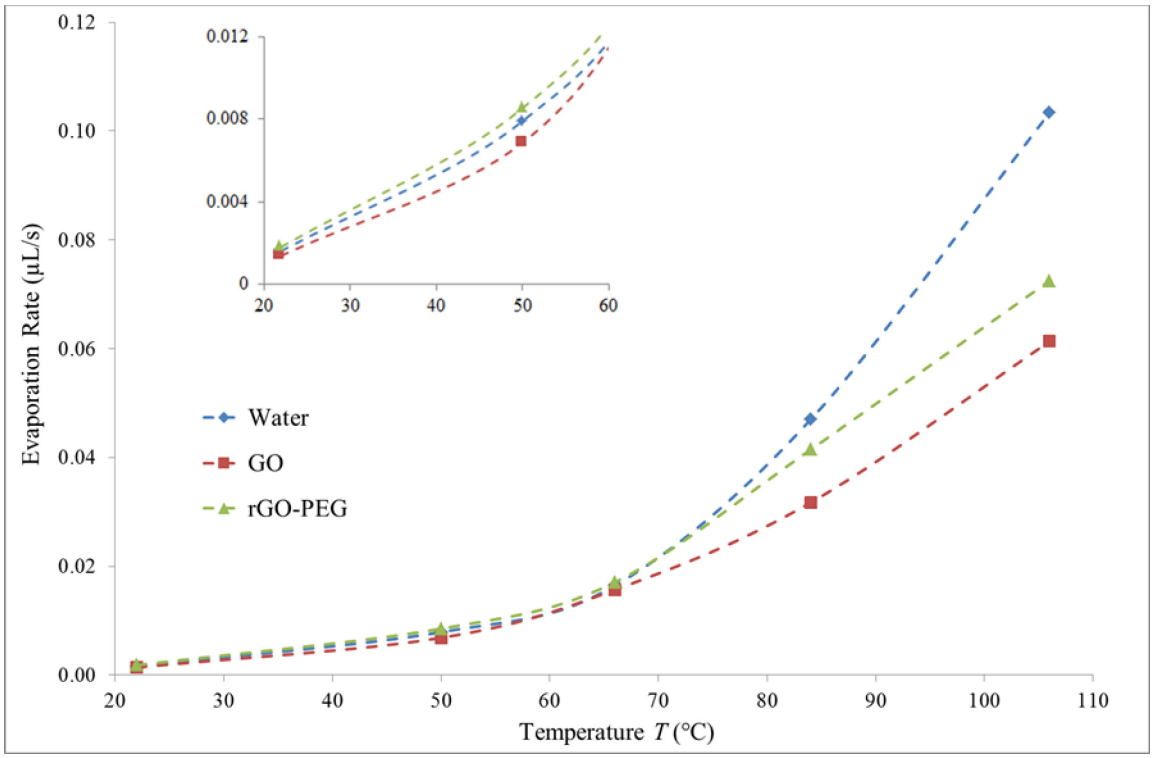

Figure 5.7 Evaporation rates for pure water and 0.25 mg/ml graphene nanofluid (GO and rGO-PEG) as a function of substrate temperature.

For the rGO-PEG nanofluid, the addition of graphene nanoparticles enhances the thermal performance of the base fluid at low substrate temperatures (22 and 50 °C). However, the situation is reversed at high substrate temperatures (84 and 106 °C) that the evaporation rate of the rGO-PEG nanofluid is significantly much lower than that of water. Tab. 5.1 shows the change in the evaporation rate of pure water droplets resulting from addition of graphene nanoparticles, with negative values signifying degradation. Adding graphene nanoparticles (0.25 mg/ml rGO-PEG) enhances the evaporation rate of water droplets by 12.1% (the maximum increase observed) at 22 °C substrate temperature; subsequently, the enhancement decreases with increasing substrate temperature. The enhancement becomes negative at around 66 °C, above which the water droplets evaporate faster than

that of rGO-PEG nanofluid. Thus, an improvement in thermal performance upon addition of graphene nanoparticles is no longer a valid assumption for higher substrate temperatures.

Substrate Temperature (°C)	Evaporation Rate Enhancement (%)
22	12.1
50	8.0
66	3.6
84	-11.8
106	-29.9

Table 5.1 Enhancement of evaporation rate by addition of graphene nanoparticles. (Data from Fig. 6; water and 0.25 mg/ml rGO-PEG nanofluid).

In order to explain this evaporation rate behavior, the temperature distribution on the surface of droplets for different substrate temperatures are observed from infrared images (Fig. 5.8). For the rGO-PEG nanofluid, thermal instability is not detected at any substrate temperature. However, for a substrate temperature T_s = 66 °C, convection cells are apparent on the surface of water droplets; these become more distinct and intense at higher substrate temperatures. The observation is in accordance with the previous study on hydrophobic silicon substrates [125]. Coincidentally, the water droplet evaporates faster than the rGO-PEG nanofluid when the substrate temperature exceeds 66 °C. The heat transfer mode for both liquids at low substrate temperature is thermal conduction; other reports [163-166] have shown that addition of graphene nanoparticles can significantly augment the thermal conductivity of a base fluid, so it is consistent that the graphene nanofluid shows better thermal performance than water at low temperature. However, with increased substrate temperature, thermal convection appears inside the water droplet, while the graphene nanofluid droplet continues to transfer heat from the

substrate by conduction only. The addition of convection improves the heat transfer efficiency of the water droplet, and its evaporation rate becomes considerably higher than that of the rGO-PEG nanofluid.

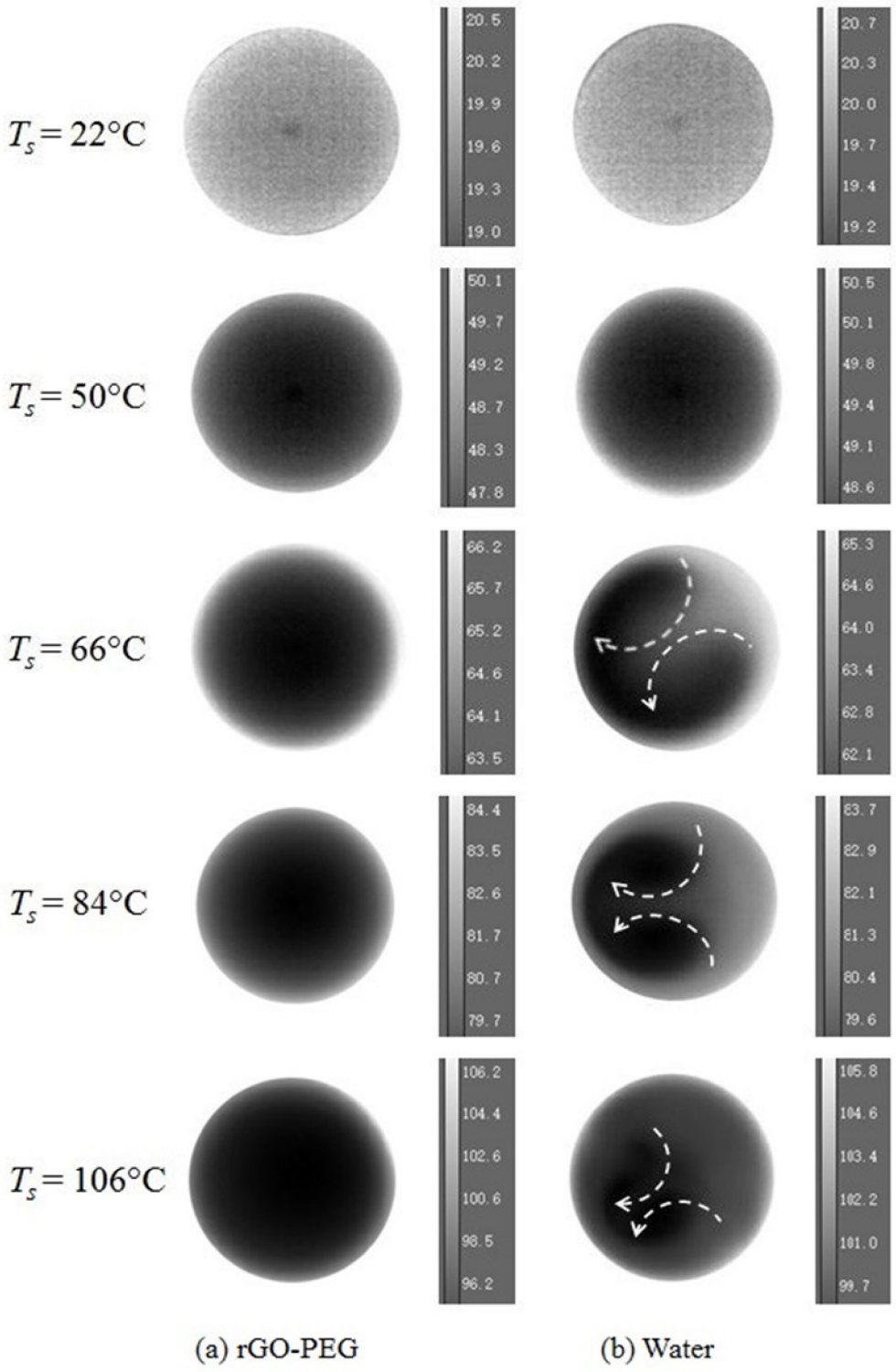

Figure 5.8 Evaporation of droplets of (a) rGO-PEG nanofluid and (b) water, for different substrate temperatures T_s. Photographs taken from infrared videos.

From the infrared videos, the highest temperature is found at the contact line and the lowest temperature is normally situated at the top of the droplet. The temperature difference between the contact line and the top of the droplet surface drives a thermal Marangoni effect. Nevertheless, for water droplets on the higher temperature substrates, the lowest temperature is located near the top because of convection. From infrared camera thermal mapping data, the initial temperature differences across the droplet surface of water and rGO-PEG nanofluid were measured when the droplets were placed on the substrates as a function of substrate temperature (Fig. 5.9). The initial temperature difference increases with the rise of substrate temperature for both liquids, and (with the exception of the unheated substrate) is always higher for the graphene nanofluid droplet than for water. The graphene nanofluid is assumed by many researchers to possess a significantly higher thermal conductivity than water, implying that the temperature at the top of the droplet is closer to that at the contact line than for water. However, the experiments indicate the converse, with convection in the water droplet making the temperature distribution on the surface more homogeneous than for the graphene nanofluid.

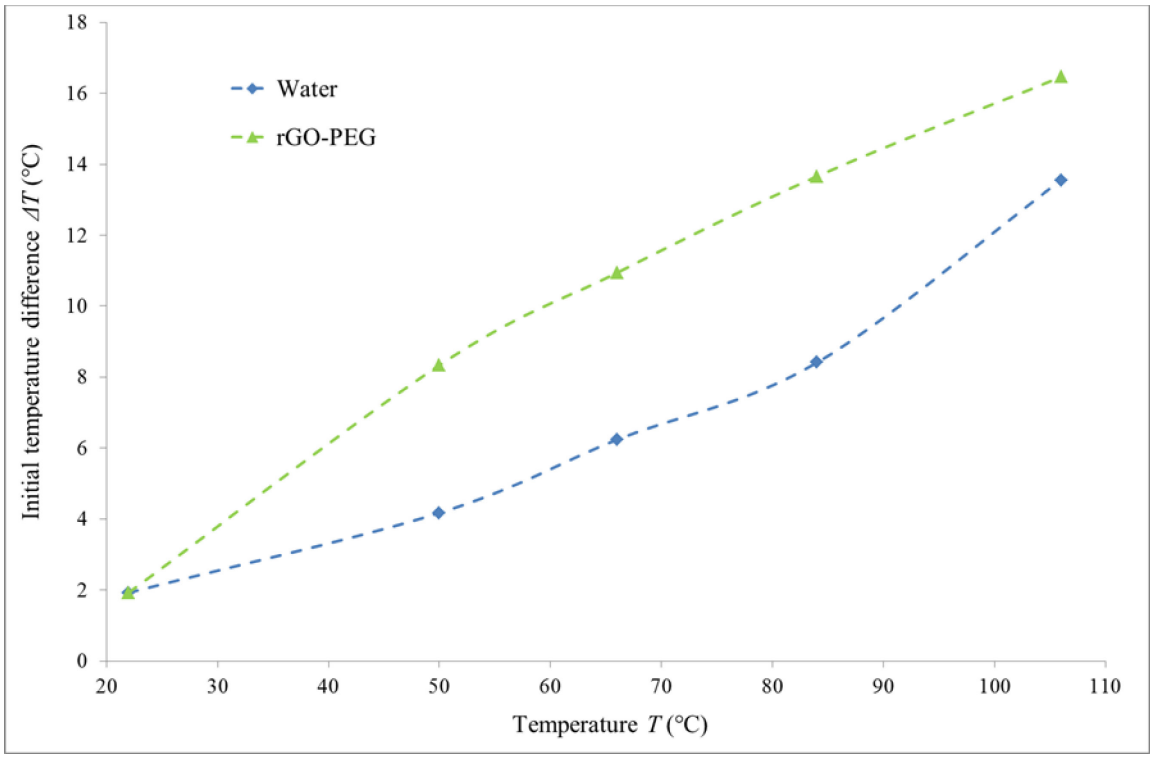

Figure 5.9 Initial temperature difference across the droplet surface as a function of substrate temperature. Samples are pure water and 0.25 mg/ml rGO-PEG nanofluid.

Regarding the instantaneous temperature difference, the tests recorded on substrates heated at 50 °C and 84 °C are presented in Fig. 5.10. In the case of 50 °C, the temperature difference of rGO-PEG nanofluid droplet suffers a quick and sharp drop at the beginning and then decreases linearly until the end of evaporation. The same trend can be found in the case of 84 °C for rGO-PEG nanofluid. In a study by David et al. [171], they also observed the preheating stage of sessile droplet after deposition on heated substrate and then the droplet reaches a steady evaporation state. For the droplet of pure water, the evolution of temperature difference has a slight decrease after deposition at 50 °C. However, the temperature difference across the water droplet surface stays flat at the first stage due to thermal convection at substrate temperature of 84 °C. At around 10 s, when

the thermal convection under infrared camera becomes weakened and disappears gradually, the temperature difference begins to decrease non-linearly. The existence of thermal convection maintains the temperature difference on the surface of water droplet during first evaporation stage. Therefore, the evaporating droplets of rGO-PEG show the same evolution of temperature difference with preheating stage at difference substrate temperatures, but for water droplets, the evolution of temperature difference on surface have two different modes, which depend on the existence of thermal convection.

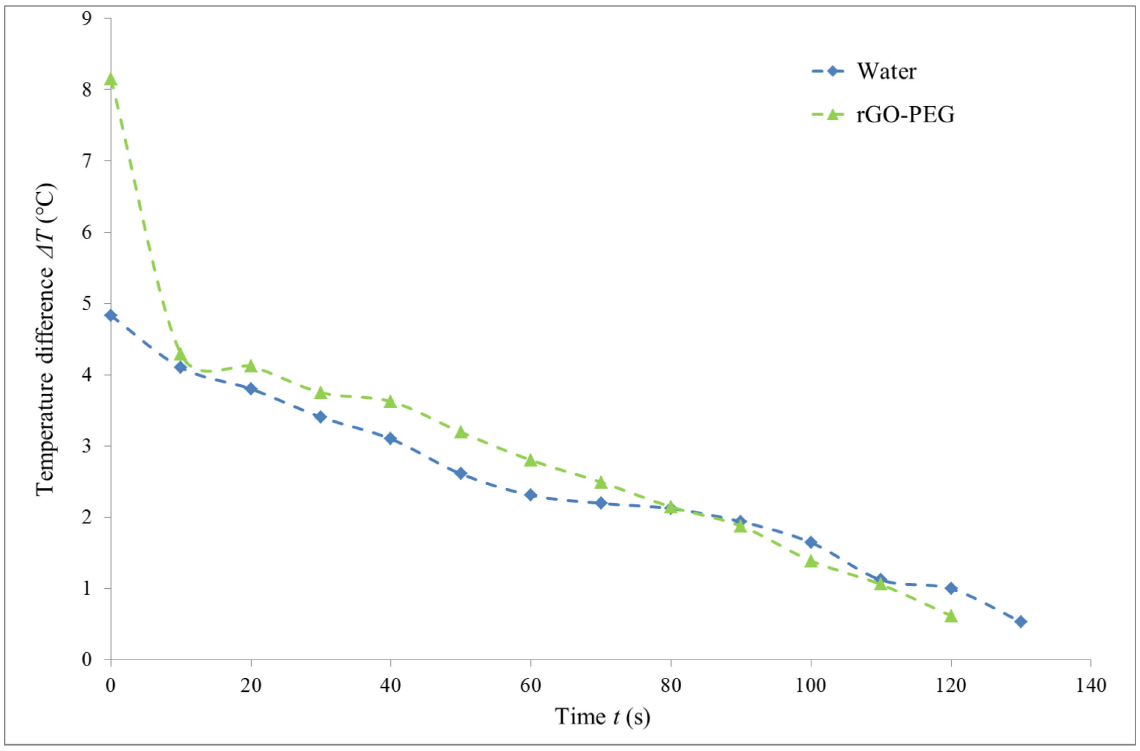

(a) $T = 50$ °C

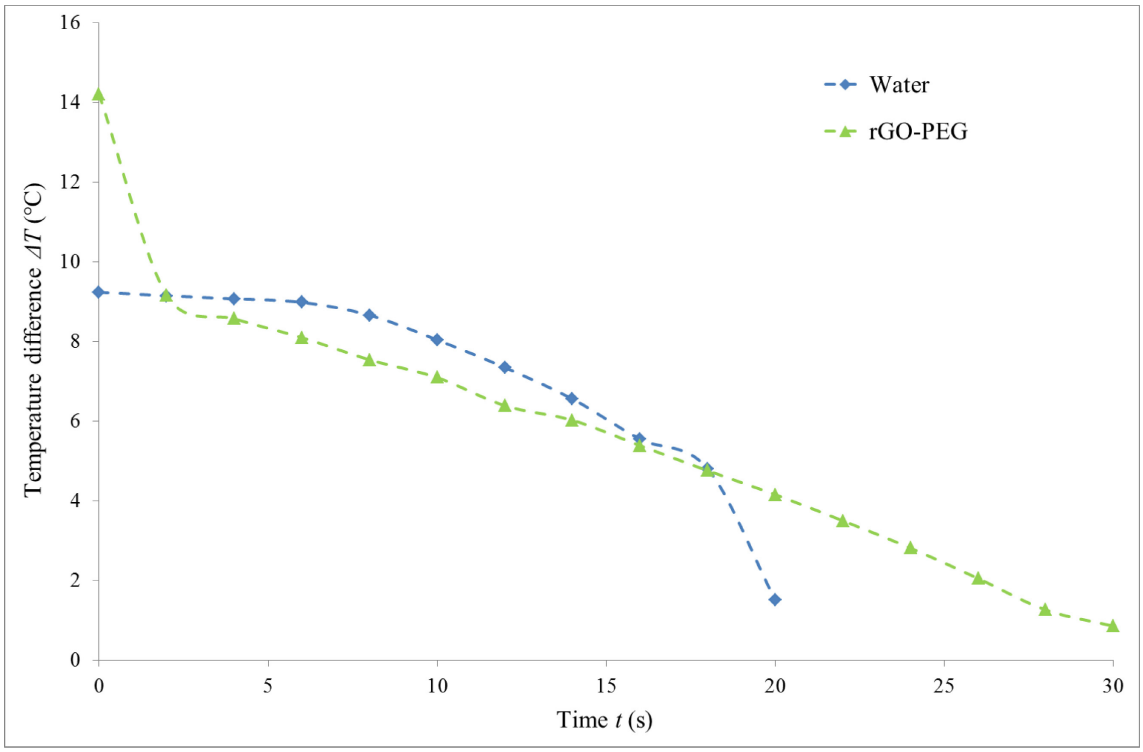

(b) $T = 84$ °C

Figure 5.10 instantaneous temperature differences across the droplet surface as a function of time. Samples are pure water and 0.25 mg/ml rGO-PEG nanofluid at substrate temperatures of (a) 50 °C and (b) 84 °C.

Thermal convection in a single-component droplet can be driven by either gravity or surface tension. In this study, the droplets are so small that their radii are less than the capillary length. As a result, the effect of gravity as a buoyancy force can be excluded. Moreover, in our previous study using hydrophobic silicon substrates at high temperatures, convection cells appeared in pure water droplets but not in pure butanol droplets [125]. If the convection cells are generated by buoyancy, they will exist in the droplets of both liquids. Therefore, the convection cells in the present study are surface tension driven, with a gradient in surface tension caused by the temperature difference

across the water droplet surface. This is the so-called thermal Marangoni effect, which is characterized by the thermal Marangoni number:

$$Ma_T = -\frac{\partial \gamma}{\partial T}\frac{L\Delta T}{\mu \alpha} \tag{5.1}$$

where γ is the liquid-vapor surface tension, ΔT is the temperature difference across the droplet surface, L is the characteristic length (the drop radius R used in this experiment), μ is the dynamic viscosity, and α is the thermal diffusivity. The thermal diffusivity can be expressed by $\alpha = \frac{k}{C_{p,v}}$ where k is the thermal conductivity and $C_{p,v}$ is the volumetric heat capacity. Consequently, the thermal Marangoni number can be written as:

$$Ma_T = -\frac{\partial \gamma}{\partial T}\frac{RC_{p,v}\Delta T}{\mu k} \tag{5.2}$$

Some of the properties required to calculate the thermal Marangoni number are presented in Tab. 5.2. The dynamic viscosities of 0.25 mg/ ml rGO-PEG nanofluid were measured using a Stabinger Viscometer (incertitude ± 5 %) at five different temperatures. Fig. 5.11 shows that the dynamic viscosity of water and rGO-PEG nanofluid both decrease with increasing temperature, but the graphene nanofluid has a higher viscosity at each temperature. Moreover, this percentage enhancement of dynamic viscosity with the addition of rGO-PEG nanoparticles increases with temperature. The heat capacity for graphene nanofluid with PEG was measured by differential scanning calorimetry (incertitude ± 1 %) under 10 bar of nitrogen. In Tab. 5.2, the heat capacities of rGO-PEG nanofluid at different temperatures are very similar to those of water because of the very

low nanoparticle concentration. The thermal conductivities of rGO-PEG nanofluid were calculated by applying the model of Leong et al. [172] (which includes the effect of the interfacial layer):

$$k_{eff} = ((k_p - k_{lr})\phi_p k_{lr}[2\beta_l^3 - \beta^3 + 1] + (k_p + 2k_{lr}) \times \beta_l^3[\phi_p \beta^3 (k_{lr} - k_f) + k_f])(\beta_l^3 (k_p + 2k_{lr}) - (k_p - k_{lr})\phi_p[\beta_l^3 + \beta^3 - 1])^{-1} \quad (5.3)$$

In this expression, $1 + h/a = \beta$ and $1 + h/2a = \beta_l$, where h is the interfacial layer thickness and a is the particle radius. The particle volume fraction is ϕ_p; k_p, k_f, and k_{lr} are the thermal conductivities of the particles and the liquid and interfacial layers, respectively. The calculated thermal conductivities using Eq. 5.3 are given in Tab. 5.2; the thermal conductivity of graphene nanofluid is significantly enhanced in comparison to the base fluid. These calculated results are consistent with other reports [163-166], claiming that a considerable thermal conductivity enhancement can be achieved in water-based graphene nanofluid with a very low volume fraction.

Temperature T_s (°C)	Dynamic viscosity μ (mPa·s)		Volumetric heat capacity $C_{p,v}$ (J·cm^{-3}·K^{-1})		Thermal conductivity k (W·m^{-1}·K^{-1})	
	Water	rGO-PEG	Water	rGO-PEG	Water	rGO-PEG
22	1.002	1.08	4.174	4.19	0.5984	1.7961
50	0.547	0.65	4.131	4.13	0.6435	1.9314
66	0.429	0.52	4.103	4.10	0.6596	1.9797
84	0.339	0.39	4.071	4.07	0.6721	2.0173
106	0.270	0.34	4.032	4.03	0.6801	2.0414

Table 5.2 Physical and thermal properties of (i) water and (ii) rGO-PEG nanofluid (0.25 mg/ml), at specified temperatures.

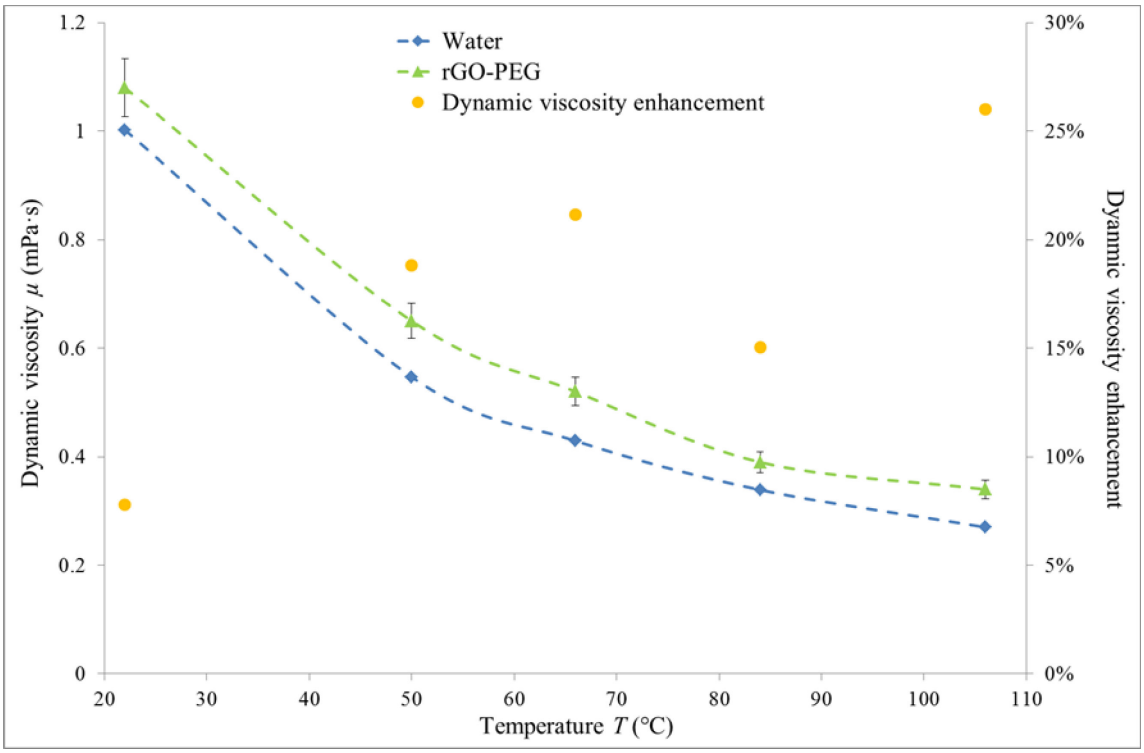

Figure 5.11 Dynamic viscosity as a function of temperature, for pure water and 0.25 mg/ml rGO-PEG nanofluid. The enhancement by addition of nanoparticles is shown (right-hand axis).

The surface tension of rGO-PEG nanofluid was measured at different temperatures by the pendant drop method with Kruss® DSA. The pendant drop method is based on the Young-Laplace equation which describes the relationship between the drop shape and the interfacial tension. The surface tension is calculated from the shadow image of a drop suspended from a needle by drop shape analysis. Fig. 5.12 shows the measurement results for water and rGO-PEG nanofluid. As common liquids, the surface tensions of both liquids decrease almost linearly with the increase of temperature. However, the addition of rGO-PEG nanoparticles reduces the surface tension and the evolution for rGO-PEG nanofluid has a steeper slope than for water which is also observed in the study of

Ahammed et al. [173]. Owing to the hydrophilic nature of rGO-PEG nanoparticle, the strong attraction force adsorbs water molecules to create an interlayer on solid surface and the intermolecular space of water molecules between each interlayer increases. Therefore, on the free surface of droplet, the attraction force from water molecules in bulk is weakened which is perceived as a decline in surface tension. The surface tension of water from the international tables [174] is added to examine the measurement accuracy. From Fig. 5.12, it is clearly observed that the measured surface tension of water agrees well with the theoretical data with a maximum deviation of ± 2.8%.

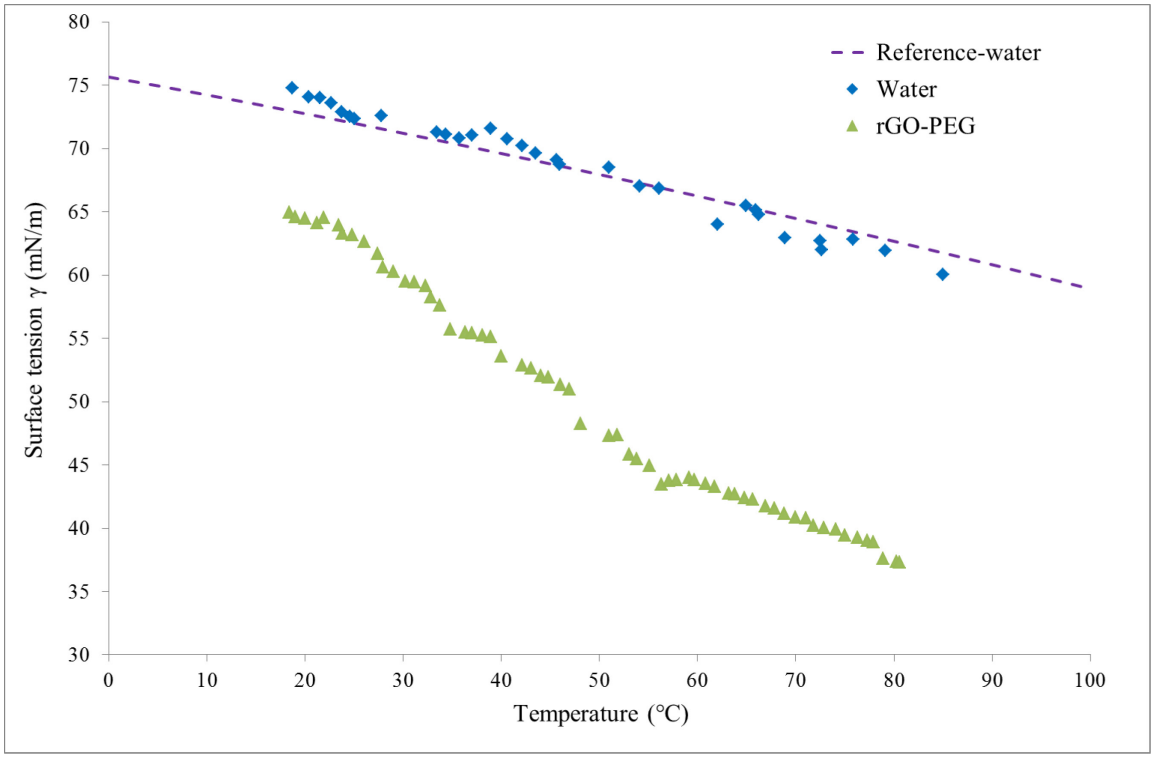

Figure 5.12 Relation of surface tension and temperature for pure water and 0.25 mg/ml rGO-PEG nanofluid. The purple dashed line represents data from international tables.

The temperature difference across the droplet surface was applied to calculate (using Eq. 5.2) the thermal Marangoni numbers of water and rGO-PEG nanofluid throughout evaporation. The case at substrate temperature of 84 °C is presented in Fig. 5.13. The evolutions of thermal Marangoni number for both liquids have the same trend as temperature difference: for rGO-PEG nanofluid, a sharp reduction is observed which lasts only a few seconds at the beginning and then the thermal Marangoni number decreases almost linearly since the evaporation of droplet reaches the steady state (when the temperature difference begins to decrease with a constant rate); for pure water, the thermal Marangoni number stays constant when the evaporation process starts and then undergoes a rapid decrease after 10 s which is more intense than for rGO-PEG nanofluid. The initial Marangoni number for rGO-PEG nanofluid droplet is considerably high, but its duration is too short that the Marangoni effect cannot generate visible convection cells. On the other side, the thermal Marangoni number for water droplet keeps a relative long period of high value at which the Marangoni effect induces thermal convection and improves the evaporation performance.

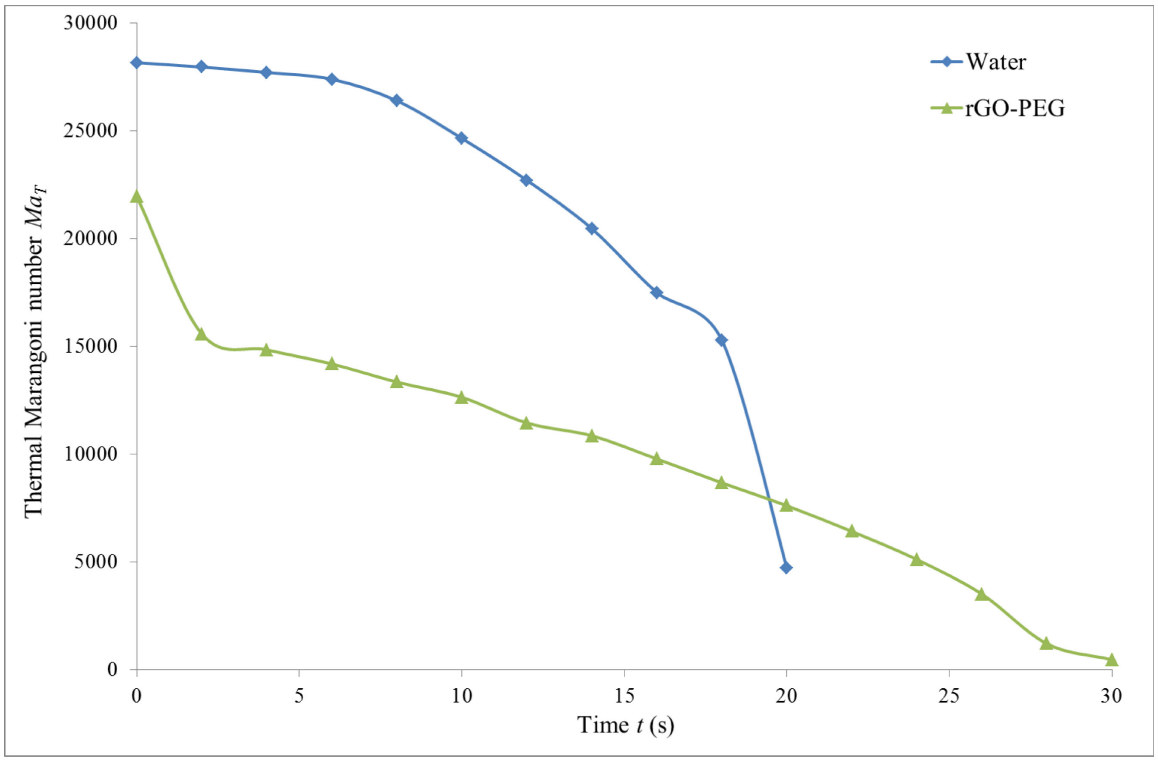

Figure 5.13 Evolution of thermal Marangoni number as a function of time, for pure water and 0.25 mg/ml rGO-PEG nanofluid at substrate temperatures of 84 °C.

The comparison of thermal Marangoni numbers for water and rGO-PEG nanofluid at five different substrate temperatures is shown in Fig. 5.14. The initial thermal Marangoni number is taken for water while the value in steady state, when the decrease rate of thermal Marangoni number is constant, is taken for rGO-PEG nanofluid. As common liquids, the thermal Marangoni number of both increases as the substrate temperature rises. However, while the thermal Marangoni number for rGO-PEG nanofluid increases nearly linearly with substrate temperature, beyond 66 °C it increases more rapidly for water as convection cells appear. Furthermore, even at the maximum substrate temperature used (106 °C), the thermal Marangoni number of rGO-PEG nanofluid is lower than that of water at 66 °C. As a result, the thermal Marangoni number of a water

droplet at 66 °C (around 20000) is considered as the threshold beyond which the evaporation rate will be significantly improved by the appearance of convection cells.

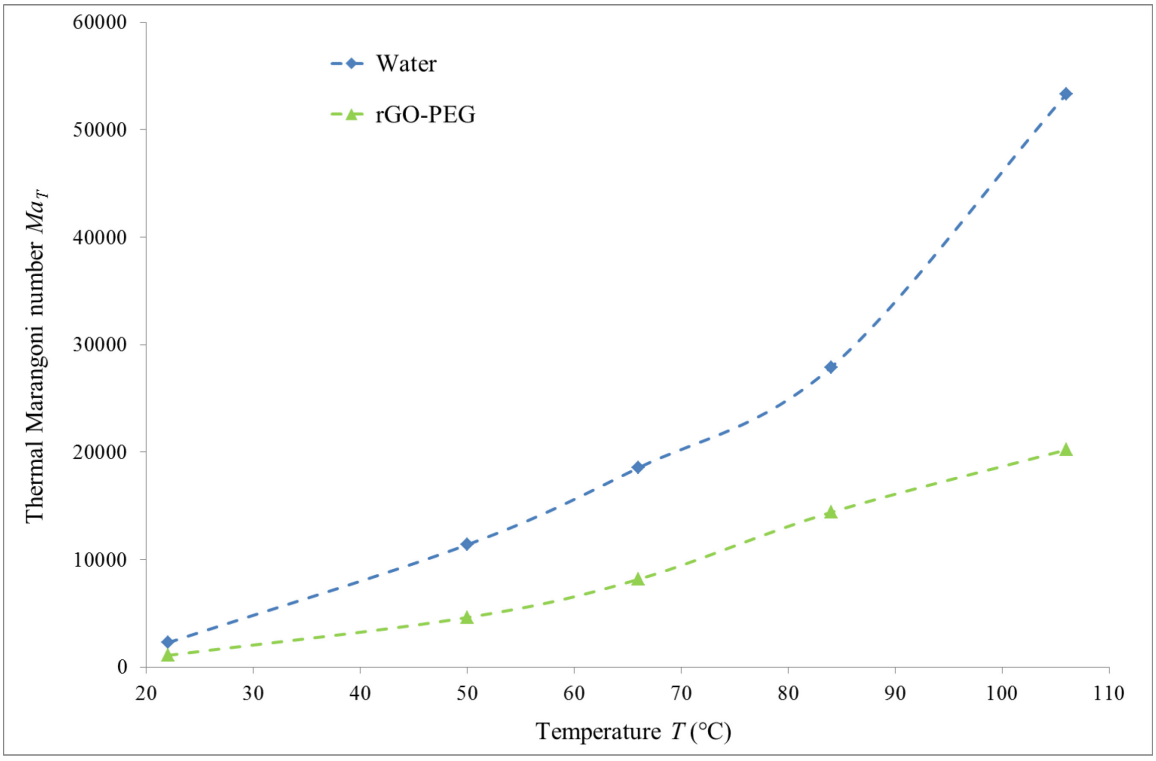

Figure 5.14 Dependence of the thermal Marangoni number on substrate temperature, for pure water and 0.25 mg/ml rGO-PEG nanofluid.

In order to investigate the correlation between the thermal Marangoni flow and the droplet evaporation rate, Fig. 5.15 shows their relation for droplets of water and for rGO-PEG nanofluid. The evaporation rate of both liquids increases with increasing thermal Marangoni number, but different modes are suggested by the curves. The evaporation rate of the rGO-PEG nanofluid grows exponentially, while the water shows two different growth regimes: when the thermal Marangoni number exceeds the threshold of 20000, the evaporation rate increases more rapidly. Moreover, the growth rate of evaporation for

the rGO-PEG nanofluid is noticeably higher than that of water, which indicates that with the same thermal Marangoni number, the rGO-PEG nanofluid can provide a significantly improved evaporation performance in comparison to water. This suggests a possible method to enhance the evaporation rate of graphene nanofluid further, by increasing the thermal Marangoni number so as to generate convective flows.

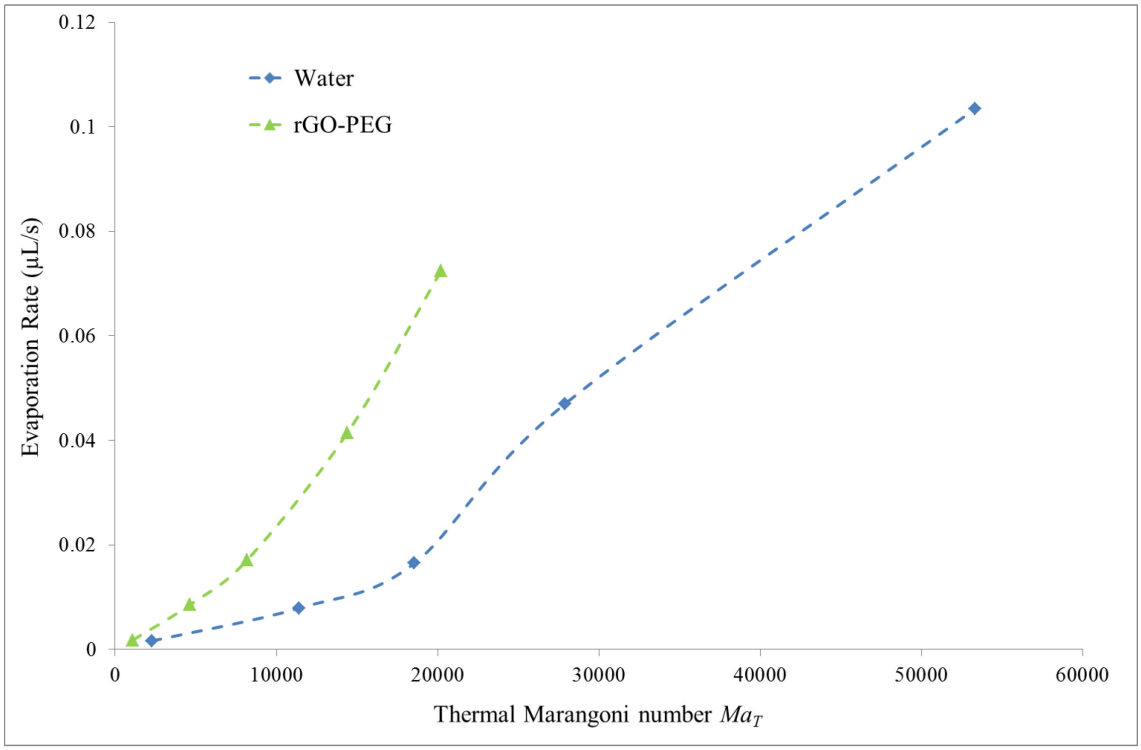

Figure 5.15 Relation between evaporation rate and thermal Marangoni number, for pure water and 0.25 mg/ml rGO-PEG nanofluid.

5.5 Conclusions

The evaporation behavior of droplets of pure water and three different water-based graphene nanofluids was investigated; it is confirmed that graphene oxide functionalization with polyethylene glycol (PEG) promotes the dispersion of graphene

nanoparticles and increases the evaporation rate. Preparation without PEG-functionalization, or with an increased nanoparticle concentration, decreases the evaporation rate; the poor dispersion of graphene nanoparticles and their agglomeration are the main causes, indicated by analysis of the nanoparticle depositions and the microscopic videos, respectively.

Heating of the substrate can greatly enhance the droplet evaporation rate of water and graphene nanofluids (GO and rGO-PEG). The poor dispersion of GO nanoparticles leads to reduced heat transfer efficiency and a lower evaporation rate, in comparison to water and rGO-PEG nanofluid. Because of better heat transfer efficiency, the droplet of rGO-PEG nanofluid exhibits a higher evaporation rate than water at ambient temperature. The enhancement of evaporation rate in our study is at maximum at ambient temperature and then decreases with further increase of substrate temperature, to the extent that at a substrate temperature of 106 °C, the water droplet evaporates much faster than the rGO-PEG nanofluid. From infrared videos, convection cells appear on the surface of water droplets at the higher substrate temperatures, while thermal instability is not detected on the droplet surface of rGO-PEG nanofluid. Convective flows increase the evaporation of water droplets, and only results from the thermal Marangoni effect in small droplets of single-component. The thermal Marangoni number, which characterizes the thermal Marangoni effect, is always under the threshold of convective flow for droplets of rGO-PEG nanofluid. The increase in the dynamic viscosity from the addition of rGO-PEG nanoparticles to the base fluid is believed to be the main reason that the heat convection is inhibited. The application of graphene nanofluid to enhance the evaporation rate is more effective at low substrate temperature. The correlation seen between evaporation

rate and the thermal Marangoni number can provide guidance in future work to improve droplet evaporation performance.

Chapter 6
Conclusions and future work

Over past decades, high efficiency heat dissipation is more and more imperatively required in areas of micro-electronics, spacecraft, and nuclear reactors, which encourages the development of next generation heat exchanger. Heat pipe is one of potential effective cooling equipments with advantages of passive operation, long life, minimum maintenance, flexible size and effective thermal conductivity. Binary solution and nanofluid are considered as prospective working fluid to significantly improve thermal performance of heat pipe by Marangoni effect and exceptional thermal conductivity, respectively. Most of mass and heat transfer take place at micro-region near triple phase (solid, liquid, vapor) contact line of working fluid, which is essential to working efficiency enhancement of heat pipe. Therefore this study was focused on the evaporation process of sessile droplets of these two novel working fluids which possess similar micro-region to that in heat pipe. Various techniques were employed to investigate evaporation behavior of sessile droplets. The acoustic high frequency echography technique was first time used to track alcohol concentration in alcohol-water binary mixture droplet at solid/liquid interface. The infrared thermography was used to investigate temperature distribution and convective flow on liquid/vapor interface of droplets. The Drop Shape Analyzer (DSA) was used to unveil the shape variation of evaporating droplets in the form of contact angle, contact diameter and volume. The microscopic technique was used to observe the kinetics of nanoparticles within droplets and the deposition patterns left by drying. Additionally, UV/Vis spectrum technique,

Raman spectroscopy, and X-ray photoelectron spectroscopy were devoted to the characterizations of nanofluid.

For binary solutions, different diffusion coefficient in the air leads to different alcohol/water ratio at droplet free surface between 1-butanol and ethanol aqueous solutions during evaporation under ambient condition. The infrared camera detects the existence of alcohol by visible convection cells at liquid/vapor interface while the acoustic echography measures reflection coefficient at solid/liquid interface. Due to high volatility, the ratio of ethanol/water stays at very low level on droplet surface and most of ethanol molecules are situated in the bulk of droplet, which results in a large disparity of alcohol exhaustion time estimation between infrared and acoustic methods. Nevertheless, the coincidence of 1-butanol depletion time estimations confirms the feasibility of acoustic method to monitor 1-butanol concentration kinetics as a function of time. Furthermore, hygroscopic power difference between pure 1-butanol and ethanol was also confirmed with the aid of infrared thermography and acoustic echography. When deposited on heated substrate, the pure 1-butanol droplet does not show any thermal instability at different substrate temperatures while the co-existence of thermal and solutal Marangoni flows was observed for 1-butanol-water mixture droplet at substrate temperature of above 50 °C. Thermal Marangoni flows appear on the surface of pure water droplet when substrate temperature exceeds 50 °C. By comparing with pure 1-butanol and water droplets, the evaporation rate of 1-butanol aqueous solution droplet is enhanced by the contribution of solutal Marangoni effect which is induced by inhomogeneous distribution of 1-butanol concentration at liquid/vapor interface. By analyzing the relationship between the experimental data and prediction of Hu and

Larson model as a function of thermal Marangoni number, a series of empirical equations was developed to calculate overall and initial time evaporation rate of pure water droplet at different substrate temperature. And then by including solutal Marangoni effect, the empirical equations were derived to calculate evaporation rate before depletion time and at initial time for 1-butanol-water binary droplet which are based on precedent equations. The results of these equations correspond fairly well to the experimental data at different substrate temperature.

For nanofluid, the effects of PEG-functionalization and nanoparticle concentration on suspension stability and evaporation behavior were investigated at ambient condition. The PEGylation treatment was proved to not only improve graphene nanoparticle dispersion but also enhance evaporation performance by the comparison of deposition pattern and overall evaporation rate between 0.25 mg/ml graphene oxide (GO), 0.25 mg/ml and 0.8 mg/ml PEGylated reduced graphene oxide (rGO-PEG) nanofluids. Non-PEGylating or inappropriate concentration will deteriorate nanoparticle dispersion homogeneity and then evaporation performance due to large nanoparticle agglomerations. The effect of substrate temperature was investigated during evaporation process of pure water and 0.25 mg/ml rGO-PEG nanofluid droplets at five substrate temperatures (22, 50, 66, 84, 106 °C). Evaporation rates of both liquids increase with the rise of substrate temperature. Owing to reported exceptional thermal conductivity, rGO-PEG nanofluid evaporates faster than pure water at ambient temperature. However, this heat transfer enhancement by adding graphene nanoparticles decreases with further substrate heating. When temperature goes above 66 °C, water droplet reveals dramatically higher evaporation rate than that for rGO-PEG nanofluid. This theatrical transformation is

attributable to thermal Marangoni effect on water droplet evaporation, which is presented in the form of convection cells under infrared camera. The addition of rGO-PEG nanoparticles increases dynamic viscosity, which is considered to be responsible for the suppression of heat convection within nanofluid droplet.

Despite findings from this study, the mass and heat transfer mechanisms of binary solution and the controversial thermal performance of nanofluid necessitate a large scope of future researches. The acoustic high frequency echography is demonstrated to precisely monitor alcohol concentration at solid/liquid interface and thus the application can be extended to track overall not local alcohol concentration variation or to reveal nanoparticle deposition rate on substrate within evaporating nanofluid droplet which is beneficial to DNA mapping and inkjet printing. More factors such as alcohol concentration, surface properties of substrate, drop profile etc. need to be added in the equation for predicting evaporation rate of low volatile alcohol aqueous droplet, which lacks experimental data. Besides, the study on dynamic equilibrium of ethanol condensation and evaporation at liquid/vapor interface can contribute to the evaporation rate prediction for ethanol-water mixture droplet. The application of rGO-PEG nanofluid to improve heat transfer is more effective at low substrate temperature. Thus, the method for reducing dynamic viscosity is expected to considerably enhancement thermal performance of rGO-PEG nanofluid and to widely extend application range.

Reference

[1] Joule, J. P. (1861). On the surface-condensation of steam. *Philosophical transactions of the Royal Society of London, 151*, 133-160.

[2] Bergles, A. E. (1998). Techniques to enhance heat transfer. *Handbook of heat transfer, 3*, 11-1.

[3] Figure from http://www.aavid.com/product-group/heatpipe/operate

[4] Ranjan, R., Patel, A., Garimella, S. V., & Murthy, J. Y. (2012). Wicking and thermal characteristics of micropillared structures for use in passive heat spreaders. *International Journal of Heat and Mass Transfer, 55*(4), 586-596.

[5] Harmand, S., Sefiane, K., Lancial, N., & Benselama, A. M. (2011). Experimental and theoretical investigation of the evaporation and stability of a meniscus in a flat micro-channel. *International Journal of Thermal Sciences, 50*(10), 1845-1852.

[6] Wang, H., Garimella, S. V., & Murthy, J. Y. (2007). Characteristics of an evaporating thin film in a microchannel. *International journal of heat and mass transfer, 50*(19), 3933-3942.

[7] Potash, M., & Wayner, P. C. (1972). Evaporation from a two-dimensional extended meniscus. *International Journal of Heat and Mass Transfer, 15*(10), 1851-1863.

[8] Wayner, P. C. (1999). Intermolecular forces in phase-change heat transfer: 1998 Kern award review. *AIChE journal, 45*(10), 2055-2068.

[9] Ranjan, R., Garimella, S. V., Murthy, J. Y., & Yazawa, K. (2011). Assessment of nanostructured capillary wicks for passive two-phase heat transport. *Nanoscale and microscale thermophysical engineering, 15*(3), 179-194.

[10] Young, T. (1805). An essay on the cohesion of fluids. *Philosophical Transactions of the Royal Society of London, 95*, 65-87.

[11] Contact Angle 2017 Wikipedia. https://en.wikipedia.org/w/index.php?title=Contact_angle&oldid=809158542, accessed November 24, 2017.

[12] Sefiane, K., Tadrist, L., & Douglas, M. (2003). Experimental study of evaporating water–ethanol mixture sessile drop: influence of concentration. *International journal of heat and mass transfer, 46*(23), 4527-4534.

[13] Christy, J. R., Hamamoto, Y., & Sefiane, K. (2011). Flow transition within an evaporating binary mixture sessile drop. *Physical review letters, 106*(20), 205701.

[14] Marangoni, C. (1865). Sull'espansione delle goccie d'un liquido galleggianti sulla superfice di altro liquido.

[15] Hendarto, E., & Gianchandani, Y. B. (2013). Size sorting of floating spheres based on Marangoni forces in evaporating droplets. *Journal of Micromechanics and Microengineering, 23*(7), 075016.

[16] Hu, H., & Larson, R. G. (2006). Marangoni effect reverses coffee-ring depositions. *The Journal of Physical Chemistry B, 110*(14), 7090-7094.

[17] Majumder, M., Rendall, C. S., Eukel, J. A., Wang, J. Y., Behabtu, N., Pint, C. L., ... & Barron, A. R. (2012). Overcoming the "coffee-stain" effect by compositional Marangoni-flow-assisted drop-drying. *The Journal of Physical Chemistry B, 116*(22), 6536-6542.

[18] Nikolov, A. D., Wasan, D. T., Chengara, A., Koczo, K., Policello, G. A., & Kolossvary, I. (2002). Superspreading driven by Marangoni flow. *Advances in colloid and interface science, 96*(1), 325-338.

[19] Savino, R., & Fico, S. (2004). Transient Marangoni convection in hanging evaporating drops. *Physics of Fluids, 16*(10), 3738-3754.

[20] Buffone, C., & Sefiane, K. (2004). Investigation of thermocapillary convective patterns and their role in the enhancement of evaporation from pores. *International Journal of Multiphase Flow, 30*(9), 1071-1091.

[21] Vochten, R., & Petre, G. (1973). Experimental determination of the heat of reversible absorption of some alcohols. *Journal of Colloid and Interface Science, 42*, 320-327.

[22] Ono, N., Kaneko, T., Nishiguchi, S., & Shoji, M. (2009). Measurement of temperature dependence of surface tension of alcohol aqueous solutions by maximum bubble pressure method. *Journal of Thermal Science and Technology, 4*(2), 284-293.

[23] Ouenzerfi, S., & Harmand, S. (2016). Experimental droplet study of inverted marangoni effect of a binary liquid mixture on a nonuniform heated substrate. *Langmuir, 32*(10), 2378-2388.

[24] Di Francescantonio, N., Savino, R., & Abe, Y. (2008). New alcohol solutions for heat pipes: Marangoni effect and heat transfer enhancement. *International Journal of Heat and Mass Transfer, 51*(25), 6199-6207.

[25] Hu, Y., Liu, T., Li, X., & Wang, S. (2014). Heat transfer enhancement of micro oscillating heat pipes with self-rewetting fluid. *International Journal of Heat and Mass Transfer, 70*, 496-503.

[26] Savino, R., Piccolo, C., Fortezza, R., & Abe, Y. (2007). Heat pipes with self-rewetting fluids under low-gravity conditions. *Microgravity Science and Technology, 19*(3-4), 75-77.

[27] Choi, S. U., & Eastman, J. A. (1995). Enhancing thermal conductivity of fluids with nanoparticles (No. ANL/MSD/CP--84938; CONF-951135--29). *Argonne National Lab., IL (United States)*.

[28] Sivashanmugam, P. (2012). Application of nanofluids in heat transfer. *In An Overview of Heat Transfer Phenomena. InTech*.

[29] Yatsuya, S., Mihama, K., & Uyeda, R. (1974). A New Technique for the Preparation of Extremely Fine Metal Particles. *Japanese Journal of Applied Physics, 13*(4), 749.

[30] Wagener, M., Murty, B. S., & Günther, B. (1996). Preparation of metal nanosuspensions by high-pressure DC-sputtering on running liquids. *MRS Online Proceedings Library Archive*, 457.

[31] Eastman, J. A., Choi, U. S., Li, S., Thompson, L. J., & Lee, S. (1996). Enhanced thermal conductivity through the development of nanofluids. *MRS Online Proceedings Library Archive*, 457.

[32] Zhu, H. T., Lin, Y. S., & Yin, Y. S. (2004). A novel one-step chemical method for preparation of copper nanofluids. *Journal of colloid and interface science, 277*(1), 100-103.

[33] Lo, C. H., Tsung, T. T., & Chen, L. C. (2005). Shape-controlled synthesis of Cu-based nanofluid using submerged arc nanoparticle synthesis system (SANSS). *Journal of Crystal Growth, 277*(1), 636-642.

[34] Phuoc, T. X., Soong, Y., & Chyu, M. K. (2007). Synthesis of Ag-deionized water nanofluids using multi-beam laser ablation in liquids. *Optics and lasers in engineering, 45*(12), 1099-1106.

[35] Kim, H. J., Bang, I. C., & Onoe, J. (2009). Characteristic stability of bare Au-water nanofluids fabricated by pulsed laser ablation in liquids. *Optics and Lasers in Engineering, 47*(5), 532-538.

[36] Kole, M., & Dey, T. K. (2013). Thermal performance of screen mesh wick heat pipes using water-based copper nanofluids. *Applied Thermal Engineering, 50*(1), 763-770.

[37] Li, Q., Xuan, Y., & Wang, J. (2005). Experimental investigations on transport properties of magnetic fluids. *Experimental Thermal and Fluid Science, 30*(2), 109-116.

[38] Beck, M. P., Sun, T., & Teja, A. S. (2007). The thermal conductivity of alumina nanoparticles dispersed in ethylene glycol. *Fluid Phase Equilibria, 260*(2), 275-278.

[39] Longo, G. A., & Zilio, C. (2011). Experimental measurement of thermophysical properties of oxide–water nano-fluids down to ice-point. *Experimental Thermal and Fluid Science, 35*(7), 1313-1324.

[40] Kannadasan, N., Ramanathan, K., & Suresh, S. (2012). Comparison of heat transfer and pressure drop in horizontal and vertical helically coiled heat exchanger with CuO/water based nano fluids. *Experimental Thermal and Fluid Science, 42*, 64-70.

[41] Kole, M., & Dey, T. K. (2012). Thermophysical and pool boiling characteristics of ZnO-ethylene glycol nanofluids. *International Journal of Thermal Sciences, 62*, 61-70.

[42] Kim, N. J., Park, S. S., Lim, S. H., & Chun, W. (2011). A study on the characteristics of carbon nanofluids at the room temperature (25° C). *International Communications in Heat and Mass Transfer, 38*(3), 313-318.

[43] Meng, Z., Wu, D., Wang, L., Zhu, H., & Li, Q. (2012). Carbon nanotube glycol nanofluids: photo-thermal properties, thermal conductivities and rheological behavior. *Particuology, 10*(5), 614-618.

[44] Hajjar, Z., morad Rashidi, A., & Ghozatloo, A. (2014). Enhanced thermal conductivities of graphene oxide nanofluids. *International Communications in Heat and Mass Transfer, 57*, 128-131.

[45] Mehrali, M., Sadeghinezhad, E., Rosen, M. A., Akhiani, A. R., Latibari, S. T., Mehrali, M., & Metselaar, H. S. C. (2016). Experimental investigation of thermophysical properties, entropy generation and convective heat transfer for a nitrogen-doped graphene nanofluid in a laminar flow regime. *Advanced Powder Technology, 27*(2), 717-727.

[46] Yu, W., Xie, H., Chen, L., & Li, Y. (2009). Investigation of thermal conductivity and viscosity of ethylene glycol based ZnO nanofluid. *Thermochimica Acta, 491*(1), 92-96.

[47] Moosavi, M., Goharshadi, E. K., & Youssefi, A. (2010). Fabrication, characterization, and measurement of some physicochemical properties of ZnO nanofluids. *International journal of heat and fluid flow, 31*(4), 599-605.

[48] Bobbo, S., Fedele, L., Benetti, A., Colla, L., Fabrizio, M., Pagura, C., & Barison, S. (2012). Viscosity of water based SWCNH and TiO 2 nanofluids. *Experimental Thermal and Fluid Science, 36*, 65-71.

[49] Lamas, B., Abreu, B., Fonseca, A., Martins, N., & Oliveira, M. (2012). Assessing colloidal stability of long term MWCNT based nanofluids. *Journal of colloid and interface science, 381*(1), 17-23.

[50] Liu, Y. D., Zhou, Y. G., Tong, M. W., & Zhou, X. S. (2009). Experimental study of thermal conductivity and phase change performance of nanofluids PCMs. *Microfluidics and Nanofluidics, 7*(4), 579.

[51] Wu, S., Zhu, D., Zhang, X., & Huang, J. (2010). Preparation and melting/freezing characteristics of Cu/paraffin nanofluid as phase-change material (PCM). *Energy & fuels, 24*(3), 1894-1898.

[52] Wu, S., Wang, H., Xiao, S., & Zhu, D. (2012). Numerical simulation on thermal energy storage behavior of Cu/paraffin nanofluids PCMs. *Procedia Engineering, 31*, 240-244.

[53] Otanicar, T. P., Phelan, P. E., Prasher, R. S., Rosengarten, G., & Taylor, R. A. (2010). Nanofluid-based direct absorption solar collector. *Journal of renewable and sustainable energy, 2*(3), 033102.

[54] Shin, D., & Banerjee, D. (2011). Enhancement of specific heat capacity of high-temperature silica-nanofluids synthesized in alkali chloride salt eutectics for solar thermal-energy storage applications. *International journal of heat and mass transfer, 54*(5), 1064-1070.

[55] Taylor, R. A., Phelan, P. E., Otanicar, T. P., Walker, C. A., Nguyen, M., Trimble, S., & Prasher, R. (2011). Applicability of nanofluids in high flux solar collectors. *Journal of Renewable and Sustainable Energy, 3*(2), 023104.

[56] Gnanadason, M. K., Kumar, P. S., Jemilda, G., & Jasper, S. S. (2012). Effect of nanofluids in a modified vacuum single basin solar still. *International Journal of Scientific and Engineering Research, 3*, 2229-5518.

[57] Kim, J. K., Jung, J. Y., & Kang, Y. T. (2006). The effect of nano-particles on the bubble absorption performance in a binary nanofluid. *International Journal of Refrigeration, 29*(1), 22-29.

[58] Kim, J. K., Jung, J. Y., & Kang, Y. T. (2007). Absorption performance enhancement by nano-particles and chemical surfactants in binary nanofluids. *International Journal of Refrigeration, 30*(1), 50-57.

[59] Ma, X., Su, F., Chen, J., & Zhang, Y. (2007). Heat and mass transfer enhancement of the bubble absorption for a binary nanofluid. *Journal of Mechanical Science and Technology, 21*(11), 1813.

[60] Ma, X., Su, F., Chen, J., Bai, T., & Han, Z. (2009). Enhancement of bubble absorption process using a CNTs-ammonia binary nanofluid. *International Communications in Heat and Mass Transfer, 36*(7), 657-660.

[61] Zhou, J., Wu, Z., Zhang, Z., Liu, W., & Xue, Q. (2000). Tribological behavior and lubricating mechanism of Cu nanoparticles in oil. *Tribology Letters, 8*(4), 213-218.

[62] Shen, B., Shih, A., & Tung, S. (2007, January). Application of nanofluids in minimum quantity lubrication grinding. *In ASME/STLE 2007 International Joint Tribology Conference (pp. 725-731)*. American Society of Mechanical Engineers.

[63] Yu, H. L., Yi, X. U., Shi, P. J., Xu, B. S., Wang, X. L., & Qian, L. I. U. (2008). Tribological properties and lubricating mechanisms of Cu nanoparticles in lubricant. *Transactions of Nonferrous Metals Society of China, 18*(3), 636-641.

[64] Yu, B., Liu, Z., Zhou, F., Liu, W., & Liang, Y. (2008). A novel lubricant additive based on carbon nanotubes for ionic liquids. *Materials Letters, 62*(17), 2967-2969.

[65] Kim, Y. S., Nakatsuka, K., Fujita, T., & Atarashi, T. (1999). Application of hydrophilic magnetic fluid to oil seal. *Journal of Magnetism and Magnetic Materials, 201*(1), 361-363.

[66] Kim, Y. S., & Kim, Y. H. (2003). Application of ferro-cobalt magnetic fluid for oil sealing. *Journal of Magnetism and Magnetic Materials, 267*(1), 105-110.

[67] Mitamura, Y., Arioka, S., Sakota, D., Sekine, K., & Azegami, M. (2008). Application of a magnetic fluid seal to rotary blood pumps. *Journal of Physics: Condensed Matter, 20*(20), 204145.

[68] Zhang, L., Jiang, Y., Ding, Y., Povey, M., & York, D. (2007). Investigation into the antibacterial behaviour of suspensions of ZnO nanoparticles (ZnO nanofluids). *Journal of Nanoparticle Research, 9*(3), 479-489.

[69] Jones, N., Ray, B., Ranjit, K. T., & Manna, A. C. (2008). Antibacterial activity of ZnO nanoparticle suspensions on a broad spectrum of microorganisms. *FEMS Microbiology Letters, 279*(1), 71-76.

[70] Liu, Y., He, L., Mustapha, A., Li, H., Hu, Z. Q., & Lin, M. (2009). Antibacterial activities of zinc oxide nanoparticles against Escherichia coli O157: H7. *Journal of Applied Microbiology, 107*(4), 1193-1201.

[71] Ghosh, P., Han, G., De, M., Kim, C. K., & Rotello, V. M. (2008). Gold nanoparticles in delivery applications. *Advanced drug delivery reviews, 60*(11), 1307-1315.

[72] Singh, R., & Lillard, J. W. (2009). Nanoparticle-based targeted drug delivery. *Experimental and molecular pathology, 86*(3), 215-223.

[73] Tripisciano, C., Kraemer, K., Taylor, A., & Borowiak-Palen, E. (2009). Single-wall carbon nanotubes based anticancer drug delivery system. *Chemical Physics Letters, 478*(4), 200-205.

[74] Philip, J., Jaykumar, T., Kalyanasundaram, P., & Raj, B. (2003). A tunable optical filter. *Measurement Science and Technology, 14*(8), 1289.

[75] Mishra, A., Tripathy, P., Ram, S., & Fecht, H. J. (2009). Optical properties in nanofluids of gold nanoparticles in poly (vinylpyrrolidone). *Journal of Nanoscience and Nanotechnology, 9*(7), 4342-4347.

[76] Nguyen, C. T., Roy, G., Galanis, N., & Suiro, S. (2006). Heat Transfer Enhancement by Using Al203-Water Nanofluid in a Liquid Cooling System for Microprocessors. *WSEAS Transactions on Heat and Mass Transfer, 1*(3), 370.

[77] Ma, H. B., Wilson, C., Borgmeyer, B., Park, K., Yu, Q., Choi, S. U. S., & Tirumala, M. (2006). Effect of nanofluid on the heat transport capability in an oscillating heat pipe. *Applied Physics Letters, 88*(14), 143116.

[78] Shokouhmand, H., Ghazvini, M., & Shabanian, J. (2008). Performance analysis of using nanofluids in microchannel heat sink in different flow regimes and its simulation using artificial neural network. *In Proceedings of the World Congress on Engineering (WCE ' 08) (Vol. 3)*.

[79] Kao, M. J., Ting, C. C., Lin, B. F., & Tsung, T. T. (2007). Aqueous aluminum nanofluid combustion in diesel fuel. *Journal of Testing and Evaluation, 36*(2), 186-190.

[80] Gan, Y., Lim, Y. S., & Qiao, L. (2012). Combustion of nanofluid fuels with the addition of boron and iron particles at dilute and dense concentrations. *Combustion and Flame, 159*(4), 1732-1740.

[81] Sabet Sarvestany, N., Farzad, A., Ebrahimnia-Bajestan, E., & Mir, M. (2014). Effects of magnetic nanofluid fuel combustion on the performance and emission characteristics. *Journal of Dispersion Science and Technology, 35*(12), 1745-1750.

[82] Shaafi, T., & Velraj, R. (2015). Influence of alumina nanoparticles, ethanol and isopropanol blend as additive with diesel–soybean biodiesel blend fuel: combustion, engine performance and emissions. *Renewable Energy, 80*, 655-663.

[83] Wen, D., & Ding, Y. (2005). Experimental investigation into the pool boiling heat transfer of aqueous based γ-alumina nanofluids. *Journal of Nanoparticle Research, 7*(2), 265-274.

[84] Liu, Z. H., Xiong, J. G., & Bao, R. (2007). Boiling heat transfer characteristics of nanofluids in a flat heat pipe evaporator with micro-grooved heating surface. *International Journal of Multiphase Flow, 33*(12), 1284-1295.

[85] Kim, H., & Kim, M. (2009). Experimental study of the characteristics and mechanism of pool boiling CHF enhancement using nanofluids. *Heat and Mass Transfer, 45*(7), 991-998.

[86] Han, Z. H., Cao, F. Y., & Yang, B. (2008). Synthesis and thermal characterization of phase-changeable indium/polyalphaolefin nanofluids. *Applied Physics Letters, 92*(24), 243104.

[87] Nelson, I. C., Banerjee, D., & Ponnappan, R. (2009). Flow loop experiments using polyalphaolefin nanofluids. *Journal of Thermophysics and Heat Transfer, 23*(4), 752.

[88] Buongiorno, J., Hu, L. W., Kim, S. J., Hannink, R., Truong, B. A. O., & Forrest, E. (2008). Nanofluids for enhanced economics and safety of nuclear reactors: an evaluation of the potential features, issues, and research gaps. *Nuclear Technology, 162*(1), 80-91.

[89] Hadad, K., Rahimian, A., & Nematollahi, M. R. (2013). Numerical study of single and two-phase models of water/Al_2O_3 nanofluid turbulent forced convection flow in VVER-1000 nuclear reactor. *Annals of Nuclear Energy, 60*, 287-294.

[90] Sharma, D., & Pandey, K. M. (2016). Numerical investigation of heat transfer characteristics in triangular channel in light water nuclear reactor by using CuO-water based nanofluids. *Indian Journal of Science and Technology, 9*(16).

[91] Park, K. J., & Jung, D. (2007). Boiling heat transfer enhancement with carbon nanotubes for refrigerants used in building air-conditioning. *Energy and Buildings, 39*(9), 1061-1064.

[92] Kulkarni, D. P., Das, D. K., & Vajjha, R. S. (2009). Application of nanofluids in heating buildings and reducing pollution. *Applied Energy, 86*(12), 2566-2573.

[93] Chen, P., Toubal, M., Carlier, J., Harmand, S., Nongaillard, B., & Bigerelle, M. (2016). Evaporation of binary sessile drops: infrared and acoustic methods to track alcohol concentration at the interface and on the surface. *Langmuir, 32*(38), 9836-9845.

[94] Deegan, R. D., Bakajin, O., Dupont, T. F., Huber, G., Nagel, S. R., & Witten, T. A. (2000). Contact line deposits in an evaporating drop. *Physical Review E, 62*(1), 756.

[95] Ristenpart, W. D., Kim, P. G., Domingues, C., Wan, J., & Stone, H. A. (2007). Influence of substrate conductivity on circulation reversal in evaporating drops. *Physical Review Letters, 99*(23), 234502.

[96] Kelly-Zion, P. L., Pursell, C. J., Vaidya, S., & Batra, J. (2011). Evaporation of sessile drops under combined diffusion and natural convection. *Colloids and Surfaces A: Physicochemical and Engineering Aspects, 381*(1), 31-36.

[97] Nguyen, T. A., Nguyen, A. V., Hampton, M. A., Xu, Z. P., Huang, L., & Rudolph, V. (2012). Theoretical and experimental analysis of droplet evaporation on solid surfaces. *Chemical Engineering Science, 69*(1), 522-529.

[98] Carle, F., Sobac, B., & Brutin, D. (2013). Experimental evidence of the atmospheric convective transport contribution to sessile droplet evaporation. *Applied Physics Letters*, 102(6), 061603.

[99] Gatapova, E. Y., Semenov, A. A., Zaitsev, D. V., & Kabov, O. A. (2014). Evaporation of a sessile water drop on a heated surface with controlled wettability. *Colloids and Surfaces A: Physicochemical and Engineering Aspects, 441*, 776-785.

[100] Picknett, R. G., & Bexon, R. (1977). The evaporation of sessile or pendant drops in still air. *Journal of Colloid and Interface Science, 61*(2), 336-350.

[101] Kneer, R., Schneider, M., Noll, B., & Wittig, S. (1993). Diffusion controlled evaporation of a multicomponent droplet: theoretical studies on the importance of variable liquid properties. *International Journal of Heat and Mass Transfer, 36*(9), 2403-2415.

[102] Erbil, H. Y., & Meric, R. A. (1997). Evaporation of sessile drops on polymer surfaces: Ellipsoidal cap geometry. *The Journal of Physical Chemistry B, 101*(35), 6867-6873.

[103] Masoud, H., & Felske, J. D. (2009). Analytical solution for inviscid flow inside an evaporating sessile drop. *Physical Review E, 79*(1), 016301.

[104] Sefiane, K., & Bennacer, R. (2011). An expression for droplet evaporation incorporating thermal effects. *Journal of Fluid Mechanics, 667*, 260-271.

[105] Kawase, T., Sirringhaus, H., Friend, R. H., & Shimoda, T. (2001). Inkjet printed via-hole interconnections and resistors for all-polymer transistor circuits. *Advanced Materials, 13*(21), 1601.

[106] de Gans, B. J., Duineveld, P. C., & Schubert, U. S. (2004). Inkjet printing of polymers: state of the art and future developments. *Advanced Materials, 16*(3), 203-213.

[107] Wang, W., Lin, J., & Schwartz, D. C. (1998). Scanning force microscopy of DNA molecules elongated by convective fluid flow in an evaporating droplet. *Biophysical journal, 75*(1), 513-520.

[108] Chopra, M., Li, L., Hu, H., Burns, M. A., & Larson, R. G. (2003). DNA molecular configurations in an evaporating droplet near a glass surface. *Journal of Rheology, 47*(5), 1111-1132.

[109] Saito, M., Sato, M., & Suzuki, I. (1994). Evaporation and combustion of a single fuel droplet in acoustic fields. *Fuel, 73*(3), 349-353.

[110] Park, C. W., & Kaviany, M. (2002). Evaporation-combustion affected by in-cylinder, reciprocating porous regenerator. *Journal of Heat Transfer, 124*(1), 184-194.

[111] Wu, S. C. (2015). Study of self-rewetting fluid applied to loop heat pipe. *International Journal of Thermal Sciences, 98*, 374-380.

[112] Su, X., Zhang, M., Han, W., & Guo, X. (2015). Enhancement of heat transport in oscillating heat pipe with ternary fluid. *International Journal of Heat and Mass Transfer, 87*, 258-264.

[113] O'Hare, K. D., & Spedding, P. L. (1992). Evaporation of a binary liquid mixture. *The Chemical Engineering Journal, 48*(1), 1-9.

[114] Liu, C., Bonaccurso, E., & Butt, H. J. (2008). Evaporation of sessile water/ethanol drops in a controlled environment. *Physical Chemistry Chemical Physics, 10*(47), 7150-7157.

[115] Saad, N., Dufour, R., Campistron, P., Nassar, G., Carlier, J., Harnois, M., Merheb, B., Boukherroub, R., Senez, V., Gao, J., Thomy, V., Ajaka, M., & Nongaillard, B. (2012). Characterization of the state of a droplet on a micro-textured silicon wafer using ultrasound. *Journal of Applied Physics, 112*(10), 104908.

[116] Dufour, R., Saad, N., Carlier, J., Campistron, P., Nassar, G., Toubal, M., Boukherroub, R., Senez, V., Nongaillard, B., & Thomy, V. (2013). Acoustic tracking of Cassie to Wenzel wetting transitions. *Langmuir, 29*(43), 13129-13134.

[117] Carlier, J., Toubal, M., Li, S., Campistron, P., Callens, D., Thomy, V., Senez, V., & Nongaillard, B. (2015). High frequency acoustic reflectometry for solid/liquid interface characterization: application to droplet evaporation. *Physics Procedia, 70*, 459-462.

[118] Li, S., Lamant, S., Carlier, J., Toubal, M., Campistron, P., Xu, X., Vereecke, G., Senez, V., Thomy, V., & Nongaillard, B. (2014). High-frequency acoustic for nanostructure wetting characterization. *Langmuir, 30*(25), 7601-7608.

[119] Bilaniuk, N., & Wong, G. S. (1993). Speed of sound in pure water as a function of temperature. *The Journal of the Acoustical Society of America, 93*(3), 1609-1612.

[120] Nikanorov, S. P., Burenkov, Y. A., & Stepanov, A. V. (1972). Elastic properties of Si. *Soviet Physics-Solid State, 13*(10), 2516-2518.

[121] Erbil, H. Y., McHale, G., & Newton, M. I. (2002). Drop evaporation on solid surfaces: constant contact angle mode. *Langmuir, 18*(7), 2636-2641.

[122] Movies of the process are available online https://www.youtube.com/channel/UCAEkDNQpD5psOHkLOGwuVRw.

[123] Seaver, M., Galloway, A., & Manuccia, T. J. (1990). Water Condensation onto an Evaporating Drop of 1-Butanol. *Aerosol Science and Technology, 12*(3), 741-744.

[124] Vatandas, M., Koc, A. B., & Koc, C. (2007). Ultrasonic velocity measurements in ethanol–water and methanol–water mixtures. *European Food Research and Technology, 225*(3-4), 525-532.

[125] Chen, P., Harmand, S., Ouenzerfi, S., & Schiffler, J. (2017). Marangoni Flow Induced Evaporation Enhancement on Binary Sessile Drops. *The Journal of Physical Chemistry B*.

[126] Kimura, M., Misner, M. J., Xu, T., Kim, S. H., & Russell, T. P. (2003). Long-range ordering of diblock copolymers induced by droplet pinning. *Langmuir, 19*(23), 9910-9913.

[127] Park, J., & Moon, J. (2006). Control of colloidal particle deposit patterns within picoliter droplets ejected by ink-jet printing. *Langmuir, 22*(8), 3506-3513.

[128] Bennacer, R., & Sefiane, K. (2014). Vortices, dissipation and flow transition in volatile binary drops. *Journal of Fluid Mechanics, 749*, 649-665.

[129] Shi, L., Shen, P., Zhang, D., Lin, Q., & Jiang, Q. (2009). Wetting and evaporation behaviors of water–ethanol sessile drops on PTFE surfaces. *Surface and Interface Analysis, 41*(12-13), 951-955.

[130] Bormashenko, E. (2009). Young, Boruvka–Neumann, Wenzel and Cassie–Baxter equations as the transversality conditions for the variational problem of wetting. *Colloids and Surfaces A: Physicochemical and Engineering Aspects, 345*(1), 163-165.

[131] Korlie, M. S. (2000). Three-dimensional computer simulation of liquid drop evaporation. *Computers & Mathematics with Applications, 39*(12), 43-52.

[132] Widjaja, E., & Harris, M. T. (2008). Numerical study of vapor phase-diffusion driven sessile drop evaporation. *Computers & Chemical Engineering, 32*(10), 2169-2178.

[133] Barash, L. Y., Bigioni, T. P., Vinokur, V. M., & Shchur, L. N. (2009). Evaporation and fluid dynamics of a sessile drop of capillary size. *Physical Review E, 79*(4), 046301.

[134] Rowan, S. M., Newton, M. I., & McHale, G. (1995). Evaporation of microdroplets and the wetting of solid surfaces. *The Journal of Physical Chemistry, 99*(35), 13268-13271.

[135] Shanahan, M. E. R., & Bourges, C. (1994). Effects of evaporation on contact angles on polymer surfaces. *International Journal of Adhesion and Adhesives, 14*(3), 201-205.

[136] Bourges-Monnier, C., & Shanahan, M. E. R. (1995). Influence of evaporation on contact angle. *Langmuir, 11*(7), 2820-2829.

[137] Hu, H., & Larson, R. G. (2002). Evaporation of a sessile droplet on a substrate. *The Journal of Physical Chemistry B, 106*(6), 1334-1344.

[138] Girard, F., Antoni, M., & Sefiane, K. (2010). Infrared thermography investigation of an evaporating sessile water droplet on heated substrates. *Langmuir, 26*(7), 4576-4580.

[139] Moore, G. E. (1998). Cramming more components onto integrated circuits. *Proceedings of the IEEE, 86*(1), 82-85.

[140] Eastman, J. A., Choi, S. U. S., Li, S., Yu, W., & Thompson, L. J. (2001). Anomalously increased effective thermal conductivities of ethylene glycol-based nanofluids containing copper nanoparticles. *Applied physics letters, 78*(6), 718-720.

[141] Hong, T. K., Yang, H. S., & Choi, C. J. (2005). Study of the enhanced thermal conductivity of Fe nanofluids. *Journal of Applied Physics, 97*(6), 064311.

[142] Patel, H. E., Das, S. K., Sundararajan, T., Sreekumaran Nair, A., George, B., & Pradeep, T. (2003). Thermal conductivities of naked and monolayer protected metal nanoparticle based nanofluids: Manifestation of anomalous enhancement and chemical effects. *Applied Physics Letters, 83*(14), 2931-2933.

[143] Wang, X., Xu, X., & Choi, S. U. (1999). Thermal conductivity of nanoparticle-fluid mixture. *Journal of Thermophysics and Heat Transfer, 13*(4), 474-480.

[144] Murshed, S. M. S., Leong, K. C., & Yang, C. (2005). Enhanced thermal conductivity of TiO2—water based nanofluids. *International Journal of Thermal Sciences, 44*(4), 367-373.

[145] Park, S. S., & Kim, N. J. (2014). A study on the characteristics of carbon nanofluid for heat transfer enhancement of heat pipe. *Renewable Energy, 65*, 123-129.

[146] Phuoc, T. X., Massoudi, M., & Chen, R. H. (2011). Viscosity and thermal conductivity of nanofluids containing multi-walled carbon nanotubes stabilized by chitosan. *International Journal of Thermal Sciences, 50*(1), 12-18.

[147] Keblinski, P., Phillpot, S. R., Choi, S. U. S., & Eastman, J. A. (2002). Mechanisms of heat flow in suspensions of nano-sized particles (nanofluids). *International Journal of Heat and Mass Transfer, 45*(4), 855-863.

[148] Kumar, D. H., Patel, H. E., Kumar, V. R., Sundararajan, T., Pradeep, T., & Das, S. K. (2004). Model for heat conduction in nanofluids. *Physical Review Letters, 93*(14), 144301.

[149] Xuan, Y., & Li, Q. (2000). Heat transfer enhancement of nanofluids. *International Journal of Heat and Fluid Flow, 21*(1), 58-64.

[150] Koo, J., & Kleinstreuer, C. (2005). Impact analysis of nanoparticle motion mechanisms on the thermal conductivity of nanofluids. *International Communications in Heat and Mass Transfer, 32*(9), 1111-1118.

[151] Chen, R. H., Phuoc, T. X., & Martello, D. (2010). Effects of nanoparticles on nanofluid droplet evaporation. *International Journal of Heat and Mass Transfer, 53*(19), 3677-3682.

[152] Yang, Y., Zhang, Z. G., Grulke, E. A., Anderson, W. B., & Wu, G. (2005). Heat transfer properties of nanoparticle-in-fluid dispersions (nanofluids) in laminar flow. *International Journal of Heat and Mass Transfer, 48*(6), 1107-1116.

[153] Naphon, P., Assadamongkol, P., & Borirak, T. (2008). Experimental investigation of titanium nanofluids on the heat pipe thermal efficiency. *International Communications in Heat and Mass Transfer, 35*(10), 1316-1319.

[154] You, S. M., Kim, J. H., & Kim, K. H. (2003). Effect of nanoparticles on critical heat flux of water in pool boiling heat transfer. *Applied Physics Letters, 83*(16), 3374-3376.

[155] Putnam, S. A., Cahill, D. G., Braun, P. V., Ge, Z., & Shimmin, R. G. (2006). Thermal conductivity of nanoparticle suspensions. *Journal of Applied Physics, 99*(8), 084308.

[156] Moghiman, M., & Aslani, B. (2013). Influence of nanoparticles on reducing and enhancing evaporation mass transfer and its efficiency. *International Journal of Heat and Mass Transfer, 61*, 114-118.

[157] Putra, N., Roetzel, W., & Das, S. K. (2003). Natural convection of nano-fluids. *Heat and Mass Transfer, 39*(8-9), 775-784.

[158] Wen, D., & Ding, Y. (2005). Formulation of nanofluids for natural convective heat transfer applications. *International Journal of Heat and Fluid Flow, 26*(6), 855-864.

[159] Chopkar, M., Das, A. K., Manna, I., & Das, P. K. (2008). Pool boiling heat transfer characteristics of ZrO2–water nanofluids from a flat surface in a pool. *Heat and Mass Transfer, 44*(8), 999-1004.

[160] Novoselov, K. S., Geim, A. K., Morozov, S. V., Jiang, D., Zhang, Y., Dubonos, S. V., Grigorieva, I. V., & Firsov, A. A. (2004). Electric field effect in atomically thin carbon films. *Science, 306*(5696), 666-669.

[161] Balandin, A. A., Ghosh, S., Bao, W., Calizo, I., Teweldebrhan, D., Miao, F., & Lau, C. N. (2008). Superior thermal conductivity of single-layer graphene. *Nano Letters, 8*(3), 902-907.

[162] Ghosh, S., Calizo, I., Teweldebrhan, D., Pokatilov, E. P., Nika, D. L., Balandin, A. A., Bao, W., Miao, F., & Lau, C. N. (2008). Extremely high thermal conductivity of graphene: Prospects for thermal management applications in nanoelectronic circuits. *Applied Physics Letters, 92*(15), 151911.

[163] Baby, T. T., & Ramaprabhu, S. (2010). Investigation of thermal and electrical conductivity of graphene based nanofluids. *Journal of Applied Physics, 108*(12), 124308.

[164] Baby, T. T., & Ramaprabhu, S. (2011). Enhanced convective heat transfer using graphene dispersed nanofluids. *Nanoscale Research Letters, 6*(1), 289.

[165] Yu, W., Xie, H., & Bao, D. (2009). Enhanced thermal conductivities of nanofluids containing graphene oxide nanosheets. *Nanotechnology, 21*(5), 055705.

[166] Yu, W., Xie, H., & Chen, W. (2010). Experimental investigation on thermal conductivity of nanofluids containing graphene oxide nanosheets. *Journal of Applied Physics, 107*(9), 094317.

[167] Kim, K. M., & Bang, I. C. (2016). Effects of graphene oxide nanofluids on heat pipe performance and capillary limits. *International Journal of Thermal Sciences, 100*, 346-356.

[168] Azizi, M., Hosseini, M., Zafarnak, S., Shanbedi, M., & Amiri, A. (2013). Experimental analysis of thermal performance in a two-phase closed thermosiphon using graphene/water nanofluid. *Industrial & Engineering Chemistry Research, 52*(29), 10015-10021.

[169] Fellahi, O., Das, M. R., Coffinier, Y., Szunerits, S., Hadjersi, T., Maamache, M., & Boukherroub, R. (2011). Silicon nanowire arrays-induced graphene oxide reduction under UV irradiation. *Nanoscale, 3*(11), 4662-4669.

[170] Turcheniuk, K., Hage, C. H., Heliot, L., Railian, S., Zaitsev, V., Spadavecchia, J., Boukherroub, R., & Szunerits, S. (2015). Infrared photothermal therapy with water soluble reduced graphene oxide: shape, size and reduction degree effects. *Nano LIFE, 5*(01), 1540002.

[171] David, S., Sefiane, K., & Tadrist, L. (2007). Experimental investigation of the effect of thermal properties of the substrate in the wetting and evaporation of sessile drops. *Colloids and Surfaces A: Physicochemical and Engineering Aspects, 298*(1), 108-114.

[172] Leong, K. C., Yang, C., & Murshed, S. M. S. (2006). A model for the thermal conductivity of nanofluids–the effect of interfacial layer. *Journal of Nanoparticle Research, 8*(2), 245-254.

[173] Ahammed, N., Asirvatham, L. G., & Wongwises, S. (2016). Effect of volume concentration and temperature on viscosity and surface tension of graphene–water nanofluid for heat transfer applications. *Journal of Thermal Analysis and Calorimetry, 123*(2), 1399-1409.

[174] Vargaftik, N. B., Volkov, B. N., & Voljak, L. D. (1983). International tables of the surface tension of water. *Journal of Physical and Chemical Reference Data, 12*(3), 817-820.